

AN ABSTRACT OF THE THESIS OF

Hannah G. Coe for the degree of Master of Science in Mechanical Engineering presented on March 18, 2019

Title: On the Role of Particle Size Distribution in Selective Laser Melting of 316L Stainless Steel

Abstract approved: _____
Somayeh Pasebani

Selective laser melting (SLM) is an additive manufacturing (AM) process that uses a laser beam to melt metal powder as it is spread onto the build surface using a roller or scraper, followed by rapid solidification to manufacture a 3D component, one layer at a time.

In SLM process, density of manufactured components is directly influenced by the density of powder bed. Remaining voids between particles can result in low relative densities, poor mechanical behavior and warping due to non-uniform shrinkage during melting. One approach for addressing the challenge of producing fully dense metal parts via SLM is by maximizing the packing density of the powder feedstock before/during melting.

The powder bed density of these metal feedstock powders is influenced by variations in powder size, powder size distribution, powder morphology, and chemical composition. The purpose of this thesis is to investigate the influence of particle size distribution (PSD) in 316L stainless steel powder feedstock on the density, microstructure and hardness of SLMed components. This austenitic steel is desirable for its strength and ductility, as well as good corrosion resistance.

Spherical powder feedstock with single and bimodal PSD (with coarse to fine particle size ratio of approximately 7:1) were used as feedstock. First, the commonly practiced methods of measuring flow properties and density of powder bed were identified in order to establish a relationship between powder characteristics and component density. This effort included designing and testing a simple method for measuring density of layer-wise spread powder to measure the density of a powder bed during the SLM process. Then, spread density was compared with other powder density measurements to determine if apparent density (ρ_a) and tap density (ρ_t) were practical indicators of powder bed density in SLM. Using the tap density of each, the optimal quantity of coarse and fine powder for each bimodal mixture was calculated.

The packing density and flowability of the mixed bimodal PSDs were determined by measuring tap density and the Hausner ratio (ρ_t/ρ_a). SLM was performed in nitrogen atmosphere at volumetric energy densities (VED) ranging from 35.7 J/mm³ to 116.0 J/mm³ using feedstock with single mode PSD where $D_{90} < 50\mu\text{m}$ and bimodal PSD with a primary large and small powder size of $\sim 35\mu\text{m}$ and $5\mu\text{m}$. The density of bulk samples made from each powder type and VED was measured using the Archimedes method. Metallography, scanning electron microscopy (SEM), and X-ray diffraction (XRD) were used to characterize the porosity, microstructure and phase identification of samples manufactured from different powder feedstocks. Furthermore, the Vickers microhardness of select samples produced from both single mode and bimodal feedstock was measured. Samples from both single mode and bimodal powder size distribution, SLMed at VEDs of 74 and 89 J/mm³, respectively, were annealed at 1020°C for two hours and were then characterized.

It was demonstrated that bimodal PSD could provide denser particle packing in a powder bed that is mechanically tapped to maximum packing density. This is because tap density of the bimodal size distributions was up to 2% greater than single mode powder from the same supplier. Relative density of SLMed parts as a function of VED at each power level revealed that for low laser power (107-178W) where relative density is below 99%, bimodal feedstock resulted in higher density than single mode feedstock. However, at higher power (>203W), the density of bimodal-fed components decreased as the VED increased, likely due vaporizing of the fine powder in bimodal distributions at higher energy levels.

Hardness was approximately similar for single mode and bimodal samples at microhardness values of ~225-245 HV using the same melting parameters. Grain size did not appear to change significantly between single mode and bimodal powders with the approximate width of columnar grains ranging from ~30-70 μ m. A fully austenite phase was maintained in SLMed components from both PSD types, both before and after annealing. Annealed samples showed recrystallization primarily adjacent to melt pool boundaries were observed prior to annealing.

In summary, this thesis demonstrates that despite higher powder bed densities in powder feedstock with bimodal PSD, differences in conduction melting and vaporization points between the two primary particle sizes would practically limit the maximum achievable density of SLMed components produced from bimodal powder.

©Copyright by Hannah G. Coe
March 18, 2019
All Rights Reserved

On the Role of Particle Size Distribution in Selective Laser Melting of 316L Stainless
Steel

by
Hannah G. Coe

A THESIS

submitted to

Oregon State University

in partial fulfillment of
the requirements for the
degree of

Master of Science

Presented March 18, 2019
Commencement June 2019

Master of Science thesis of Hannah G. Coe presented on March 18, 2019

APPROVED:

Major Professor, representing Mechanical Engineering

Head of the School of Mechanical, Industrial, and Manufacturing Engineering

Dean of the Graduate School

I understand that my thesis will become part of the permanent collection of Oregon State University libraries. My signature below authorizes release of my thesis to any reader upon request.

Hannah G. Coe, Author

ACKNOWLEDGEMENTS

First and foremost, I would like to extend my sincerest gratitude to my major professor, Dr. Somayeh Pasebani, for devoting her time, resources and knowledge to helping me fulfill my goals and for supporting me in bringing this thesis to completion. She encouraged me to always strive for excellence and has been instrumental in my development as a student researcher and future professional. Her sacrifice and commitment have been valuable in helping me reach where I am today

I also want to thank my other thesis committee members, Dr. Julie Tucker, Dr. Brian Paul, and Dr. Brian Woods for your time, patience, and feedback

My deepest thanks to Lynn Paul for encouraging and assisting in navigating the department and mechanical engineering program.

I also greatly acknowledge the financial support of Oregon Metal Initiative (OMI), Oregon Manufacturing Innovation Center (OMIC) and ATI Specialty Metals, without whom this work would not be possible. Special thanks to Drs. Nicholas Cunningham and Noah Phillips at ATI for their involvement in a portion of this work.

I also want to acknowledge ATAMI director Dr. Sam Angelos, as well as Danielle Clair, Neill Thornton, Keith Price, Todd Miller and the rest of the staff and facility personnel at ATAMI for all that you do in providing resources and creating an environment that inspires innovation.

I would like to thank: Dr. Pete Eschbach and Teresa Sawyer at the OSU Electron Microscopy for their help with SEM training and always being available to answer questions.

Dr. Brady Gibbons, for training and assistance in using X-ray diffraction, Dr. Megumi Kawasaki for assistance in microhardness testing, Dr. Donghua Xu for assistance in arc melting.

School of MIME faculty, and staff, including school head Dr. Harriet Nembhard and award committee, Lynn Paul and Dr. Porter. Also to COE for the MIME scholarship award. I am honored and grateful to the College of Engineering, for awarding me the GTA award, and the Graduate school for their financial support through the MS&T2018 travel and the thesis completion award

Thank you to Milad, for showing me the ropes and teaching me metallography and many other material science skills

To the women of my love and support group, for listening and lifting me up

To Paul, for encouraging me always and giving me strength. I am lucky to have you in my corner.

To my Parents, for believing in me unwaveringly. You have always taught me to take pride in hard work and have been there for me no matter what. I couldn't have done it without you. "Keep em guessing"

TABLE OF CONTENTS

	<u>Page</u>
Chapter 1 - Introduction and Objective	1
Chapter 2 - Background	4
2.1. Typical Particle Size Distribution.....	5
2.2. Powder Density	5
2.2.1. Apparent Density	6
2.2.2. Tap Density	6
2.2.3. Fractional Packing Density	7
2.3. Powder Flow Properties	7
2.3.1. Hall and Carney Flow Test Methods	8
2.3.2. Avalanche Angle and Angle of Repose	10
2.3.3. Hausner Ratio.....	12
2.4. Powder Spreading and Packing	12
2.4.1. Packing Density and Packing Ratio	12
2.4.2. Measuring Spread Powder Properties	13
2.4.3. Particle Morphology	18
2.4.4. Packing Optimization with Bimodal Particle Size Distribution	19
2.4.5. Wall Effects in Particle Packing	21
2.5. SLM of 316L Stainless Steel	22
2.5.1. Volumetric Energy Density (VED)	23
2.5.2. Hatch Spacing	26
2.5.3. Layer Thickness	27
2.5.4. Shift angle and Scanning Strategy	28
2.5.5. Gas Atmosphere.....	28
2.6. Phase Composition.....	30
2.7. Microstructure and Melt Pool in SLM.....	31
2.7.1. Intergranular Cells	34
2.7.2. Columnar Grains	34
2.7.3. Porosity	36
2.8. Density	37
2.9. Hardness.....	37

TABLE OF CONTENTS (Continued)

	<u>Page</u>
2.10. Design Advantages of SLM.....	38
Chapter 3 - Materials and Methods.....	41
3.1. Powder	41
3.1.1. Chemistry	42
3.1.2. Powder Size	43
3.1.3. Powder Density and Flow Measurement	44
3.1.4. Spreading Density	46
3.1.5. Mixing Bimodal Powder from Constituent Powders.....	49
3.1.6. Measuring Particle Size Distribution	50
3.1.7. Morphology.....	51
3.2. SLM Processing Parameters	53
3.2.1. Volumetric Energy Density (VED)	54
3.2.2. Support structures	56
3.2.3. Density Measurement	57
3.2.4. Metallographic Sample Preparation.....	58
3.2.5. Phase Identification.....	59
3.2.6. Microstructure and Porosity Imaging	60
3.2.7. Etching	60
3.2.8. Annealing.....	61
3.2.9. Hardness Testing.....	61
Chapter 4 – Results and Discussion.....	62
4.1. Powder properties	62
4.1.1. Powder Size Distribution	63
4.1.2. Powder Density and Flow Properties.....	65
4.1.3. Spread Density - Results of Experimental Testing Method.....	68
4.1.4. Morphology.....	71
4.2. Density of Bulk Samples	72
4.2.1. Nominal Density of Each Powder Type	72
4.2.2. Role of Volumetric Energy Density on SLMed Density	73
4.2.3. Density Dependence on Laser Power and Limitations of Volumetric Energy Density	76

TABLE OF CONTENTS (Continued)

	<u>Page</u>
4.3. Microstructural Characterization and Analysis	79
4.3.1. Porosity Analysis	79
4.3.2. Melt Pool Characterization	83
4.3.3. Intergranular Cell Growth.....	86
4.4. Phase Identification.....	88
4.4.1. X-ray Diffraction	89
4.4.2. Chemical Analysis	91
4.5. Hardness of SLMed 316L.....	93
4.5.1. Theoretical Cooling Rate	95
4.5.2. Anticipated Grain Size.....	96
4.6. Post Processing of SLMed 316L (Annealing)	97
Chapter 5 – Conclusions and Future Work.....	101
5.1. Summary and Conclusions	101
5.2. Current Limitations and Future Work.....	103
6. References.....	105
Appendix A – Publication from Thesis	111
Appendix B – Business Value and Impact on Industry	125

LIST OF FIGURES

<u>Figure</u>	<u>Page</u>
Figure 1. Particle size distribution of two powder types [11]	5
Figure 2. ASTM standard apparatus for Hall flow test method: (a) funnel and (b) stand [16]	9
Figure 3. ASTM standard funnel and stand for Carney flow method [17]	10
Figure 4. Schematics of (a) angle of repose and (b) avalanche angle [20]	11
Figure 5. Test volume for measuring density of spread powder during binder jetting [23]	14
Figure 6. Changes in powder layer thickness as a function of layer numbers for different packing density [24]	16
Figure 7. Powder spreader device designed by Van den Eynde <i>et al.</i> [22]	17
Figure 8. For randomly packed monosized particles, the fractional density can be heavily influenced by the relative roundness of the particles [8]	18
Figure 9. Illustration of a secondary particle size increasing packing density in bimodal	20
Figure 10. Effect of walls on void fraction in monodisperse packed particles [25]	21
Figure 11. (a) Schematic of the SLM process [26] and (b) illustration of the melt pool behavior during SLM [27]	23
Figure 12. Single-track scanning of 316L SLMed under parameters equaling the same VED [13]	24
Figure 13. (a) conduction mode and (b) keyhole mode in SLM of 316L as demonstrated by Bertoli <i>et al.</i> [13]	25
Figure 14. (a) Lateral cross section of 316L parts built by SLM and (b) cross section of melt pools overlap [34]	27
Figure 15. (a) Density of samples SLMed under various atmospheres and resulting sample porosity for (b) argon, (c) nitrogen, (d) helium, and (e) hydrogen	29
Figure 16. XRD pattern obtained from 316L powder and SLMed part [43]	30
Figure 17. XRD plot showing diffraction peaks indicating a fully austenite phase for bulk samples produced by SLM, hot pressing, and casting [45]	31

LIST OF FIGURES (Continued)

<u>Figure</u>	<u>Page</u>
Figure 18. EBSD micrograph of melt pool and microstructure in SLMed 316L. Dotted lines show the geometry of the melt pool [39]	32
Figure 19. SLMed 316L: (a) Melt pool geometry showing grain structure and (b)-(c) characteristic microstructure showing intergranular cells [44].....	33
Figure 20. Porosity in SLMed 316L (a) parallel to the build direction with a single orthogonal shift melt pattern, (b) normal to the build direction with a single orthogonal shift melt pattern, (c) parallel to the build direction with a checkerboard scanning strategy, (d) normal to the build direction with a checkerboard scanning strategy. All are printed with same VED (90W, 1000mm/s, 150µm hatch, 30µm layer) [39].....	36
Figure 21. Example metal lattice structures that can be constructed using SLM for weight- reducing applications [43]	39
Figure 22. Sieve shaker and stacks of standard sieve used to separate narrow particle size distribution OM-2	44
Figure 23. (a) Hall flowmeter for apparent density measurement and (b) Quantachrome Autotap AT-6-110-60 mechanical tapper with 100 mL cylinder for tap density measurement	45
Figure 24. (a) Single wall layer with base before spreading, (b) after spreading and (c) sample holder after spreading a layer and cleaning surface of excess powder.....	47
Figure 25. (a) Three layers for a total container height of ~0.048" or ~1.2mm. (b) Powder volume and mass was measured after removing walls	48
Figure 26. The vortex mixer used in this study to blend small and large powders to get a bimodal powder size distribution	50
Figure 27. (a) Malvern MASTERSIZER 3000E particle size analyzer and (b) Hydro MV suspension mixer	51
Figure 28. SEM micrographs of powders used in the first set of bimodal mixtures, (a) smaller, USRN-A, (b) larger powder OM and (c) the first bimodally distributed powder, Bimo-1	52
Figure 29. SEM micrographs of the powders used in the third bimodal mixture, including (a) the smaller, USRN-B (b) larger powder GH and (c) the third bimodally distributed powder, Bimo-3	52

LIST OF FIGURES (Continued)

<u>Figure</u>	<u>Page</u>
Figure 30. (a) ORLAS CREATOR SLM machine used in this study, (b) build chamber architecture in ORLAS CREATOR.....	53
Figure 31. 5x5x5 mm SLMed sample cubes with power% varying from 50-80% and scan speed varying from 700-1200 mm/s	54
Figure 32. Digital balance equipped with Archimedes density kit for dry and liquid-submerged weighing	57
Figure 33. Metallography and sample preparation (a) cutting saw, (b) hot mounting, (c) grinding and polishing equipment and (d) vibratory polisher	59
Figure 34. Particle size distribution histogram of fine particles (USRN-A) measured by Malvern particle size analyzer	63
Figure 35. Histogram of particle size distribution for (a) coarse 316L powders with normal PSD (OM) and narrow PSD (OM-2), and (b) bimodal mixtures containing coarse powder with normal PSD (Bimo-1) and narrow PSD (Bimo-2)	64
Figure 36. Powder bed densities for each powder type	66
Figure 37. Hausner ratio measured for each powder type. The red dotted line shows upper limit of “good flow” at $H < 1.25$	67
Figure 38. SEM micrograph of powder used in second experiment batch. Note satellite powders forming on the outside, perhaps leading to poor flowability. Powders were relatively spherical.	71
Figure 39. Measured nominal density of each powder type compared to standard value from literature [14].	73
Figure 40. Relative density as a function of volumetric energy density for SLMed samples produced with single mode powder (OM), normally-distributed bimodal powder (Bimo-1), and bimodal powder with a narrow size distribution of large powder (Bimo-2).	74
Figure 41. Relative density of 316L SLMed samples as a function of volumetric energy density for single mode feedstock powder (GH) and bimodal feedstock powder (Bimo-3)	76
Figure 42. Relative density values as a function of volumetric energy density for different power: 107, 139, 178 and 203 W. For each power level, scan speed ranges from 700-1200 mm/s.....	77

LIST OF FIGURES (Continued)

<u>Figure</u>	<u>Page</u>
Figure 43. Optical micrographs and their corresponding Image J obtained from parallel cross-sections of GH single mode powder SLMed at 203W and at VED of (a) 90.2, (b) 101.5 and (c) 116 J/mm ³	80
Figure 44. Optical micrographs and their corresponding Image J obtained from parallel cross-sections of bimodal size distribution powder Bimo-3 SLMed at 203W and at VED of (a) 90.2, (b) 101.5 and (c) 116 J/mm ³	81
Figure 45. Optical micrograph showing melt pool measurement for Bimo-3 at VED=90.2J/mm ³	83
Figure 46. Optical micrographs showing melt pool in samples from single mode and bimodal size distribution powder SLMed at different VEDs	85
Figure 47. SEM micrographs obtained from (a)-(b) single mode powder and (c)-(d) bimodal SLMed at 80% power, 1000 mm/s, VED=81.2 J/mm ³	86
Figure 48. SEM micrograph obtained from single mode (a)-(b) and bimodal (c)-(d) powder size distribution SLMed at 80% power, 700 mm/s, VED=700 J/mm ³	87
Figure 49. XRD pattern of OM single mode powder, and SLMed samples produced from OM powder and Bimo-2 powder	89
Figure 50. XRD pattern of Hoeganaes large powder, USRN-B small powder, and SLMed samples produced from bimodal powder size distribution (combination of USRN-B small powder and Hoeganaes large powder).....	90
Figure 51. GH single mode powder SLMed at 80% power and 1000 mm/s: (a) SEM micrograph parallel to build direction, (b) corresponding EDS histogram, Bimo-3 Bimodal powder SLMed at 80% power and 1000 mm/s: (c) SEM micrograph parallel to build direction and (d) corresponding EDS histogram	92
Figure 52. (a) Vickers microhardness of SLMed samples produced from different powders at various VEDs (66-116 J/mm ³), (b) relative density of samples tested for hardness.....	94
Figure 53. Optical micrograph obtained at 200x magnification: (a) Arrows show the direction of columnar grain growth for as-built single mode sample SLMed at (b) annealed single mode sample SLMed at 73.8 J/mm ³ with no melt pool boundaries, (c) annealed bimodal sample SLMed at 89.0 J/mm ³	97
Figure 54. (a) Single mode GH sample SLMed at 73.8 J/mm ³ , annealed for two hours at 1020°C. Dotted lines trace regions of new grain growth along high-diffusivity paths that formed melt pool boundaries prior to annealing.	98

LIST OF FIGURES (Continued)

<u>Figure</u>	<u>Page</u>
Figure 55. Bimodal Bimo-3 sample SLMed at 89.0 J/mm^3 , were annealed for two hours at 1020°C . Dotted lines trace regions of new grain growth along high-diffusivity paths that formed melt pool boundaries prior to annealing.	99
Figure 56. XRD patterns of annealed Bimo-3 and GH samples indicating a pure austenite phase	100

LIST OF TABLES

<u>Table</u>	<u>Page</u>
Table 1 – Standard Composition of 316L (wt%).....	22
Table 2 – Naming convention and size range of each powder type	42
Table 3 – Composition of powders reported by manufacturer (wt%)	42
Table 4 – Concentration of “*other” nonmetal elements reported in powder (wt%) ..	43
Table 5– Particle size distribution of 316L procured from various powder manufacturers.....	43
Table 6 – Mixing ratios of three bimodal size distributions	49
Table 7 – Actual Power Level of Percent Machine Power	55
Table 8 – Constant SLM Parameters	55
Table 9 – Parameter Matrix with VED values.....	56
Table 10 - Spread density of <149µm water-atomized 304 stainless steel with 0.41 mm layers	68
Table 11 - Spread density of gas-atomized 316L stainless steel with 0.114 mm sheets	70
Table 12 – Density values measured from area percent porosity based on analysis of optical micrographs and density values measured from Archimedes method for parts made from single mode GH powder and bimodal power Bimo-3 (parts were SLMed at VED of 90.2, 101.5 and 116 J/mm ³).....	82
Table 13- Average thickness of melted layer for GH and Bimo-3 powder at VED of 90.2, 101.5 and 116 J/mm ³	84
Table 14- Measured cell area and cell width of cellular structure observed in single mode and bimodal powder size distribution SLMed at VED of 81.2 and 116 J/mm ³ ..	88
Table 15 Chemical composition (wt%) of single mode and bimodal powder size distribution SLMed at 80% power and 1000 mm/s, VED= 81.2 J/mm ³ based EDS histogram shown in Fig. 14 b, d.....	93
Table 16 – Calculated cooling rate based on width of intergranular cells.....	96
Table 17 – Theoretical grain width in µm calculated from measured hardness	96

To my beloved family

Chapter 1 - Introduction and Objective

Selective laser melting (SLM) is a laser powder bed fusion (LPBF) additive manufacturing (AM) process in which three-dimensional parts are manufactured, one two-dimensional layer at a time. This is done by scanning a laser in prescribed pattern on the surface of a bed of metal powder. In SLM, a solid metallic part can be produced as a single object by melting thin layers of metal, with a high-powered laser, in the shape of individual “slices” of the 3D object. Each layer then solidifies rapidly, allowing a 3D object to be built by repeatedly spreading, and then melting, a new layer of powder over the surface of the previously solidified layer [1].

Powder-based additive manufacturing technologies such as SLM have been developed into useful tools that could soon replace or supplement many subtractive metal manufacturing methods such as machining and casting [2]. Recent studies on SLM have shown that many metal alloys can be printed to ~ 99% of full density [3]. Maximum density is critical to the quality of parts produced by SLM. Partially melted powder, poor layer adhesion, contaminants in the feedstock or atmosphere gas, or uneven spreading during SLM can result in voids and porosity in the solidified material [3–5].

Defects such as voids, cavities and porosity (even in small concentrations), can reduce the density of the material and negatively impact the mechanical characteristics of parts produced by SLM. Powder layer thickness, laser power, laser scan speed and other build parameters can be adjusted to increase the consolidation of the powder bed and ensure high density in the final part. The powder bed density for normally distributed powder sizes is typically around 60% of the bulk material density [6]. Maximizing this relative density

of the powder bed could result in improved density and further on dimensional accuracy in solid parts produced by SLM.

Early work by McGeary [7], later elaborated upon by professor Randall German [8], has reported on the benefit of bimodal size distributions to achieve higher powder bed packing densities than powders with a single primary particle size. This concept has enormous potential in powder based additive manufacturing processes, where maximizing powder bed density is crucial to maximizing final component density. Karapatis *et al.* [9] used this work in a study on the effect of particle size distribution in selective laser *sintering* (SLS) with particle sizes ranging in the 20-200 μm size. This study found that for high ratios of small to large particle size (over 1:10), apparent density of the bimodal powder was over 15% percent higher than that of single mode PSDs.

Similarly, McGeary's model for measuring and mixing bimodal powders was utilized for binder jetting in a study by Do *et al.* [10]. For binder jetting, it was found that use of bimodal powder not only increased the packing density of the powder bed, but also improved the surface finish, and reduced the distortion and shrinkage of parts that were sintered following binder jetting [10]. In the SLM process, however, the single mode particle size distribution typically used is smaller than with SLS (D_{90} = 45-50 μm for SLM), and temperatures are much higher in SLM than in binder jetting and sintering with the same particle size. Efforts to apply the concept of using bimodal particle size distribution in SLM has thus far been largely unexplored.

Therefore, the objective of this study was to evaluate the spreading properties and packing density of multiple 316L stainless steel powder bed feedstocks; with a single mode

particle size distribution (typically used in SLM process) and bimodal particle size distribution (has not been explored in SLM process). For bimodal particle size distribution, three different powder mixtures were prepared and used as SLM feedstock. After comparing the packing density of these powder size distributions, solid samples were then manufactured via optimized SLM process. Density, microstructure, and mechanical properties of these SLMed samples were characterized before and after annealing.

The goal of this Master's thesis was to determine the role of particle size distribution of powder bed on density, microstructure and mechanical properties of the 316L stainless steel components additively manufactured via SLM process.

Chapter 2 - Background

In this chapter, a review on metal powder feedstock, SLM process and other studies on SLM of 316L stainless steel is presented. The following includes an overview of measurement methods and physical characteristics of both raw powder and bulk material processed by SLM.

Powder characteristics that influence the quality of SLMed parts include particle size and particle size distribution (PSD), apparent and tap density, surface roughness of spread powder, powder flowability, and thermal conductivity of pre-melted powder beds. The measurement methods described in the following review can be used to help understand the behavior of metal precursor powder used in powder bed fusion additive manufacturing methods such as SLM and SLS. Although the goal is to apply these methods to metal powders, literature related to other powdered materials such as pharmaceuticals and polymer AM precursors were also considered.

Furthermore, this review provides an overview of the SLM process and describes the significance of the influence of various parameters involved in SLM. Characteristics of 316L having undergone processing by SLM have been studied extensively in previous research and will be summarized in this review to compare with results found in this study. These characteristics include phase composition, microstructure, melt pool behavior, density, and microhardness.

2.1. Typical Particle Size Distribution

Most gas-atomized powders, like the powder used in this study, contain a range of particle sizes, with a typical Gaussian size distribution, as shown in Figure 1. The plot in Figure 1, from a study by Liu *et al.* [11] displays the percentage of each particle size that can be found in each of two powders with different size distributions. The average particle size needed for a particular SLM experiment may vary depending on other SLM parameters, but typical powder sizes range between $\sim 10\mu\text{m}$ and $\sim 50\mu\text{m}$ [5,12-13]. While SLM parameters such as layer thickness and laser spot size can be limited by the largest or most abundant powder size, the distribution of intermediate and small particle sizes can greatly impact the packing density and other properties of a powder bed [11].

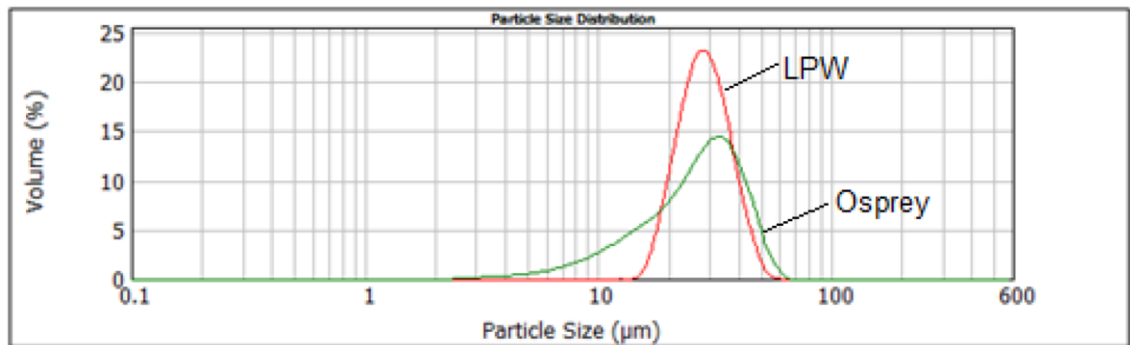


Figure 1. Particle size distribution of two powder types [11]

2.2. Powder Density

For a part printed by SLM to possess the properties of its parent material, the density of the part would need to be nearly the density of the parent material. In powder manufacturing processes, the density of the loose powder bed has a direct impact on the

density of the part. By optimizing the density of the powder bed before printing, more precision should be achievable in the geometry of printed parts with near full material density.

2.2.1. Apparent Density

Bulk density, also known as apparent density (ρ_a) in many cases, is the density of the powder in the “as-filled” or “as-spread” state. Apparent density is often measured by pouring powder into a container of known volume (generally 25 cm³) from a funnel like those used in the Hall and Carney methods (see section 2.3.1). The mass of the powder, once leveled in the container by a scraper, can then be divided by the volume (generally 25 cm³) to determine the density of the powder in the cup. In the case of powders used in additive manufacturing, apparent density may refer to the density of the powder that has been spread into the powder bed layer by layer [6].

2.2.2. Tap Density

Tap density (ρ_t) is the density of powder as measured from the volume occupied by a given mass of powder (generally 100 g) after it has been “tapped” or consolidated to its minimum height in a container by mechanical vibration after certain number of taps (generally >3000 times). Neither the tap density nor the bulk density can be considered constant values for a given shape, size and composition of particle, as the results of such measurements vary greatly by container size and shape. However, tap density of normally-

distributed powders in size ranges used for SLM is typically within the range of 60-70% of the material density [5].

2.2.3. Fractional Packing Density

The fractional packing density, f , refers to the ratio of the maximum density of the powder bed relative to the density of the bulk material, as shown in Equation 1:

$$f = \rho_t / \rho_m \quad \text{Equation 1}$$

where ρ_t is the measured tap density of the powder and ρ_m is the density of the material from which the powder is made. In this study, 316L stainless steel was used, which has a material density, ρ_m , of approximately 8.0 g/cm³ [14]. In some cases, the chemical composition of 316L steel can vary slightly, leading to differences in parent material density. For each batch of 316L powder, ρ_m was measured by Archimedes density measurement of arc melted SLMed samples (as will be discussed in the experimental and methods section) to ensure correct material densities were compared to SLMed samples.

2.3. Powder Flow Properties

In the production of pharmaceutical powders and other industries concerned with handling granular material, flowability, or the ability of a powder to be “poured” with ease, can accurately represent the quality of the material. However, for correlating flow properties to success in powder bed additive manufacturing, a better descriptor for the

behavior of particles would be the “spreadability” of a powder, since the bulk density described by powder flow models would then refer to the density of a powder after it has been spread, not poured.

Flowability is a characteristic commonly used to make predictions about the behavior of powders when they are spread into the powder bed. Properties that are generally attributed to powders with good flowability include high density and minimal surface roughness [8, 15]. Several types of values are commonly used to indicate the relative flow of powders, determined by a standard methodology as described in the following section [16–19].

2.3.1. Hall and Carney Flow Test Methods

One of the ASTM standard test methods commonly used to quantify flowability of powder is the Hall Flow test method [16]. The Hall technique is performed by first placing a funnel, like the one in Figure 2a, into a test stand as shown in Figure 2b. Then, a known mass of powder (typically 50g) is poured into the funnel while blocking the funnel tip. The tip barrier is then removed at the moment that a timer is started. The elapsed time required for all the powder to flow from the funnel into a container at the base is then used to calculate the Hall flow rate (FR_H) according to Equation 2, where t is the elapsed time in seconds.

$$FR_H = \frac{t}{50g} \quad \text{Equation 2}$$

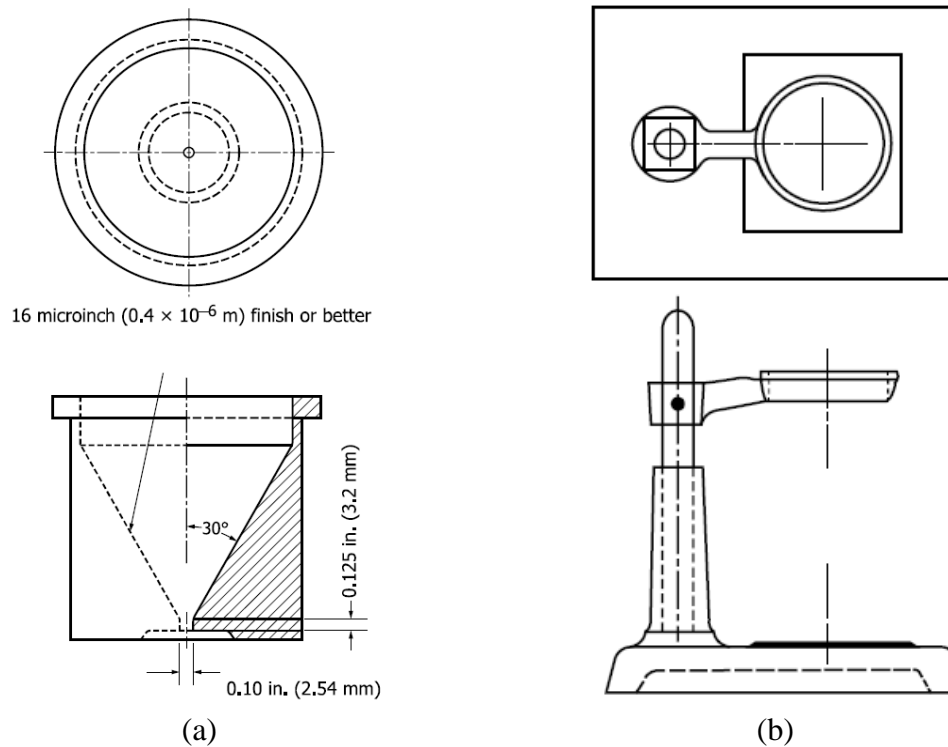


Figure 2. ASTM standard apparatus for Hall flow test method: (a) funnel and (b) stand [16]

The Carney flow test method is similar to the Hall technique, as illustrated by the familiar apparatus shown in Figure 3 [17]. For the Carney method, however, the mass of powder varies (typically between 150-200g) depending on the material used. The same measurement procedure is used for both the Hall and Carney method. The Carney flow rate (FR_C) determined from elapsed time in seconds (t) and the powder mass (M) as shown in Equation 3.

$$FR_C = \frac{t}{M}$$

Equation 3

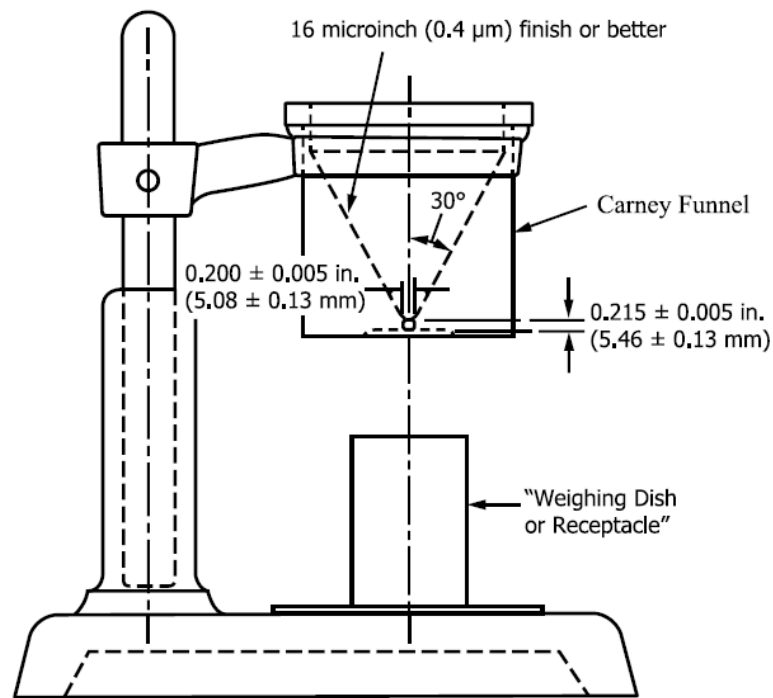


Figure 3. ASTM standard funnel and stand for Carney flow method [17]

2.3.2. Avalanche Angle and Angle of Repose

Another method for measuring the flowability and cohesiveness of powder is by determining the maximum angle a pile of powder will retain on its sides before the powder falls. Two of these types of measurements include the avalanche angle and the angle of repose. A study by Krantz *et al.* [20] compares and describes these and other methods utilized by various industries for characterizing powders [21].

Angle of repose (AOR), θ_R , is determined by a standard procedure in which powder is poured from a funnel onto a circular plate. As powder accumulates, it reaches a certain height such that, rather than accumulating into a taller peak, powder pours down the side of the heap, ultimately forming a cone. The angle between the base plate and side of the

cone is known as AOR, as shown in the schematic in Figure 4. When $\theta_R < 30^\circ$ it is generally regarded as excellent flow.

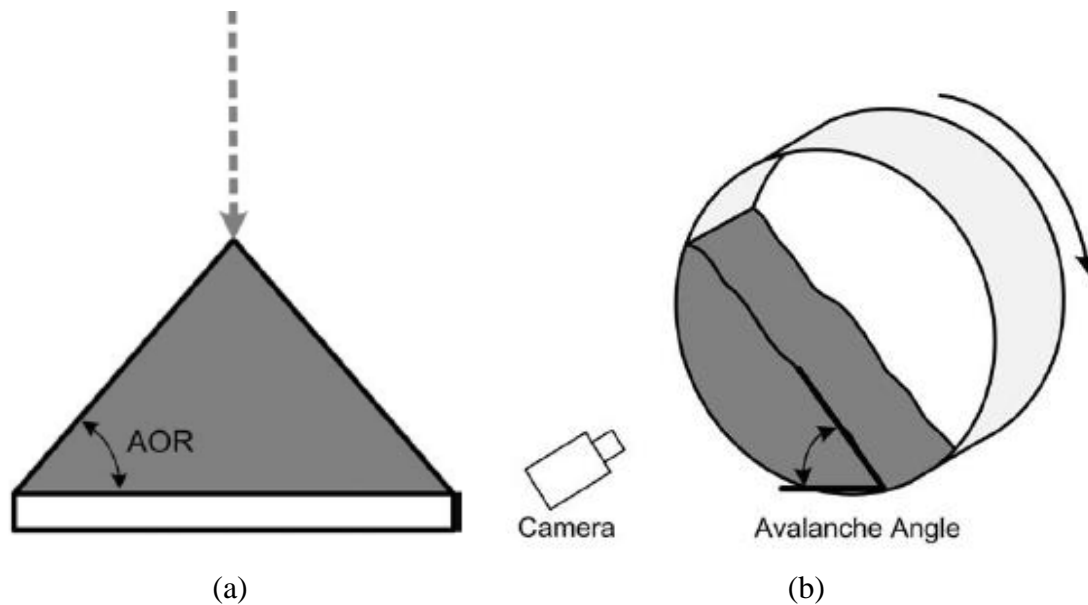


Figure 4. Schematics of (a) angle of repose and (b) avalanche angle [20]

To measure the avalanche angle (θ_A) of a powder, a known volume of powder is poured into a large cylindrical drum which is then rotated at a low, constant rpm with the cylinder's axis parallel to the ground. During rotation, cohesion between particle and between particles and the walls of the drum cause the heap of powder to maintain contact briefly with the wall. When the powder is carried high enough along the wall, it then “avalanches” at a characteristic angle known as the avalanche angle, as illustrated in Figure 4. A digital camera can be used to observe this motion and determine the avalanche angle for a given powder.

2.3.3. Hausner Ratio

An attribute used in this study to determine good flowability of a powder is the Hausner ratio, H . As early as 1969, the Hausner ratio has been observed to have a relationship to properties of metal powders [18-19]. The Hausner ratio is a value found by comparing the bulk, or apparent density (ρ_a) of a powder to the tap density (ρ_t) of the powder, according to Equation 4. Powders with a Hausner ratio less than 1.25 are generally considered to be “free flowing” [6].

$$H = \frac{\rho_t}{\rho_a} \quad \text{Equation 4}$$

2.4. Powder Spreading and Packing

Understanding the process of spreading powder on an SLM build platform is important because better spreading in the first few layers of powder will consequently lead to more uniform spreading in the subsequent layers. Uniform spreading is also necessary for efficient thermal conductivity and heat transfer during the SLM process.

2.4.1. Packing Density and Packing Ratio

Powder spreading in SLM is one layer at a time, rather than poured as a bulk like the apparent density measurements. Thus, a more appropriate measurement of spreading properties of a powder in SLM is the packing density, ρ_p , as given in Equation 5 [22].

$$\rho_p = \frac{\rho_{layer}}{\rho_m} \quad \text{Equation 5}$$

Where ρ_{layer} is the density of a layer spread during the laser melting processes and ρ_m is the material density. Since, in practice, the maximum density that can be achieved in a powder bed is the tap density, a measurement by which particles can be compared for their efficiency in laser melting or sintering is the packing ratio, PR, as defined in Equation 6.

$$PR = \frac{\rho_{layer}}{\rho_t} \quad \text{Equation 6}$$

Where ρ_t is the tap density of the powder bulk.

2.4.2. Measuring Spread Powder Properties

In a study by Bai and Williams [23], the spreading density of a copper powder used for binder jetting was found by capturing the in-situ apparent density of powder that has undergone the spreading process. This was done by manufacturing an open cube of known volume, as shown in Figure 5, and measuring the mass of the loose powder inside the cube after the binder jetting process. This method was adapted to SLM by Liu *et al.* [11] to determine the density of the powder that was spread during the melting process. While this could be considered a more accurate representation of powder bed density than apparent density measurements, the repeatability of this technique is dependent upon the ability to recover the powder contained within the test volume after processing.

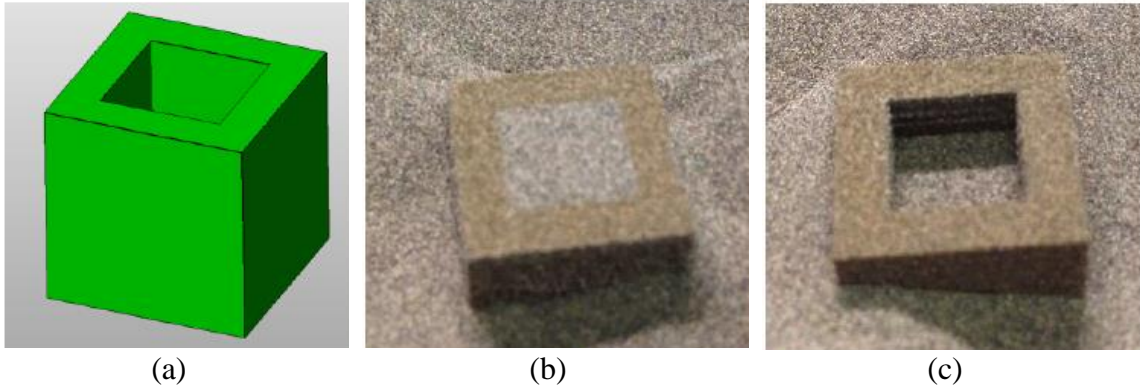


Figure 5. Test volume for measuring density of spread powder during binder jetting [23]

Results from Liu's work, however, suggest that spread density is directly proportional to the Hausner ratio of the powder, higher than its apparent density and lower than tap density. Furthermore, most SLM bulk samples in Liu's study showed higher density when produced from powders with a higher spread density and lower Hausner ratio [11]. This suggests that measuring the Hausner ratio of a powder may be an effective method of predicting its relative usefulness in producing high-density components via SLM.

A study by Mindt, *et al.* [24] implies the initial distribution of powder onto the processing table is an overseen first order input. In this study, three separate powder layer values were used: processing table displacement (δ_t), fresh powder layer thickness (δ_p), and consolidated layer thickness (δ_c). Where δ_t is set by the machine operator, δ_p indicates the depth required for heat penetration, and δ_c represents the height addition to the final built part from a single spread of powder. The packing density, ρ_p (Equation 5), relates the two measured values here by Equation 7.

$$\delta_c = \delta_p \rho_p \quad \text{Equation 7}$$

Thus, by adding the downward displacement of the table, the powder layer thickness of an upcoming layer (n+1) is predicted by the density and thicknesses of the previous layer (n) according to Equation 8.

$$\delta_{p|n+1} = \delta_{t|n+1} + \delta_{p|n}(1 - \rho_{p|n}) \quad \text{Equation 8}$$

Figure 6 shows how thickness of the powder increases with each table displacement for three assumed packing densities. According to the plot, powder layer thickness increases by layer, until an equilibrium value is reached, after which the thickness of powder in each layer reaches a steady state. At higher packing density, this steady state is achieved at lower layer numbers.

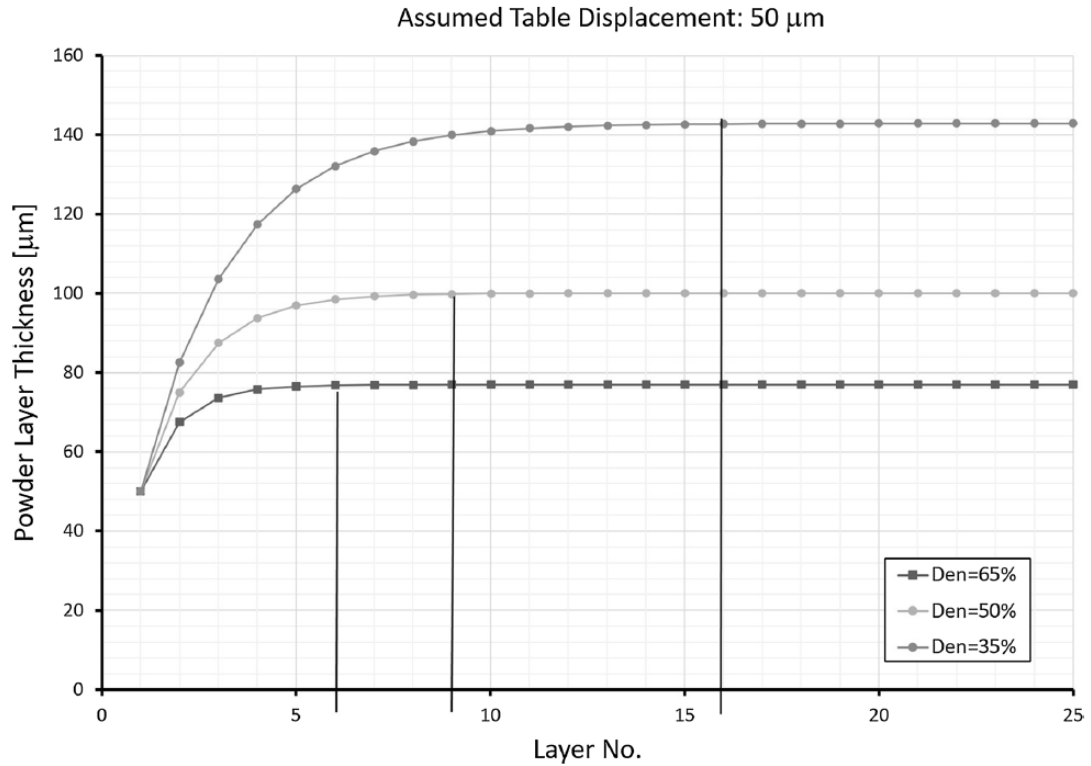


Figure 6. Changes in powder layer thickness as a function of layer numbers for different packing density [24]

Van den Eynde *et al.* [22] designed a measurement technique that mimics the spreading process in a laser sintering machine using polymer powder. This powder spreader device, shown in Figure 7 is composed of a modified spreading blade from a commercial motorized film applicator, which spreads a thin layer of powder, loaded into the front of the spreading blade, across a measurement plate. The measurement plate is located on a balance below the support plate, allowing for the mass of a powder sample to be measured. The density of the spread sample was then determined from this mass, and the volume of the sample (taken from the dimensions of the plate times the layer thickness) [22].

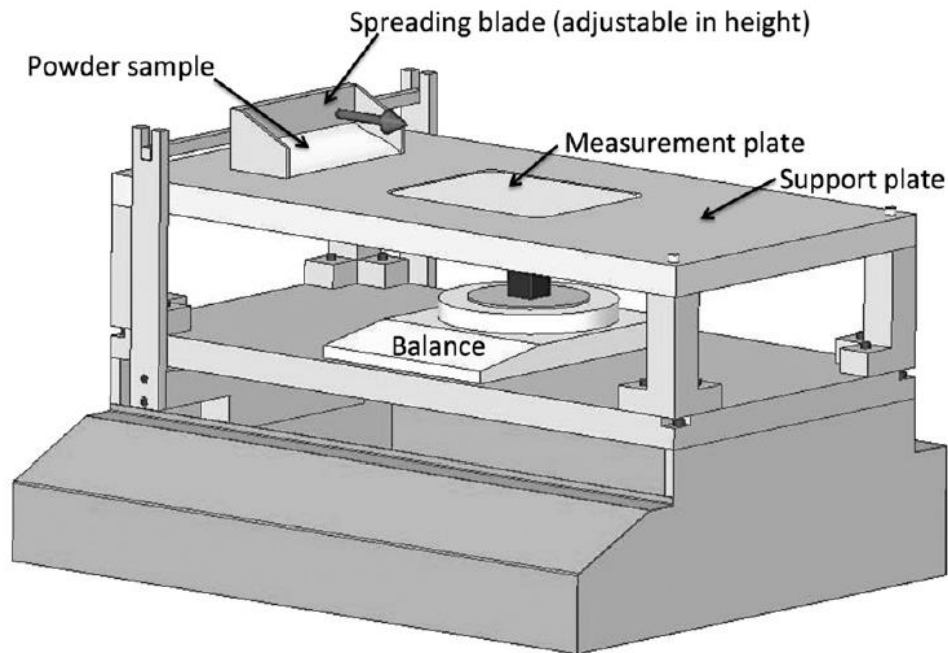


Figure 7. Powder spreader device designed by Van den Eynde *et al.* [22]

Layer thickness was set by raising or lowering the spreading blade (adjustable to a precision of $10\mu\text{m}$). To establish a uniform powder layer at the beginning of the measurement, the measuring plate was set to 1mm below the top surface of the support plate, and a layer of powder was spread with the blade set at $0\mu\text{m}$. Subsequent layers were added by raising the blade by $100\mu\text{m}$, loading about twice the amount of powder needed for a layer, and spreading the new layer. This was performed for 20 layers, with the balance being reset before each layer, thus allowing for the density of each layer to be recorded and averaged [21].

2.4.3. Particle Morphology

In practice, most powder industries involve particles of irregular or non-spherical shape. Surface roughness can create friction between particles which limits their ability to flow into a packed structure. Professor Randall German [8] characterized powder roughness by the “relative roundness” of an irregular shaped particle, where a perfectly spherical particle has a roundness value of 1.0. Round particles flow past each other more easily and stack more closely to each other than irregular powders, so the fractional packing density of a powder tends to be greater the more spherical the particle shape. This relationship between irregularity of shape and fractional density is shown in Figure 8 [8].

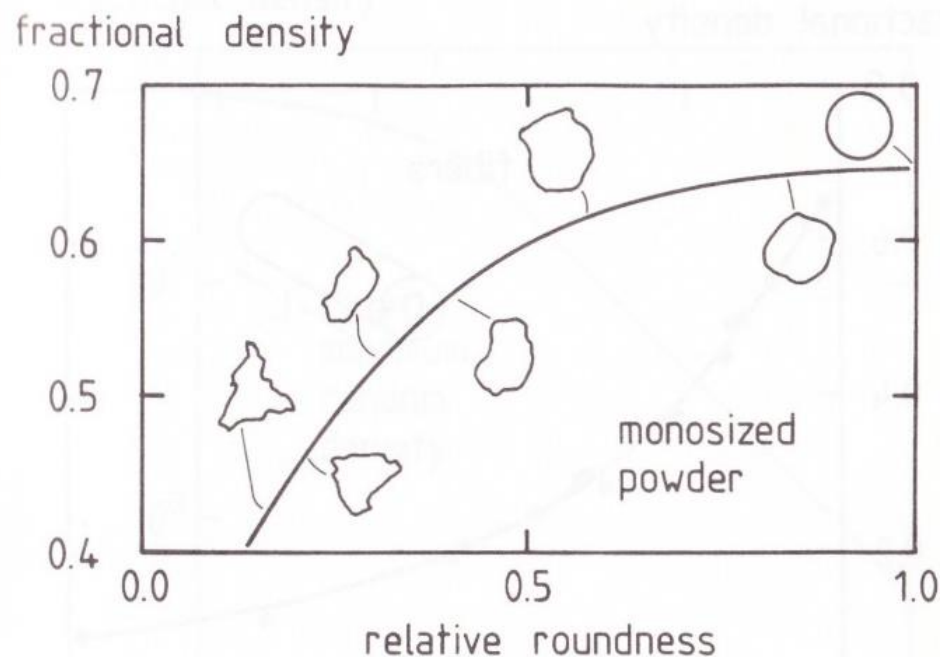


Figure 8. For randomly packed monosized particles, the fractional density can be heavily influenced by the relative roundness of the particles [8]

The sphericity, Ψ of a particle can be described by Equation 9 where S is the actual surface area of a particle and S_s is the surface area of a sphere of the same volume as the particle. The sphericity of a particle type may be experimentally approximated based on the fractional tap density, f_t , according to the experimentally determined relationship in Equation 10 [8].

$$\psi = \frac{S_s}{S} \quad \text{Equation 9}$$

$$\Psi = 0.79 + 0.831f_t + 1.53f_t^3 \quad \text{Equation 10}$$

2.4.4. Packing Optimization with Bimodal Particle Size Distribution

In a study by Karapatis *et al.* [9], mathematical models and experimental procedures were used to determine what parameters can be controlled to increase the powder layer density in SLS. McGeary *et al.* [7] showed that for powder bulks, the optimal achievable density was found by combining fine and coarse powders to create a bimodal particle size distribution, as illustrated in Figure 9. McGeary found that for these bimodal powders, a size ratio between large and small particle size of about 1:7, and a composition of about 30% fine particles can produce optimal packing density. In addition to experimental validation, the size relationship is expressed geometrically according to Equation 11, where r is the radius of fine particles, and R is the radius of coarse particles.

$$r = \left(\frac{2}{\sqrt{3}} - 1 \right) \cdot R \equiv \frac{1}{7} R \quad \text{Equation 11}$$

The weight percentage of fine powders, X_{fines} that is required for optimal packing density is determined from the relative density of the fine and coarse powders, according to Equation 12.

$$X_{\text{fines}} = 1 - \frac{\rho_{\text{coarse}}}{\rho^*} = 1 - \frac{\rho_{\text{coarse}}}{\rho_{\text{coarse}} + (1 - \rho_{\text{coarse}}) \cdot \rho_{\text{fines}}} \quad \text{Equation 12}$$

Theoretically, assuming 60% for relative density of both the coarse powder, ρ_{coarse} , and the fine powder, ρ_{fines} , a maximum density, $\rho^* = 0.84$ times the material density can be achieved using $X_{\text{fines}} = 30$ wt% fines. Karapatis [9] demonstrated that an even larger size ratio of 1:10 between coarse and fine particles, using a 30% composition of fines, can yield a density increase of approximately 15% compared to monodisperse particles.

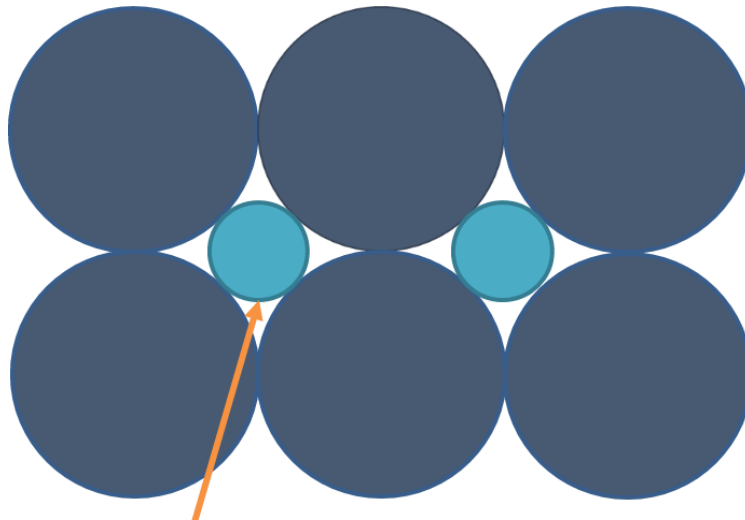


Figure 9. Illustration of a secondary particle size increasing packing density in bimodal

2.4.5. Wall Effects in Particle Packing

McGeary's model [7] is valid for powder bulks where the volume of the container is several orders of magnitude greater than the average particle size. However, if the thickness of a powder volume is less than ten times the particle diameter (as with individual powder layers in SLS and SLM) a lower maximum packing density can be achieved with the same size ratio and particle size distribution. This is due to inefficient packing along the flat walls of a powder container, including the surface of the build platform. A greater dominance of wall effects is due to a higher concentration of voids in monodisperse particle packing, as shown in Figure 10.

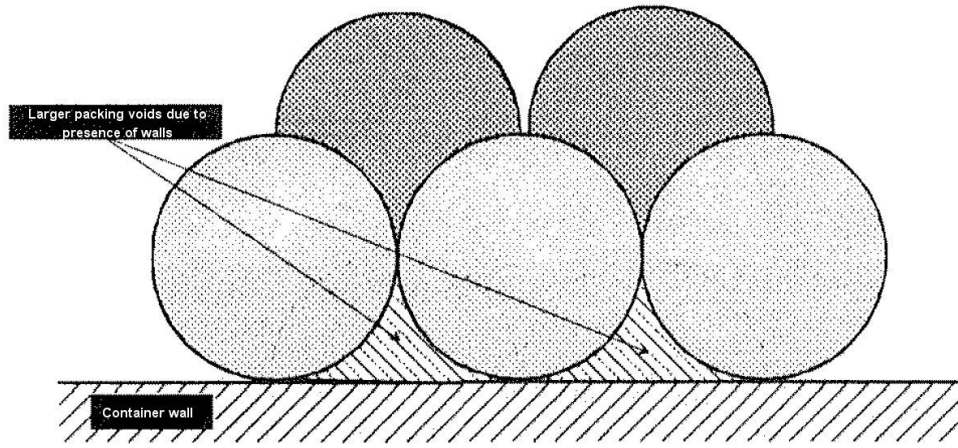


Figure 10. Effect of walls on void fraction in monodisperse packed particles [25]

Therefore, a higher concentration of fine particles is required to achieve maximum density. The void volume due to walls, V_{walls} , compared to the total void volume, V_{voids} , for an orthorhombic arrangement of particles of radius R , deposited in disk-shaped layer of diameter D and height h is shown geometrically by Equation 13 [9].

$$\frac{V_{walls}}{V_{voids}} = \frac{\frac{1}{3}\pi^2 R \cdot D \cdot \left(\frac{D}{4} + h\right)}{0.4 \cdot \pi \frac{D^2}{4} \cdot h + \frac{1}{3}\pi^2 R \cdot D \cdot \left(\frac{D}{4} + h\right)} \approx \frac{R \left(\frac{D}{4} + h\right)}{0.4 \frac{D}{4} h + R \left(\frac{D}{4} + h\right)} \quad \text{Equation 13}$$

The larger the cavity height for a given powder size, the smaller the total volume of voids along the wall is as compared to total volume of voids between particles [9]. Karapatis [9] theorized that the roughness of the surface of each sintered or melted layer allows for a less significant influence of wall effects for newly spread powder layers. Thus, greater relative density of the powder bed is achieved further from the walls of the powder bed containment.

2.5. SLM of 316L Stainless Steel

The material used in this study is 316L stainless steel. As a low-carbon, austenitic steel, 316L is desirable for use in SLM and other AM processes due to its strength, toughness, and corrosion resistance. American Society for metals (ASM) standard composition ranges for 316L stainless steel are given in Table 1 [14].

Table 1 – Standard Composition of 316L (wt%)

Fe	Cr	Ni	Mo	Mn	Si	N	P	C	S
Bal.	16-18	10-14	2-3	< 2	< 0.75	< 0.10	<0.045	< 0.03	< 0.03

In SLM, a laser beam melts the layer of metal powder as it is spread onto the build surface using a roller or scraper, cooling rapidly to form a solid shape, one layer at a time.

Figure 11 a-b shows a simplified visual illustration of the SLM process.

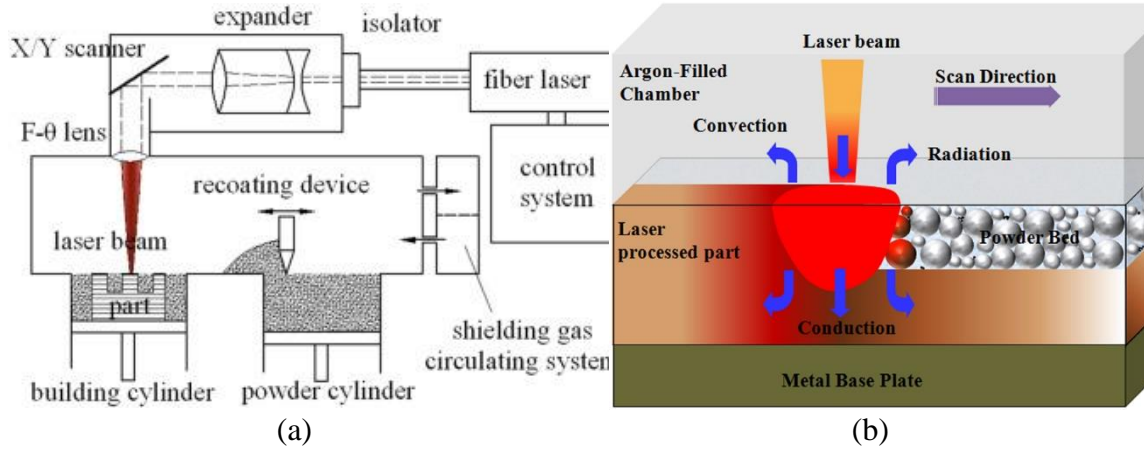


Figure 11. (a) Schematic of the SLM process [26] and (b) illustration of the melt pool behavior during SLM [27]

2.5.1. Volumetric Energy Density (VED)

The intensity of a laser beam as it melts metal powder during SLM is dependent on parameters such as power (P), scan speed (v), layer thickness (t), and laser beam diameter (σ). These parameters can be combined into a single metric of establishing the amount of energy going into the powder, known as the volumetric energy density (VED). VED can be calculated according to Equation 14 [13, 28], though in some studies, σ is defined by hatch spacing (see section 2.5.2) [29, 30].

$$VED = \frac{P}{v\sigma t} \left[\frac{J}{mm^3} \right] \quad \text{Equation 14}$$

According to Bertoli *et al.* [13], VED does not provide a complete picture for predicting melt pool behavior or component density, as it fails to account for complex melt pool physics. For example Marangoni flow and recoil pressure can influence the continuity

of the melt track [31]. Marangoni flow is mass flow driven by surface tension gradients in a fluid. In a melt pool during SLM, high temperature gradients can produce differences in surface tension within the liquid metal, causing this kind of flow to occur along the boundaries of the melt pool [32]. Furthermore, recoil pressure is caused by the rapid expansion of metallic gas when a laser heats the material beyond its vaporization temperature during SLM [32].

As shown in Figure 12, the effect of these processes can differ for different melting parameters, even if those parameters equate to the same VED. Figure 12 shows a single melt track experiment, demonstrating the continuity of the melt pool of 316L after SLM for five different parameter sets equaling the same VED.

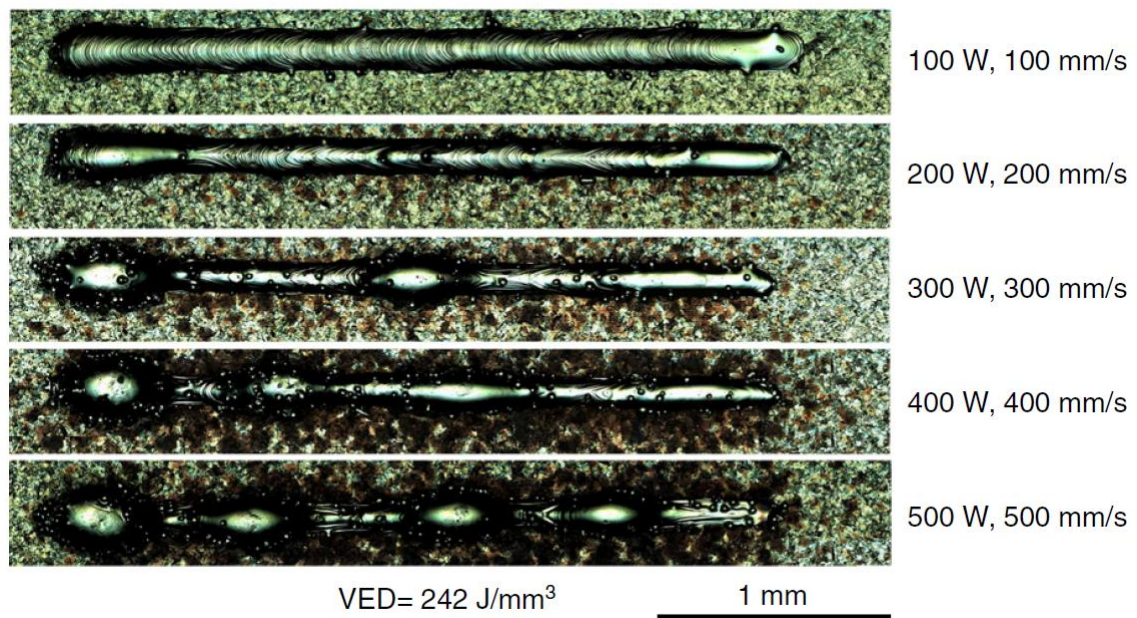
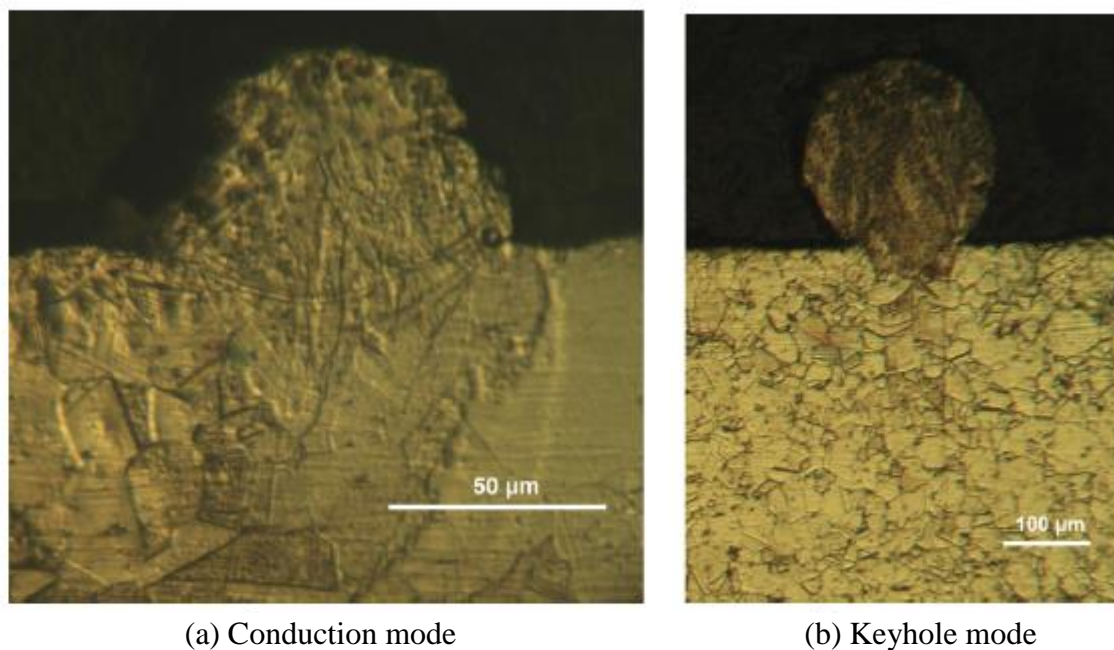


Figure 12. Single-track scanning of 316L SLMed under parameters equaling the same VED [13]

However, measuring densities of as-printed samples using different volumetric energy density can provide a framework for establishing SLM parameters required to melt a particular metal. Low VED values can result in a balling effect, in which the powder on the surface melts and forms agglomerates but does not fuse to the previous layer (or build platform) [33]. Balling causes disruptions in melt pool continuity, resulting in uneven layers and high porosity. However, higher VED does not directly lead to higher density of SLM components. If the VED is too high, temperatures within the melt pool can reach a boiling point, resulting in “keyhole mode” in which the metal is vaporized [13]. Keyhole mode is recognizable in SLMed samples by the characteristically deep and narrow melt pool, and a tall track height with a low contact angle as shown in Figure 13b.



(a) Conduction mode (b) Keyhole mode
Figure 13. (a) conduction mode and (b) keyhole mode in SLM of 316L as demonstrated by Bertoli *et al.* [13]

This shape is due to the recoil pressure of the vapor, which has been studied and modeled by Khairallah *et al.* [31]. As reported by Bertoli *et al.* [13] continuous, conduction mode melt tracks for a single layer of powder was achieved at VED values between 100-242 J/mm³. According to Cherry *et al.* [33], the optimal energy density to minimize porosity was identified to be 104.52 J/mm³.

While VED can be used to help predict the continuity of a single melt track, other parameters must be considered to produce high-density SLMed parts for SLM and to ensure full, uniform melting and sufficient overlap between tracks. These parameters include hatch spacing, shift angle, build orientation, and gas atmosphere. Each of these parameters are explained in the following sections.

2.5.2. Hatch Spacing

Hatch spacing refers to the distance between the center of two parallel melt pools in an SLM scanning pattern. Because some spreading of molten metal occurs during scanning, the width of the melt pool can often be larger than the designated spot size of the laser [13]. Therefore, a hatch spacing set equal to spot size for sufficient VED in conduction mode can often provide enough overlap to have bonding between the scanning tracks.

Liverani *et al.* [4] demonstrated that for a 50 µm spot size, with power levels ranging from 100 to 150 W, and scan speed constant at 700 mm/s, little difference in density and microstructure was shown between hatch spacing of 50µm and 70µm. Too wide of a hatch spacing can lead to grid-like porosity in the solid. If hatch spacing is too narrow, time could be wasted spent on unnecessary powder re-melting. The micrograph in

Figure 14 from Casati *et al.* [34] shows the importance of hatch spacing, where the width must be wide enough to form fusion zones such as regions 1 and 3 in Figure 14b.

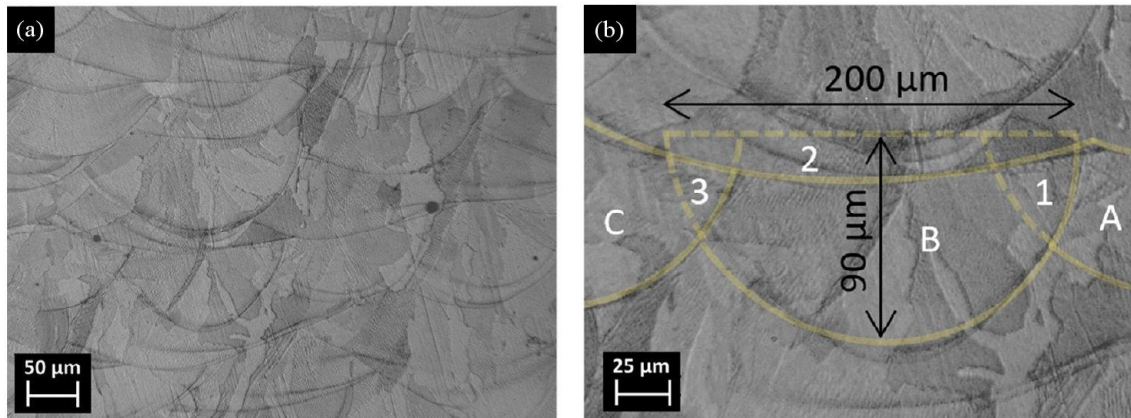


Figure 14. (a) Lateral cross section of 316L parts built by SLM and (b) cross section of melt pools overlap [34]

2.5.3. Layer Thickness

The necessary layer thickness of spread powder in SLM is dependent on the depth of penetration of the melt pool. The longest lead time in the SLM process is during raising and lowering of the platform and spreading each layer of powder. Faster scan speeds can help save some manufacturing time [35], and efficiency could be improved with reducing the number of layers in a part. In other words, if significantly thicker powder layers could be achieved in SLM without sacrificing density or another aspect of part quality, time and money could potentially be saved [36].

2.5.4. Shift angle and Scanning Strategy

Shift angle refers to the angle by which each subsequent powder layer rotates relative to the previous one. It is common to use a shift angle of 45° [5,34] or 90° [33–35], although in some studies, irregular angles have proven effective in ensuring uniform melting and limiting excessive re-melting. An example of this is the 67° shift angle used by Casati *et al.* [34], and Wang *et al.* [36]. Scanning strategy beyond a simple back and forth laser path can also play a significant role depending on component size. For smaller components, it may be sufficient to use a single back-and-forth scanning pattern, whereas if the part is larger, a “checkerboard” pattern, composed of multiple squares containing back and forth strategies may be necessary for even distribution of heat and therefore more isotropic properties [39].

2.5.5. Gas Atmosphere

Because SLM involves high-temperature laser contact with highly combustible metal powders, an inert atmosphere with extremely low oxygen is crucial to work with. High oxygen levels in the build chamber pose a hazard to health and safety and lead to the formation of oxides and other compounds that can influence the mechanical integrity of a component [40]. Most SLM systems are operated under argon atmosphere [11, 37, 40-41]. According to a study from Zhang *et al.* [3], nitrogen performs nearly as well as argon under typical SLM parameters. Nitrogen tends to be less expensive and more readily available, making it a promising alternative to Argon as an atmospheric gas. As shown in Figure 15, nitrogen is comparable to argon in both measured density and porosity.

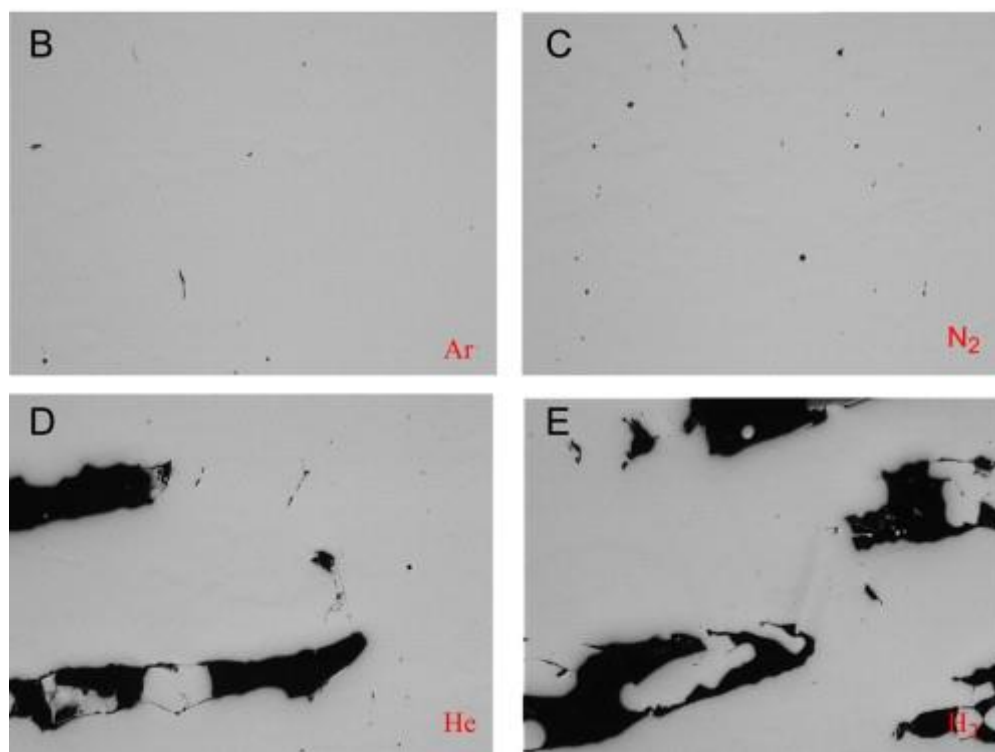
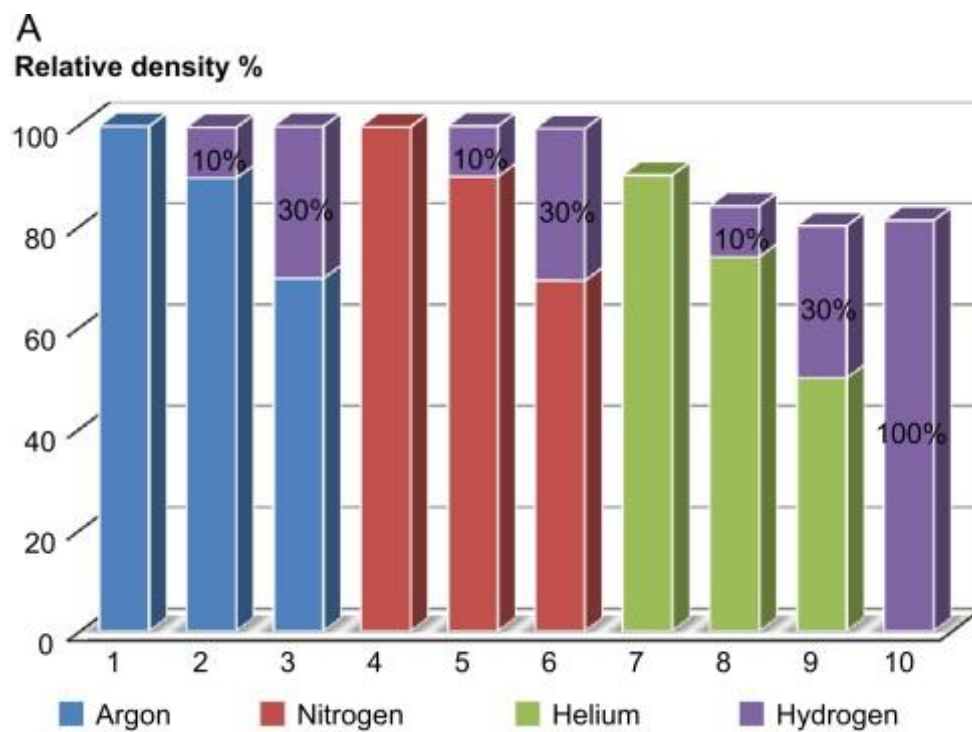


Figure 15. (a) Density of samples SLMed under various atmospheres and resulting sample porosity for (b) argon, (c) nitrogen, (d) helium, and (e) hydrogen

2.6. Phase Composition

Many of the desirable properties of 316L are attributed to its fully austenite phase [4]. Due to the low carbon content in 316L (less than 0.3 % carbon) and high thermal gradients in SLM, material cools quickly and remains well within the austenite regime after heating. Previous studies [42-43] used the x-ray diffraction (XRD) to demonstrate that precursor powder feedstock maintains a near complete FCC austenite phase before and after printing. This is shown in Figure 16.

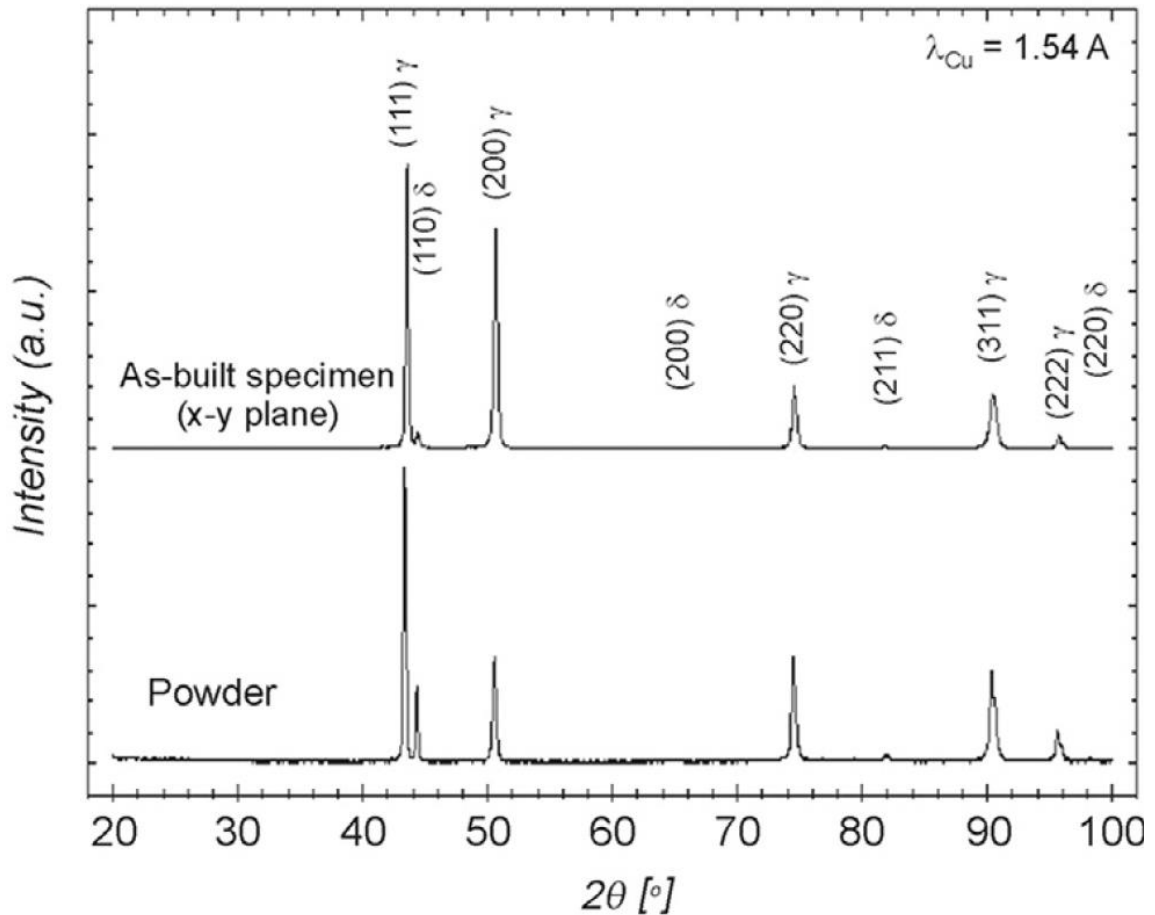


Figure 16. XRD pattern obtained from 316L powder and SLMed part [43]

While the dominant phase in both gas-atomized powder and SLM-processed 316L is austenite (γ), slight secondary ferrite (δ) peaks have been demonstrated for powder feedstock, as shown in Figure 16 [35, 43]. This δ -ferrite phase appears to be eliminated during SLM processing, resulting in a fully austenite phase in the SLMed material. Furthermore, according to Bartolomeu *et al.* [45], the austenite phase in powder and SLMed samples has been shown to be comparable to austenite phase in 316L parts manufactured by casting or hot pressing, as shown in Figure 17.

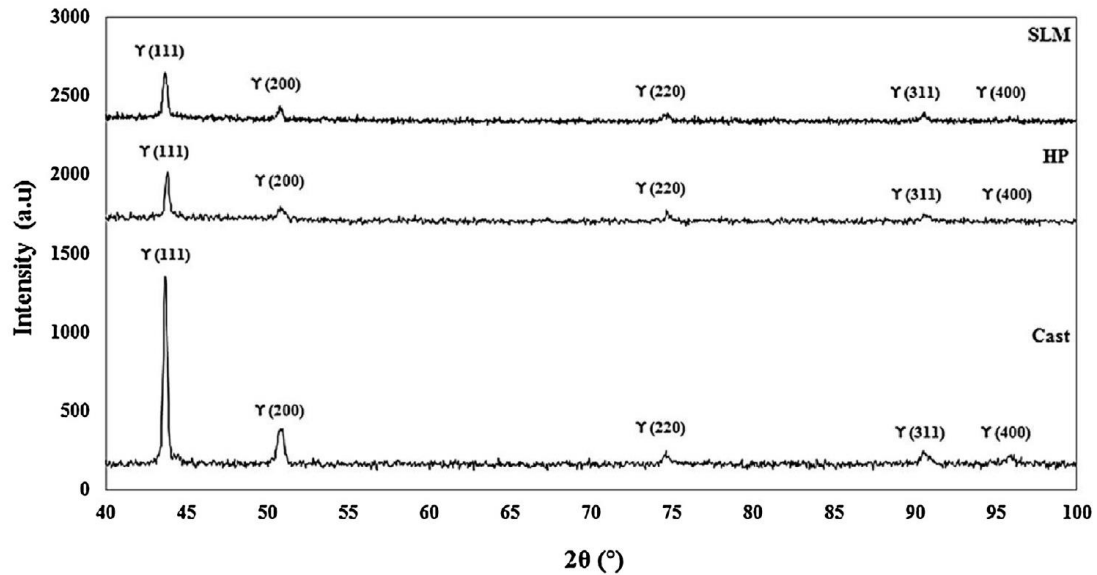


Figure 17. XRD plot showing diffraction peaks indicating a fully austenite phase for bulk samples produced by SLM, hot pressing, and casting [45]

2.7. Microstructure and Melt Pool in SLM

Electron backscatter diffraction (EBSD) shows the orientation of different grains where they have grown within the melt pool, as seen in Figure 18. Grain direction is

represented by color and the direction of grains in relation to the melt pool can be seen by the dotted lines outlining the melt pool.

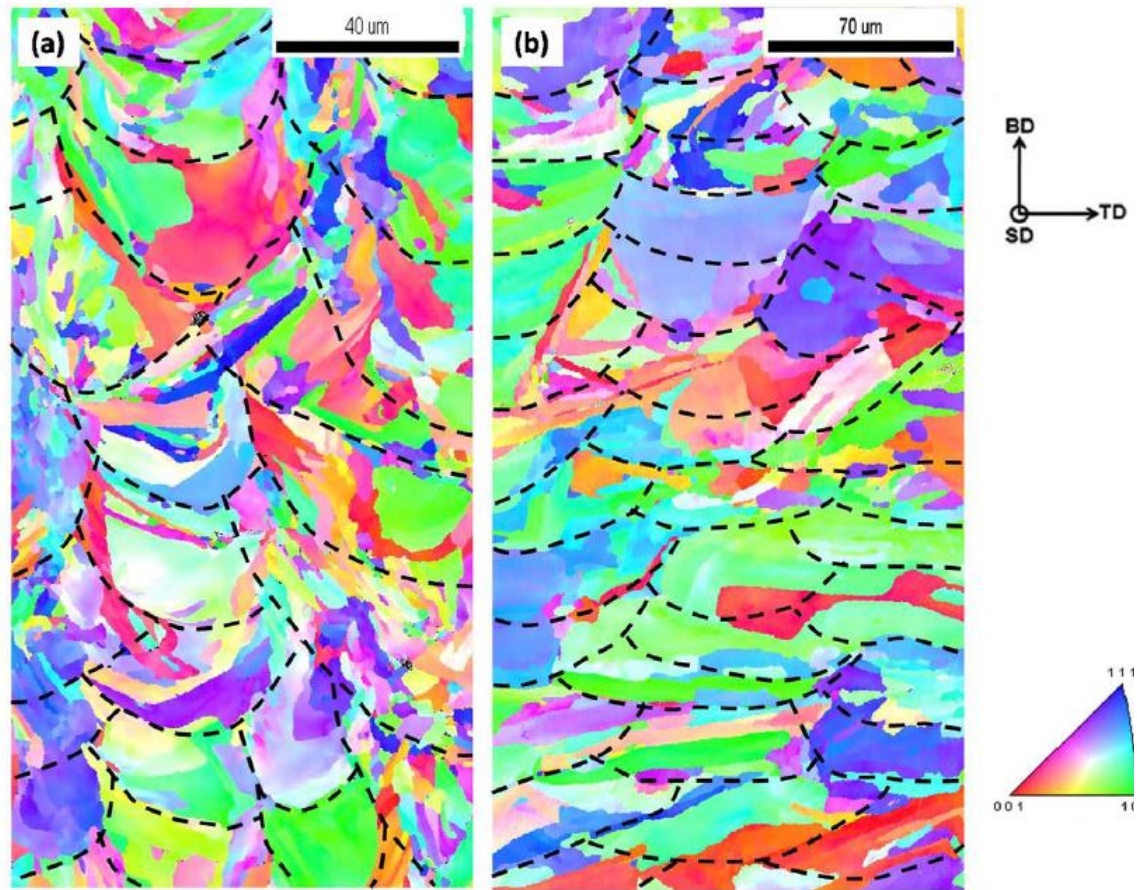


Figure 18. EBSD micrograph of melt pool and microstructure in SLMed 316L. Dotted lines show the geometry of the melt pool [39]

The melt pool structure created by SLM melt tracks layered upon each other is shown in Figure 19a. The microstructure of 316L produced by SLM is characterized by columnar and cellular grain structure as shown in Figure 19b-c. The aspect ratio of some layers compared to others shows the different cross-sections of melt tracks visible as a result of shift angle and alternating scanning orientations [44].

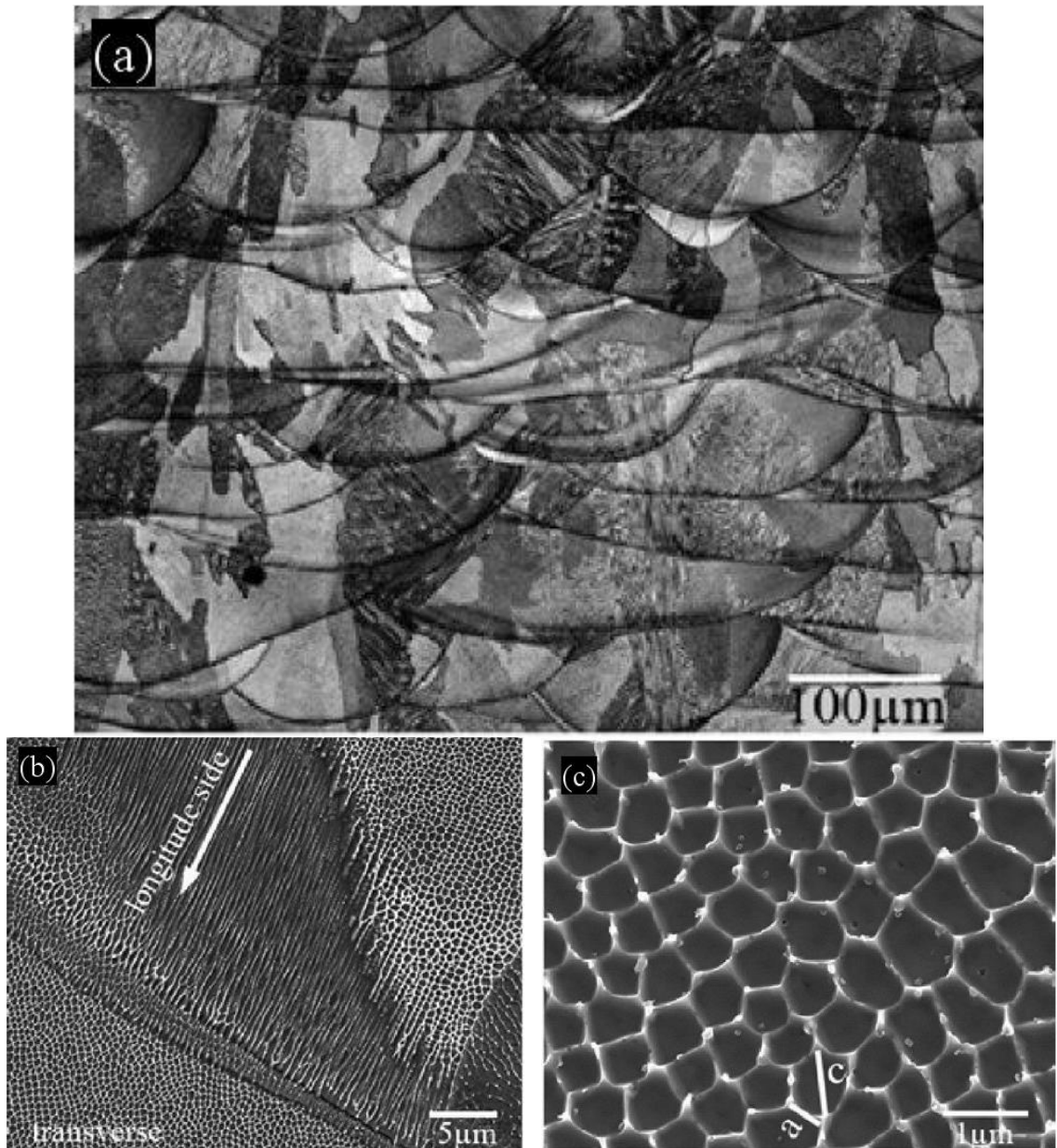


Figure 19. SLMed 316L: (a) Melt pool geometry showing grain structure and (b)-(c) characteristic microstructure showing intergranular cells [44]

2.7.1. Intergranular Cells

Intergranular cells, such as those shown in Figure 19, are formed as a result of high thermal gradients in the molten metal caused by the high temperature of the laser and rapid cooling of the melt pool during SLM, leading to a highly refined microstructure [39]. The size of these cellular arms can be quantified by the average distance between the centers of adjacent parallel cells, known as the primary cellular arm spacing (PCAS) [12]. For a typical austenitic stainless steel, primary cellular arm spacing, λ_l , (i.e. the average distance between the center of each intergranular cell) is calculated by Equation 15 as follows [46]:

$$\lambda_l = 80\dot{T}^{-0.33} \quad \text{Equation 15}$$

Where \dot{T} is the cooling rate in K/s.

2.7.2. Columnar Grains

Metallic grains in 316L that has been processed by laser melting are uniquely columnar in shape [47]. According to Tucho *et al.* [48], these columns have a tendency to grow in the direction normal to the boundary of the melt pool, but fluid flow within the molten melt pool can alter the orientation of grain growth, as shown in Figure 19 [42]. In more traditional melting and solidification processes, such as casting, the relationship between cooling rate and grain size is given by Equation 16 as follows [48-49]:

$$\lambda = a + \frac{b}{\sqrt{\dot{T}}} \quad \text{Equation 16}$$

Where λ is grain size, a and b are material constants, and \dot{T} is the cooling rate.

This traditional relationship does not accurately describe the anisotropic grain growth behavior in SLM due to the unique columnar grain structure that develops. By measuring the grain size of multiple samples over a range of VED values, and deriving a mathematical model for their results, Ma *et al.*[12] found that the solidification of an alloy by SLM can be more accurately described by the cubic function in Equation 17:

$$\lambda = \frac{a}{(\sqrt{\dot{T}})^3} + \frac{b}{(\sqrt{\dot{T}})^2} + \frac{c}{\sqrt{\dot{T}}} + d \quad \text{Equation 17}$$

Due to the high aspect ratio of these grains, a separate set of constants are required for this equation to describe the width of the grain, w , and the length, L of the grain, respectively. From experimental results, Ma *et al.* [12] derived values for the constants for a , b , c , and d to provide the calculation for grain width and length as a function of cooling rate in Equation 18 and 19 as follows:

$$w = \frac{5.9 \times 10^9}{(\sqrt{\dot{T}})^3} + \frac{2.6 \times 10^7}{(\sqrt{\dot{T}})^2} + \frac{4.2 \times 10^4}{\sqrt{\dot{T}}} + 1.6 \quad \text{Equation 18}$$

$$L = \frac{1.7 \times 10^{11}}{(\sqrt{\dot{T}})^3} + \frac{6.2 \times 10^8}{(\sqrt{\dot{T}})^2} + \frac{8.2 \times 10^5}{\sqrt{\dot{T}}} + 117.5 \quad \text{Equation 19}$$

2.7.3. Porosity

Porosity in SLMed components is generally attributed to insufficient or overpowered VED causing difficulty in the bonding process [13, 38]. Regardless of the cause, even a small percentage of porosity reduces density and introduces weak points in the material. Figure 20 shows variations in porosity by orientation to build direction, and variations in scanning strategy [39].

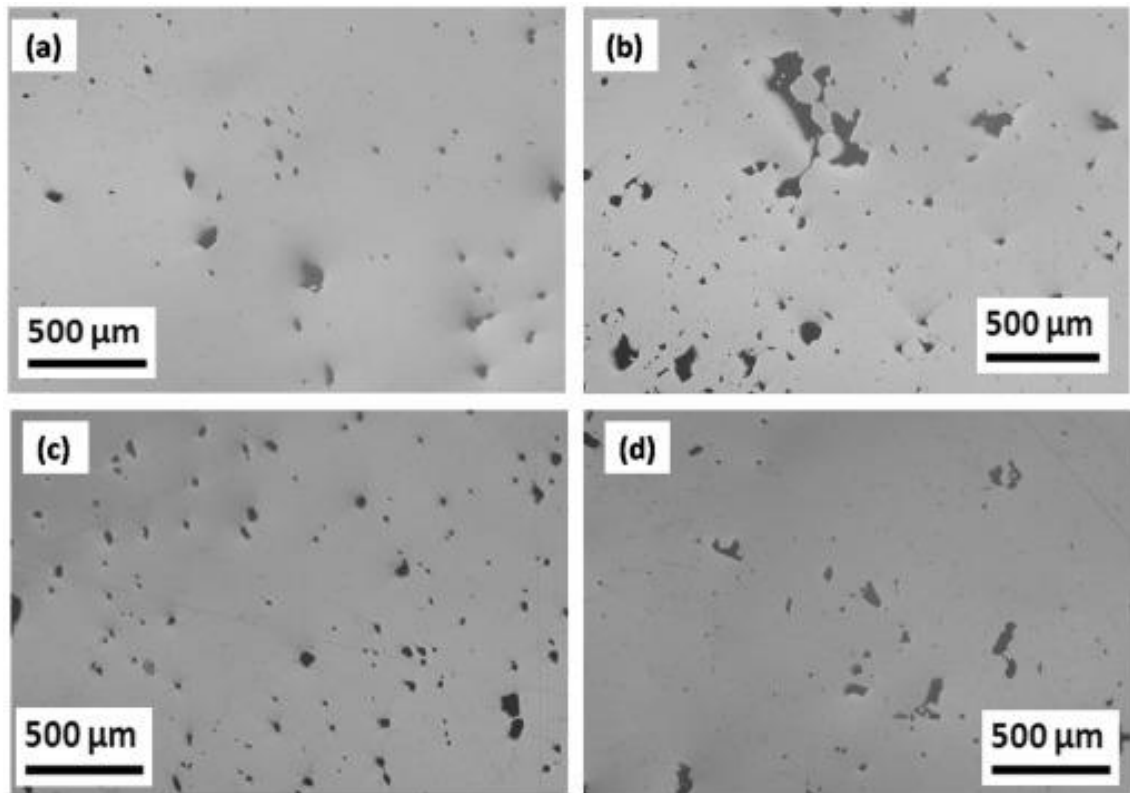


Figure 20. Porosity in SLMed 316L (a) parallel to the build direction with a single orthogonal shift melt pattern, (b) normal to the build direction with a single orthogonal shift melt pattern, (c) parallel to the build direction with a checkerboard scanning strategy, (d) normal to the build direction with a checkerboard scanning strategy. All are printed with same VED (90W, 1000mm/s, 150μm hatch, 30μm layer) [39].

2.8. Density

As mentioned in the previous section, lower density in an SLM component is caused by porosity and voids. An effective way to determine the density of a solid object is by the Archimedes method. This method uses principles of buoyancy, given by the relationship in Equation 20, to calculate the object's density from its weight in air, m_1 , and its weight, m_2 , in an auxiliary liquid of density ρ_{liquid} (typically, DI water). Normalized using the density of air at ambient temperature (ρ_{air}), the density can be calculated as follows [51]:

$$\rho_{solid} = (\rho_{liquid} - \rho_{air}) \left(\frac{m_1}{m_1 - m_2} \right) + \rho_{air} \quad \text{Equation 20}$$

2.9. Hardness

The Vickers microhardness of standard wrought, annealed 316L stainless steel is typically around 200HV [43]. Previous studies[4, 12, 32, 44, 47] have found that despite some deviation, hardness values for ~99% density SLMed 316L tend to be higher (210-278 HV) than wrought 316L. Hardness of samples processed by SLM have been shown to be directly affected by the VED [12, 33, 48]. Cherry *et al.* [33] suggests maximum microhardness, around 225 HV, at optimum VED (125 J/mm³). However, Ma *et al.* [12] found that hardness decreased with increasing energy density, with hardness values ranging approximately 240-278 HV. Tucho *et al.* [48], reported hardness of 179-213 HV at VED of 50-125 J/mm³.

As demonstrated in a study by Liverani *et al.* [4], hardness has been shown to vary from the top of a build to bottom. Values further from the build plate were found to be around 240 HV, whereas lower parts had hardness values as low as 210 HV. Additionally, Tucho *et al.* [48] reported higher hardness values measured across surfaces normal to the SLM build direction. This result is anticipated, as the study also showed hardness decreasing with increasing porosity, and the surface parallel to the build direction tends to have greater porosity due to gaps in inter-layer bonding.

Ma et al found that the Hall-Petch relationship between hardness and grain width, w , for fine grains in SLM was linear according to the following function in Equation 21:

$$H = 152 + 498w^{-0.5} \quad \text{Equation 21}$$

Where H is the Vickers microhardness (HV) and w is the width of the grain in μm . This allows the theoretical grain width to be calculated according to Equation 22 as follows:

$$w = \frac{2.48 \times 10^5}{(H-152)^2} \quad \text{Equation 22}$$

2.10. Design Advantages of SLM

Complex shapes, only plausible through additive manufacturing, can form lattices, like the examples in Figure 21. These lattice structures can be used to replace heavy, consolidated materials for applications like the aerospace industry, where every ounce

counts [50–52]. While accidental porosity can be a negative property, controllable porosity through organized lattices can lend strength properties while reducing weight [54].

As a biocompatible material, 316L can be printed in the complex shapes for making lightweight and bio-shaped prosthetic components. Easily customizable to different bodies and body parts, complex geometry again allows weight-reducing designs to be possible, limiting the impact and wear on natural bone and tissue and matching the mass of a natural bone [55].

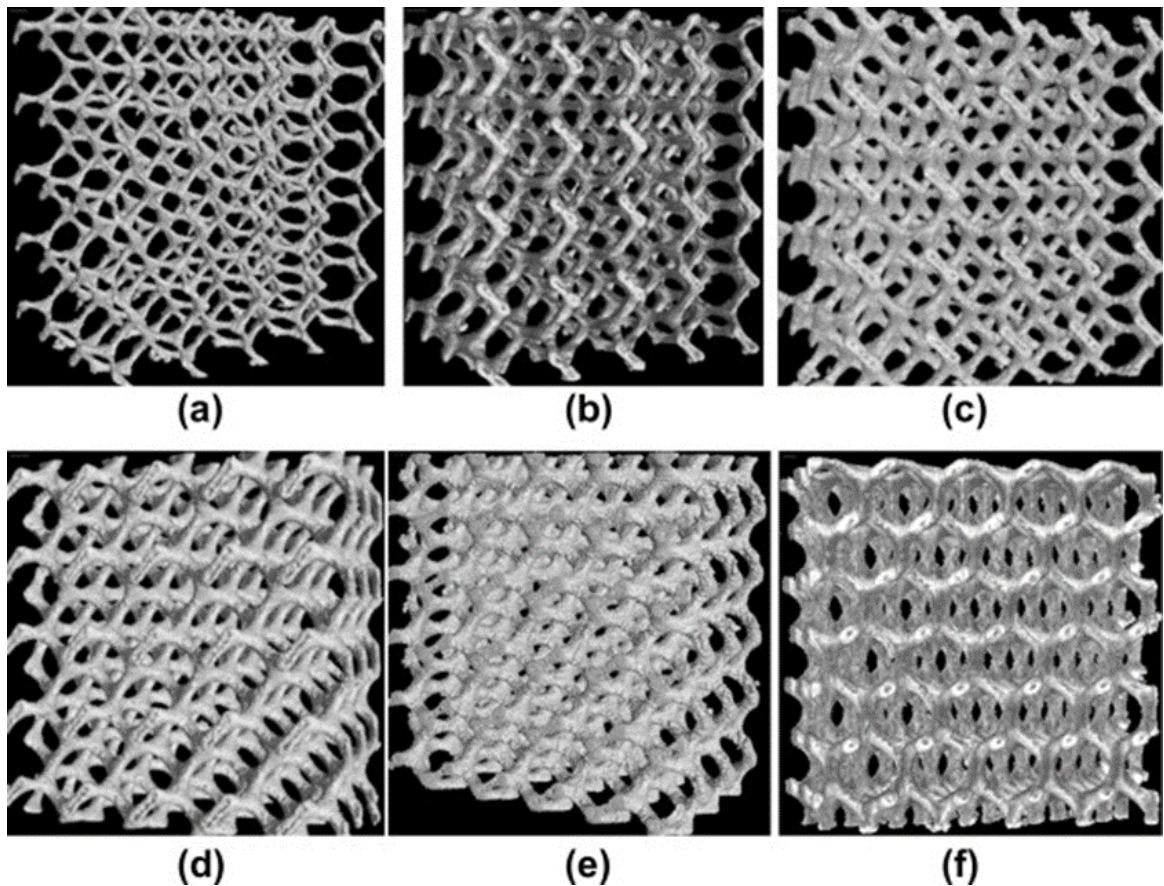


Figure 21. Example metal lattice structures that can be constructed using SLM for weight- reducing applications [43]

Mechanical properties were improved in SLMed 316L steel even at high temperatures [4, 39, 45, 54]. In a study by Bartolomeu *et al.* [45], SLMed components were found to have up to 41% higher yield strength and as much as 144% higher tensile strength than cast 316L. Suryawanshi *et al.* [39] found, however, that SLM only provided a marginal improvement in tensile strength from “conventional machining”, but yield strength was found to be higher. These improvements are largely dependent on process parameters and resulting microstructure, but overall, 316L appears to have increased some aspects of its value for many applications through the assistance of SLM.

Chapter 3 - Materials and Methods

In the following chapter, the methods and experimental equipment used to evaluate powder size, density, flow, and phase composition are described. This chapter includes methods of measuring the density and hardness of SLMed samples, as well as preparing and evaluating the samples for porosity, microstructure, and phase composition. Furthermore, post processing of SLMed samples, including removal of support structures and annealing of the samples, are described.

3.1. Powder

Mixing ratios and packing density were determined for two size distributions of Oerlikon Metco gas-atomized 316L spherical powder (OM and OM-2). These larger powders were then combined with small, morphologically irregular 316L powder procured from US Research Nanomaterials (USRN-A) to produce two powder mixtures having a bimodal particle size distribution (Bimo-1 and Bimo-2). This process was then repeated for a single-mode, gas-atomized 316L powder supplied by GKN Hoeganaes (GH), combined with a more spherical water- and gas-atomized small powder from US Research Nanomaterials (USRN-B) to create a third bimodally-distributed batch of powder (Bimo-3)

Table 2 – Naming convention and size range of each powder type

Abbreviation	Vendor	Size
OM	Oerlikon Metco	15-45 μ m
OM-2	Oerlikon Metco	38-45 μ m
GH	GKN Hoeganaes	18-53 μ m
USRN-A	US Research Nanomaterials	~5 μ m
USRN-B	US Research Nanomaterials	~5 μ m
Bimo-1	(OM) + (USRN-A)	
Bimo-2	(OM-2) + (USRN-A)	
Bimo-3	(GH) + (USRN-B)	

3.1.1. Chemistry

The powder feedstock used in this research is 316L stainless steel with several different particle size distributions, each from a different supplier reporting marginally different alloy compositions. Table 3 gives the nominal composition reported by the manufacturer of each powder type used in this study.

Table 3 – Composition of powders reported by manufacturer (wt%)

Supplier	Fe	Cr	Ni	Mo	Si	Mn	C	Other*
OM	Balance	17.0	12.0	2.5	2.3	1.0	0.03	<0.5
GH		16.6	10.7	2.4	0.35	1.5	0.02	-
USRN-A		16.5	12.4	2.6	0.5	0.075	0.02	< 0.013
USRN-B		16-18	12-15	2-3	<1	<0.3	<0.03	-

Incidental elements with concentrations low enough to be designated as “other” for some manufacturers have been included in composition reports by other powder suppliers. These concentrations are given in Table 4. It should be noted that even in small quantities, these nonmetallic elements can influence the properties of the alloy.

Table 4 – Concentration of “*other” nonmetal elements reported in powder (wt%)

Supplier	O	S	N
OM	-	-	-
GH	0.06	0.007	0.06
USRN-A	0.337	-	-
USRN-B	<0.15	-	-

3.1.2. Powder Size

Important values for particle size distributions available from each manufacturer are given in Table 5

Table 5– Particle size distribution of 316L procured from various powder manufacturers

Particle size	OM	OM-2	GH	USRN-A	USRN-B
D ₁₀	23.1	30.0	18.22	2.55	-
D ₅₀	34.7	38.2	36.31	5.68	5.52
D ₉₀	51.3	48.2	53.97	9.33	-

As summarized in Table 5, a second set of OM powder, OM-2, was made by sieving the original OM powder using a Humbolt H-4325 mechanical sieve shaker with Gilson ASTM E11 standard test sieve mesh from 325 to 400 (shown in Figure 22), to obtain a particle size distribution between ~38µm and 45µm. Powder OM-2 has a narrower size range compared to the OM powder as shown in Table 5.



Figure 22. Sieve shaker and stacks of standard sieve used to separate narrow particle size distribution OM-2

3.1.3. Powder Density and Flow Measurement

Apparent density of the powders was measured by pouring powder through a Hall flow cone into a container with volume of 25 cm^3 , as shown in Figure 23a and measuring the mass of the volume after leveling. Apparent density of a bulk powder is often similar to the density of a spread powder bed [6].

Fractional packing density, f , was determined from the tap density of the powders with an assumed material density of 8.0 g/cm^3 . Tap density was measured according to standard procedure ASTM B527 [56] using a Quantachrome Autotap AT-6-110-60 mechanical tapper with a 100 mL graduate cylinder as shown in Figure 23b. The theoretical optimal mixing ratio of large and small particle sizes was calculated using tap density according to Equation 12.

The Hausner ratio, calculated as the ratio of tap density to apparent density, was calculated and used as an indicator to compare flow properties of each powder type.

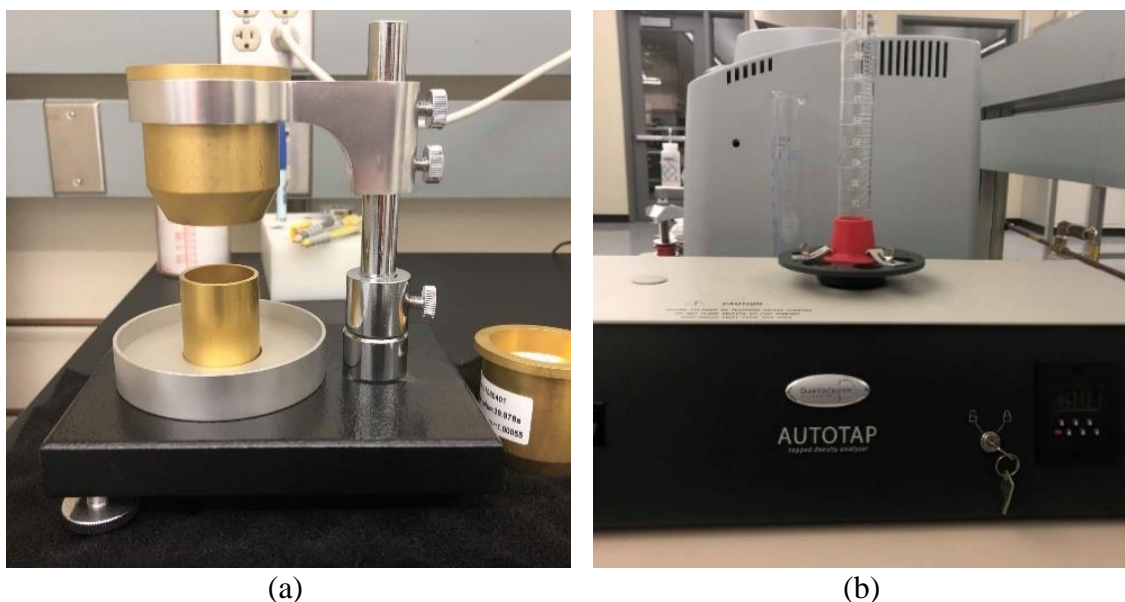


Figure 23. (a) Hall flowmeter for apparent density measurement and (b) Quantachrome Autotap AT-6-110-60 mechanical tapper with 100 mL cylinder for tap density measurement

3.1.4. Spreading Density

It is very important and of potential industrial application to establish a simple, inexpensive and repeatable technique to test the spreadability of a powder for the SLM process. In order to do so, the approach was to mimic the behavior of metal powder during spreading and measure the density of the metal after spreading, without rendering the test powder useless by melting it. This method offered a comparison between spread density and apparent or tap density of similar 316L powders in a range of sizes.

3.1.4.1. A Spreading Test Prototype Design

A prototype sample holder design consisted of multiple layers of laser-cut aluminum sheet with thickness of 0.016". A solid rectangle with dimensions of 2"x 3" served as the base plate. The subsequent layers, with the same outside dimensions, featured a 1.5" diameter circle laser cut from the center as shown in Figure 24a-c. Once stacked, these cut out pieces made up the "walls" of the "sample volume" to contain the spread powder to be measured.

For the preliminary test of the sample holder Hoeganaes water atomized 304 stainless steel powder with particle size $\sim 150\mu\text{m}$ (-100 mesh) was used. To test the spreading density of a single layer, one wall sheet was stacked on top of the base sheet to create a short "cylindrical volume". These two sheets were weighed together for the mass of the "container". Next, a small amount of powder was spread along one edge of the circular area as shown in Figure 24a. Using the flat straight edge of a hard plastic sheet, the powder was then drawn across the circular area in one direction with a slow, steady

motion to spread powder into the volume as shown in Figure 24b. Residual powder around the sample area was gently cleaned away using a fine brush so that powder only filled the area of the test volume as shown in Figure 24c.

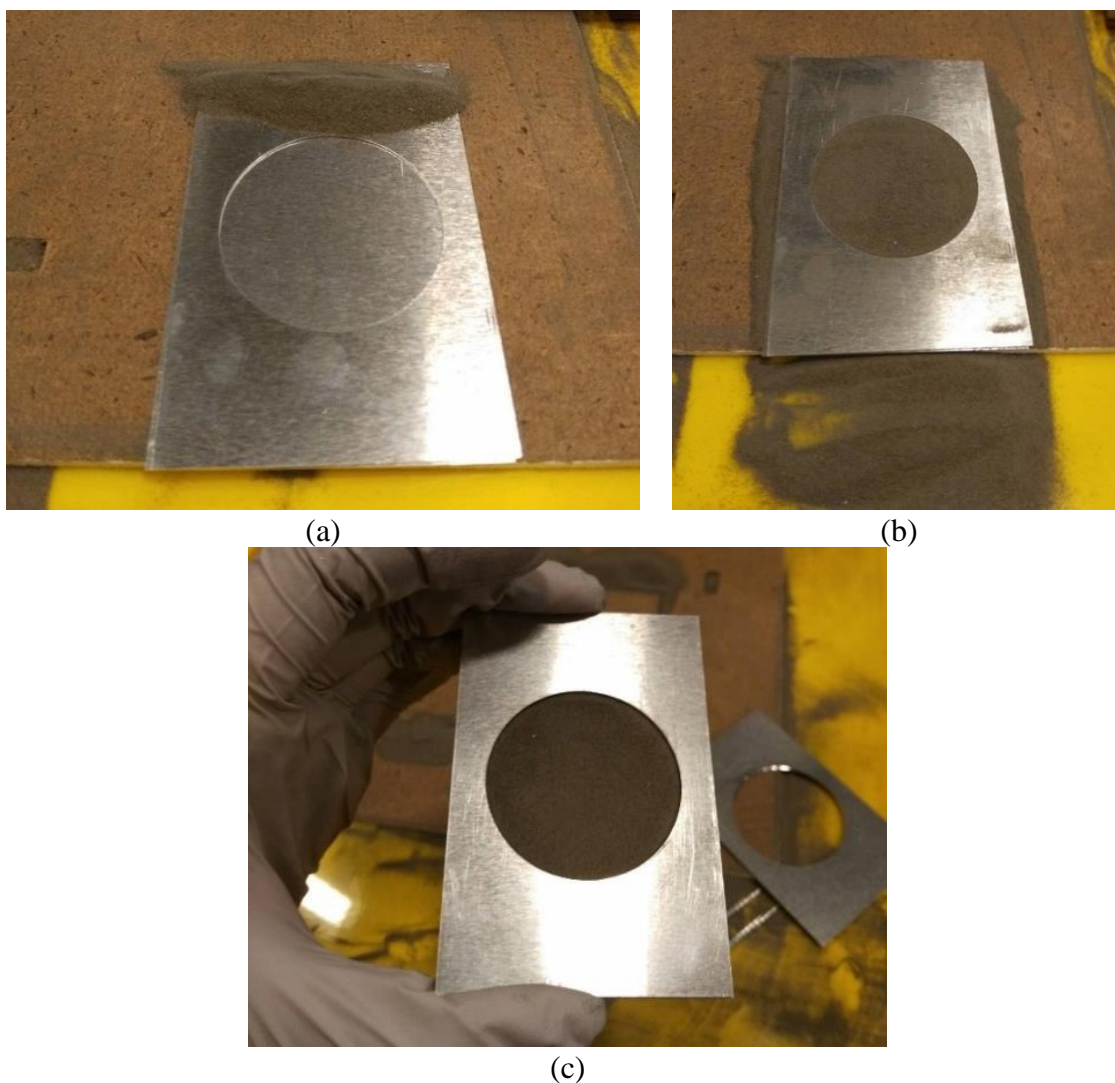


Figure 24. (a) Single wall layer with base before spreading, (b) after spreading and (c) sample holder after spreading a layer and cleaning surface of excess powder

The mass of a single layer of thickness $\sim 0.016''$ was then determined by measuring the mass of the sample and holder and subtracting that mass from the holder mass. For multiple layers, a new sheet was placed over the surface after brushing. Then, pouring and spreading process was repeated. Mass of each new sheet was added to the mass of the initial mass of the sample holder, and the thickness of the new sheet was added to volume height (the total of a three-sheet volume shown Figure 25a).

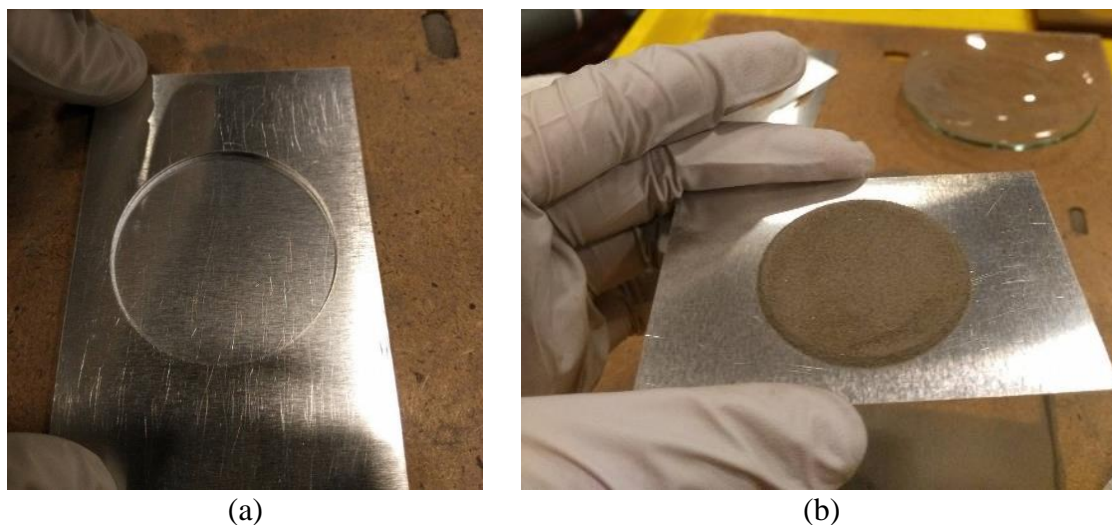


Figure 25. (a) Three layers for a total container height of $\sim 0.048''$ or $\sim 1.2\text{mm}$. (b) Powder volume and mass was measured after removing walls

Powder remained relatively within the boundaries of the volume formed by the stacked layers during the process, as shown in Figure 25b, indicating sufficient contact was achieved between base plate and sheets. It is reasonable to expect that contact between layers is not 100%, due to small particles remaining on the sheet surface before the addition of another layer.

3.1.4.2. Reduced Layer Thickness and Different Powder Grades

The above mentioned process was then repeated using laser-cut stainless steel sheets with a thickness of 0.114 mm. For these thinner sheets, the diameter of the circular wall section was 1.25". This sheet material was selected for its ability to remain rigid at smaller thicknesses, allowing it to be a promising option for simulating the SLM process. Three different size distributions of gas-atomized 316L stainless steel, ranging from $D_{50}=49\mu\text{m}$ to $D_{50}=89\mu\text{m}$, were tested for this layer thickness. The apparent, tap and spread density of these powders were measured to determine a relationship between spreading density and other powder density measurements.

3.1.5. Mixing Bimodal Powder from Constituent Powders

For the first two sets of larger powder (OM and OM-2), the D_{50} powder size was 34-39 μm . Both large powders were approximately 35 μm , and the small powder was approximately 5 μm , which, when mixed, approximately matched the 7:1 size ratio as determined by McGeary [7]. The “actual” ratio of D_{50} values for each bimodal powder size distribution is given in Table 6. The quantity of small powder to be mixed with larger powder was calculated according to Equation 12 in order to obtain maximum theoretical packing density in the bimodal mixtures and presented in Table 6.

Table 6 – Mixing ratios of three bimodal size distributions

Mixture	Large Powder	Small Powder	Bimodal Powder Ratio
Bimo-1	77.2 wt% OM	22.8 wt% USRN-A	6.1:1
Bimo-2	75.6 wt% OM-2	24.4 wt% USRN-A	6.7:1
Bimo-3	75.2 wt% GH	24.8 wt% USRN-B	6.6:1

Once the weight of each powder was measured, the bimodally distributed powders were mixed first by manually inverting the container for 50+ times, then mixing with a vortex mixer (as shown in Figure 26) for 30 seconds at ~3000 rpm. This was done in batches of ~ 500mL each, then the batches were combined, followed by additional 20+ inversions.

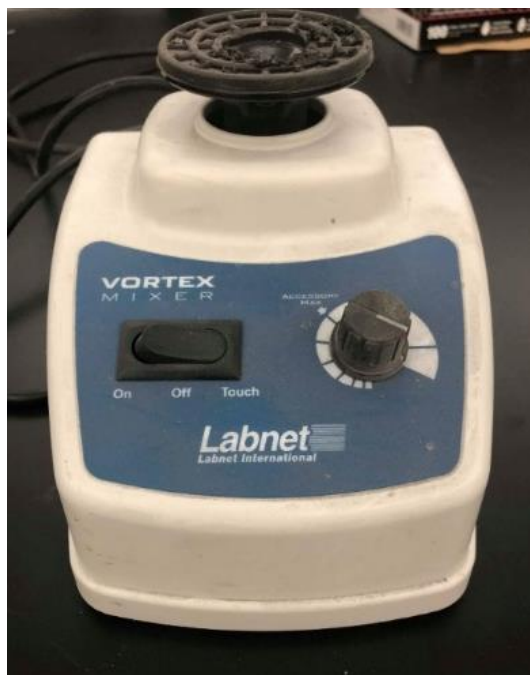


Figure 26. The vortex mixer used in this study to blend small and large powders to get a bimodal powder size distribution

3.1.6. Measuring Particle Size Distribution

Particle size distribution histograms were generated by laser diffraction in a wet suspension analysis using a Malvern Mastersizer 3000E particle analyzer as shown in Figure 27.

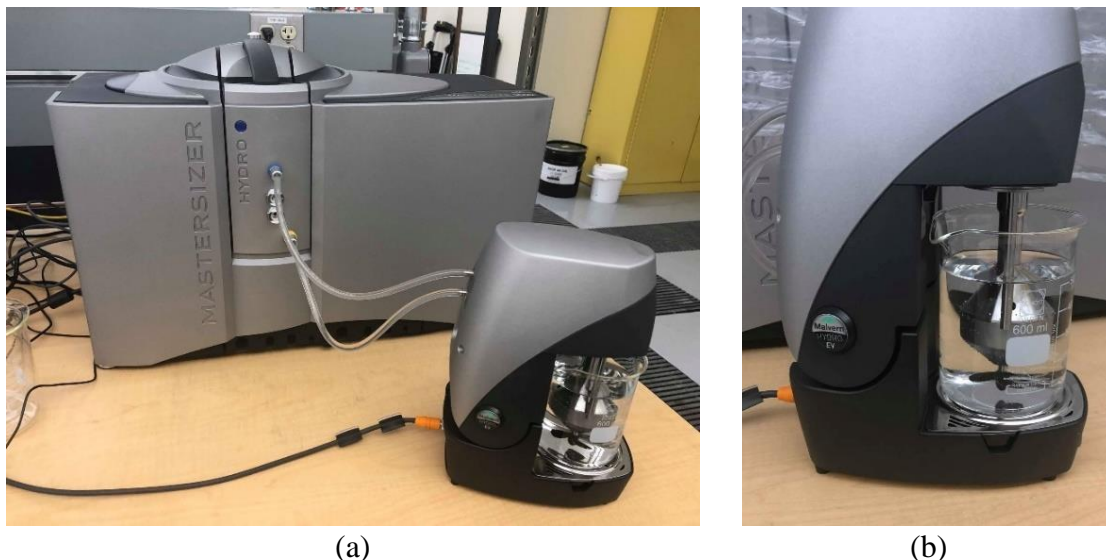


Figure 27. (a) Malvern MASTERSIZER 3000E particle size analyzer and (b) Hydro MV suspension mixer

To perform the measurement, metal powder was first mixed with deionized (DI) water into a thin slurry. Several drops of the slurry were then mixed into a 1000ml beaker of DI water with the Hydro MV until the beaker appeared faintly cloudy but still transparent. Then this dilute suspension was pumped through the Malvern analysis chamber while continuously mixed in the beaker as shown in Figure 27b. To determine how readily the powder were dispersed in water, 60 seconds of ultrasound titration was performed prior to the start of measurement until stable particle size distribution histograms were displayed.

3.1.7. Morphology

An FEI Quanta 600F environmental SEM was used to observe the morphology of powders. As shown in Figure 28, the larger set of powders (OM and OM-2) used in first

set of bimodal mixtures (Bimo-1 and Bimo-2) were primarily spherical with some irregularities where particles have fused together or small satellite particles have formed during the gas-atomization process. The small powders used in Bimo-1 and Bimo-2 were mostly irregular and contained large agglomerates.

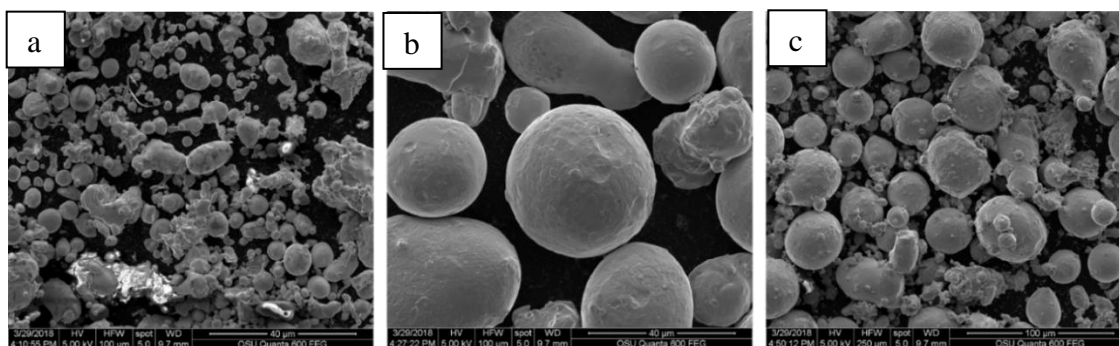


Figure 28. SEM micrographs of powders used in the first set of bimodal mixtures, (a) smaller, USRN-A, (b) larger powder OM and (c) the first bimodally distributed powder, Bimo-1

Figure 29 shows SEM images of the small (USRN-2) and large (GH) powders used in the third bimodal mixture, Bimo-3.

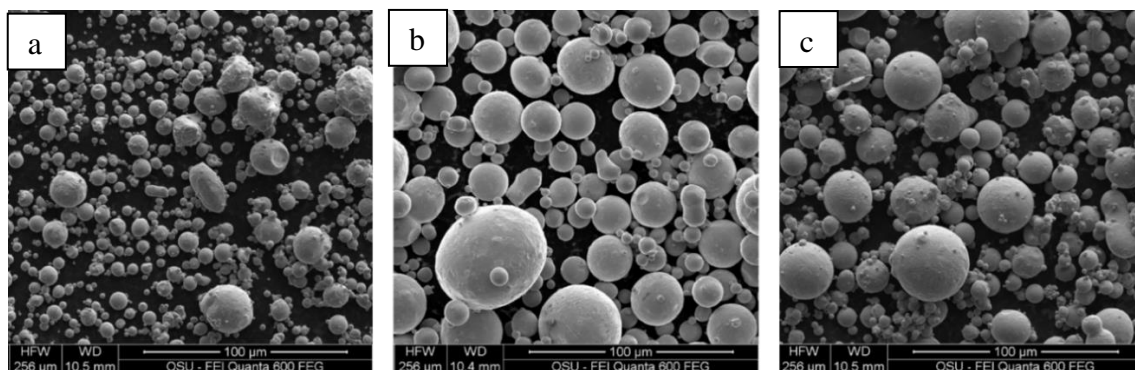


Figure 29. SEM micrographs of the powders used in the third bimodal mixture, including (a) the smaller, USRN-B (b) larger powder GH and (c) the third bimodally distributed powder, Bimo-3

The GH Powder morphology was spherical with minimal fused and satellite particles. The USRN-B powder, manufactured by water and gas atomization, was significantly more spherical and consistent than USRN-A. This improved sphericity is likely the reason for the manufacturer's designation that USRN-B is made for "3D printing", whereas USRN-A is labeled simply as "spherical 316L powder".

3.2. SLM Processing Parameters

SLM was performed using an OR LASER CREATOR SLM machine with a 1070 nm Yb Fibre Laser with 250W power under nitrogen atmosphere. Features of the build chamber in the Creator are shown in Figure 30.

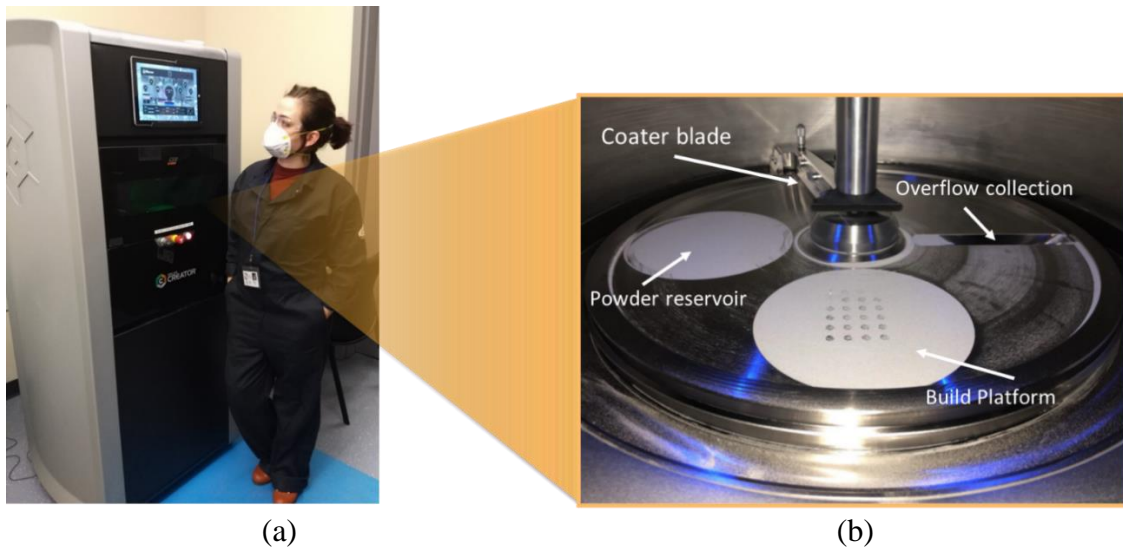


Figure 30. (a) ORLAS CREATOR SLM machine used in this study, (b) build chamber architecture in ORLAS CREATOR

The system uses a rotational spreading method to feed powder from the reservoir, across the build platform, and into the overflow collection chamber. The height-adjustable coater

arm is equipped with a replaceable rubber blade, to evenly spread powder across the build platform and ensure minimal wear on mechanical components. Oxygen content in the system cannot be controlled to a precise value. However, it was maintained below 0.1 vol%.

3.2.1. Volumetric Energy Density (VED)

In the first phase of SLM experiments, a set of $5 \times 5 \times 5 \text{ mm}^3$ samples were produced from OM single mode powder on a single build plate with different VED values by varying the power and scan speed of the laser. Figure 31 shows the layout of test sections on the build platform with different parameters printed simultaneously.

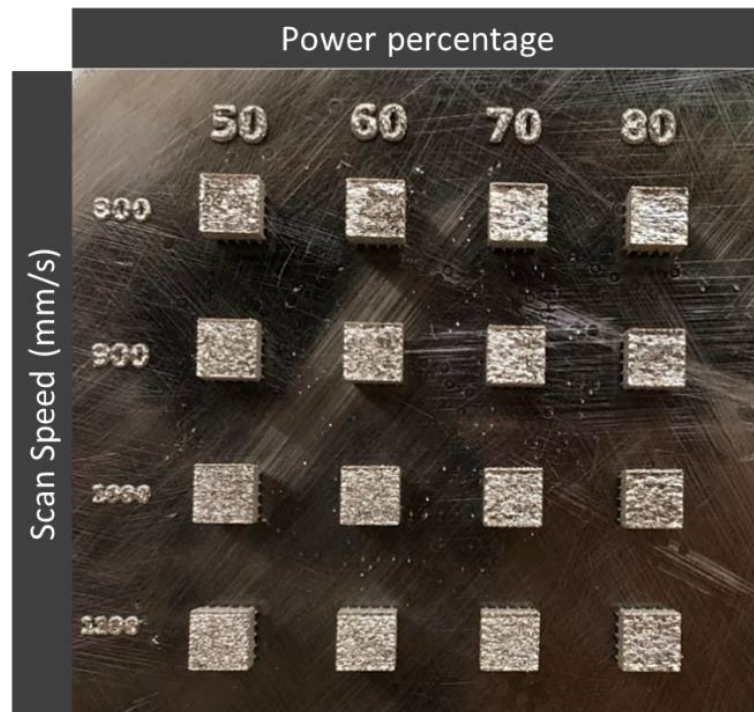


Figure 31. $5 \times 5 \times 5$ mm SLMed sample cubes with power% varying from 50-80% and scan speed varying from 700-1200 mm/s

For this machine, the power percentages shown in Figure 31 translate to the actual power given in Table 7.

Table 7 – Actual Power Level of Percent Machine Power				
Machine Setting (%)	50	60	70	80
Actual Laser Power (W)	107	139	178	203

The same set of parameters was used for Bimo-1 and Bimo-2 powders. Constant parameters that contribute to VED include spot size of 50 μ m, layer thickness of 50 μ m, and line spacing (hatch spacing) of 50 μ m. These and other parameters were constant throughout processing of all powder batches and are summarized in Table 8.

Table 8 – Constant SLM Parameters			
beam diameter	hatch spacing	layer height	shift angle
50 μ m	50 μ m	50 μ m	45°

In the second phase, the parameter set was expanded to include scanning speed values from 700 to 1200 mm/s. Rather than cubic samples, specimens from the second powder set were made to be cylindrical to distinguish build orientation in mounted samples. The expanded set of parameters with calculated VED values are given in Table 9.

Table 9 – Parameter Matrix with VED values

VED (J/mm ³)		Power (W)			
		107	139	178	203
Scan	700	61.1	79.4	101.7	116.0
Speed	800	53.5	69.5	89.0	101.5
(mm/s)	900	47.6	61.8	79.1	90.2
	1000	42.8	55.6	71.2	81.2
	1100	38.9	50.5	64.7	73.8
	1200	35.7	46.3	59.3	67.7

3.2.2. Support structures

Samples were built with support structures to ensure consistent layer spreading in the bulk of the sample, as well as to prevent warping of the sample geometry during melting. These supports were designed as 1 cm tall pillars with a cross-shaped cross-section. The total width of each cross-section was 1.5mm in each direction with a thickness of 0.5 mm, and each pillar was spaced in a grid pattern with 0.5 mm between each from edge to edge.

Samples were removed from the build plate with support structures still attached. This was done manually using a hammer and chisel to gently tap at the base of the support structure near its fusion to the build plate. After removal from build plate, support structures were removed from the bottom of each sample using a rotary diamond saw at 600 rpm.

3.2.3. Density Measurement

The density of each sample was measured using Archimedes method according to Equation 20. An OHAUSE PA84 digital balance equipped with an Archimedes density testing kit was used with DI water as shown in Figure 32.

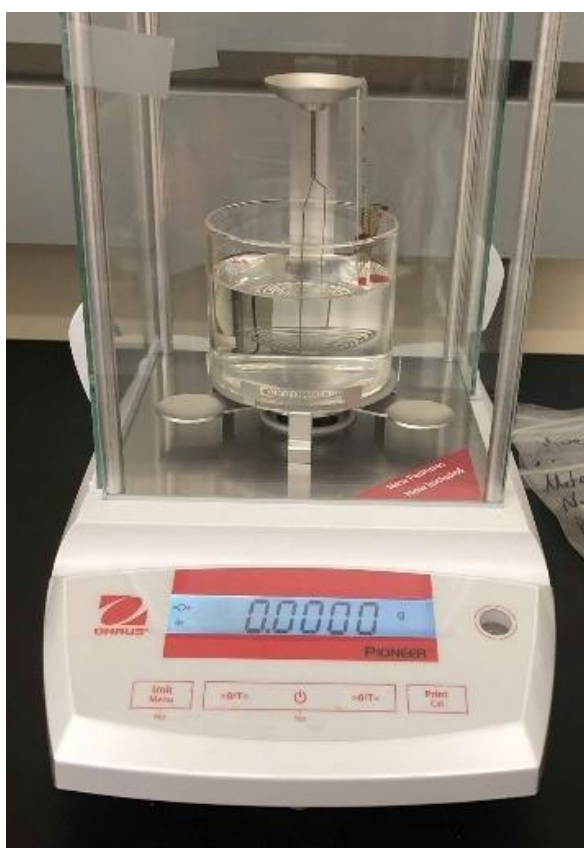


Figure 32. Digital balance equipped with Archimedes density kit for dry and liquid-submerged weighing

The differences in composition reported in Table 3 could significantly alter the accuracy of relative density measurements if the bulk density is assumed to be the same for all manufacturers. To ensure all powder and SLM component relative densities were

an accurate reflection of the parent material, bulk density was measured for each precursor powder by first *Arc Melting* an SLMed sample produced from each single mode and bimodal powder batch so that a full-density sample of each powder type was represented. Then, the density of these melted samples was measured using Archimedes method. Relative powder density and SLM sample densities shown in the results of this report are based on parent material densities recorded from these measurements.

3.2.4. Metallographic Sample Preparation

Microstructure analysis was carried out by cutting along planes normal and parallel to the build direction using a Pace Technologies PICO 155P precision cutter (as shown in Figure 33a) with circular diamond coated blade and at 600 rpm. Samples were then hot mounted at 370°C using a Pace Technologies TP-7001B pneumatic mounting press (Figure 33b). Mounted samples were then finished with 240, 400, 800, 1200 SiC grinding papers using a Pace Technologies NANO-2000T manual polisher at 150 rpm with a FEMTO-1100 rotating concurrently at 100 rpm. Then samples were polished by diamond suspension of 3, and 1 μm at 100 rpm. Some samples were polished in a 50 nm slurry using a vibratory polisher for 24hr. To reveal the microstructure, polished samples were then electro-etched in solution of 10% oxalic acid at 15V for 15 seconds.



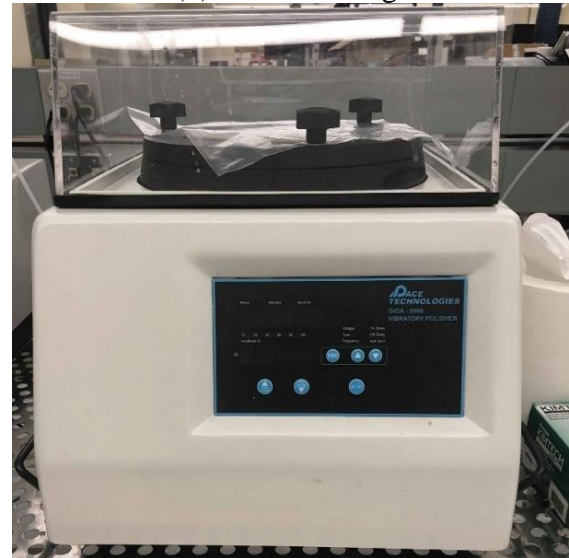
(a) Cutting



(b) Hot mounting



(c) Grinding/polishing



(d) Vibratory polishing

Figure 33. Metallography and sample preparation (a) cutting saw, (b) hot mounting, (c) grinding and polishing equipment and (d) vibratory polisher

3.2.5. Phase Identification

The phases present in both powder and bulk SLM samples were identified by X-ray Diffraction (XRD) using a Bruker D8 X-ray diffractometer. Continuous scanning mode was used to conduct scans at $2^\circ/\text{min}$ for a range of $2\theta = 20-90^\circ$.

3.2.6. Microstructure and Porosity Imaging

Optical microscopy and SEM imaging were used to observe the porosity and microstructure of SLMed samples produced from single mode (GH) and bimodal (Bimo-3) powder batches. Characteristics including %porosity, melt pool depth and grain size were helped to investigate interactions between the laser and the metal during the SLM process and provided insight into how VED influences physical characteristics of the components such as density and hardness.

Optical microscopy was used to observe melt pool shape and porosity. Using Image J software, the area fraction of pores was quantified and compared. SEM images of microstructure and finer porosity features were obtained using the same Quanta 600 machine used in powder imaging as described formerly in section 3.1.7.

3.2.7. Etching

Etched samples were observed under optical and SEM microscopy to observe and measure melt pool, the grain size, grain shape, and subgrain characteristics. Visible characteristics of the microstructure and melt pool were compared with anticipated results and XRD analysis.

3.2.8. Annealing

Selected samples were annealed by heating at a ramp rate of 8.5°C/min and holding for 2hrs at 1020°C under a nitrogen atmosphere. After annealing, samples were cooled in the furnace under nitrogen and then were polished and electroetched.

3.2.9. Hardness Testing

The hardness of each sample was measured using a Leco LM 248AT Vickers microhardness tester with three samples taken from the normal and build plane of each specimen. Loading was at done at 500g with a dwell time of 13 seconds. For each powder type and parameter set measured, 10 indentations were made to record the average hardness and standard deviation. These hardness values were used to calculate the theoretical grain size using the Hall-Petch relationship in Equation 21.

Chapter 4 – Results and Discussion

The following chapter summarizes the results of powder density and flow measurements, relative density of SLMed samples, investigation of porosity and microstructural characteristics, phase identification, and mechanical testing by Vickers microhardness measurement. The relevance of these results and how they relate to each other are discussed within this chapter as they appear.

4.1. Powder properties

As a reference for powders presented in the following results, definitions of powder abbreviations and ranges of size are reiterated in the table below:

Abbreviation	Vendor	Size
OM	Oerlikon Metco	15-45 μ m
OM-2	Oerlikon Metco	38-45 μ m
GH	GKN Hoeganaes	18-53 μ m
USRN-A	US Research Nanomaterials	~5 μ m
USRN-B	US Research Nanomaterials	~5 μ m
Bimo-1	(OM) + (USRN-A)	
Bimo-2	(OM-2) + (USRN-A)	
Bimo-3	(GH) + (USRN-B)	

The powder properties presented in these results include size distribution, tap density, apparent density, and Hausner ratio for flow characterization. Spread density of a separate set of powder batches was included for the purpose of comparing tap and apparent density to spread density to determine whether they represent a relevant metric for predicting

powder behavior during SLM. These results provide valuable insight into the cause of porosity and relative density of SLMed samples.

4.1.1. Powder Size Distribution

Particle size distribution analysis, performed using Malvern Mastersizer 3000E, showed that the fine powder (USRN-A), used in bimodal mixtures Bimo-1 and Bimo-2, followed a normal size distribution with $D_{50}=5.68\pm0.072\mu\text{m}$, as shown in Figure 34.

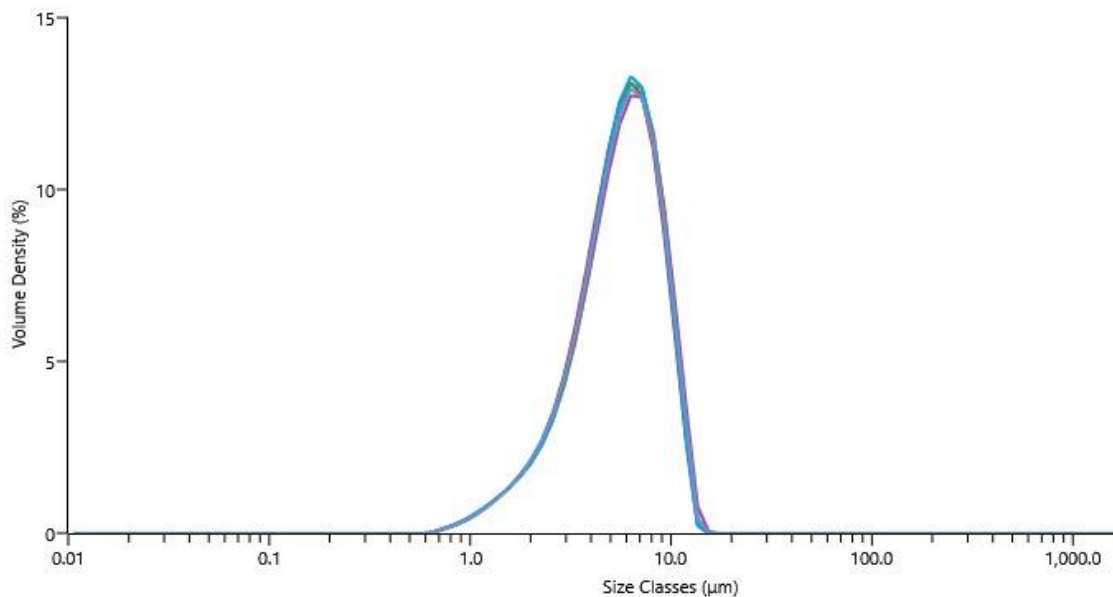
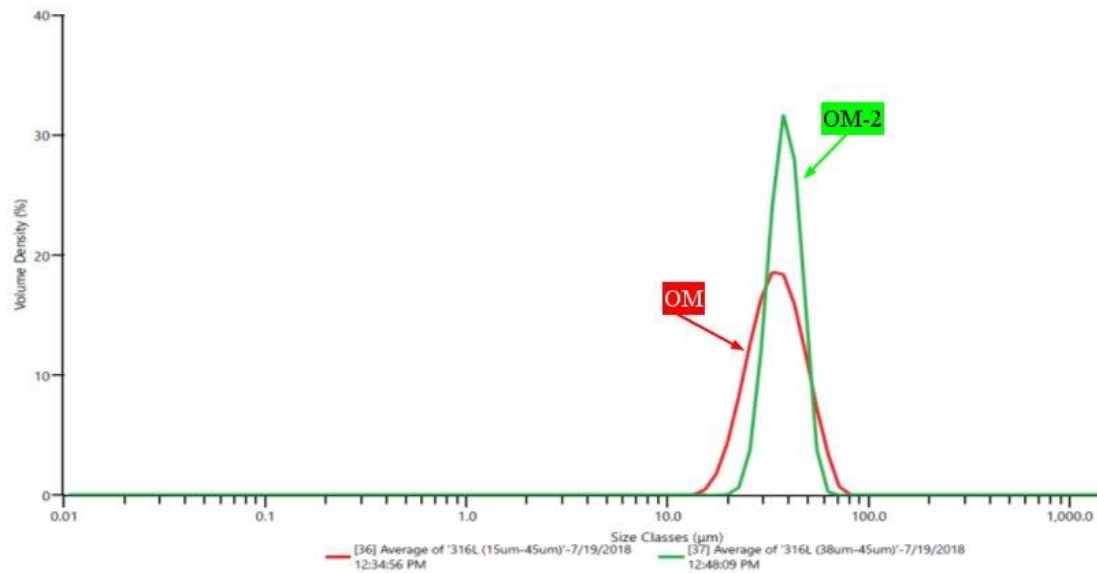


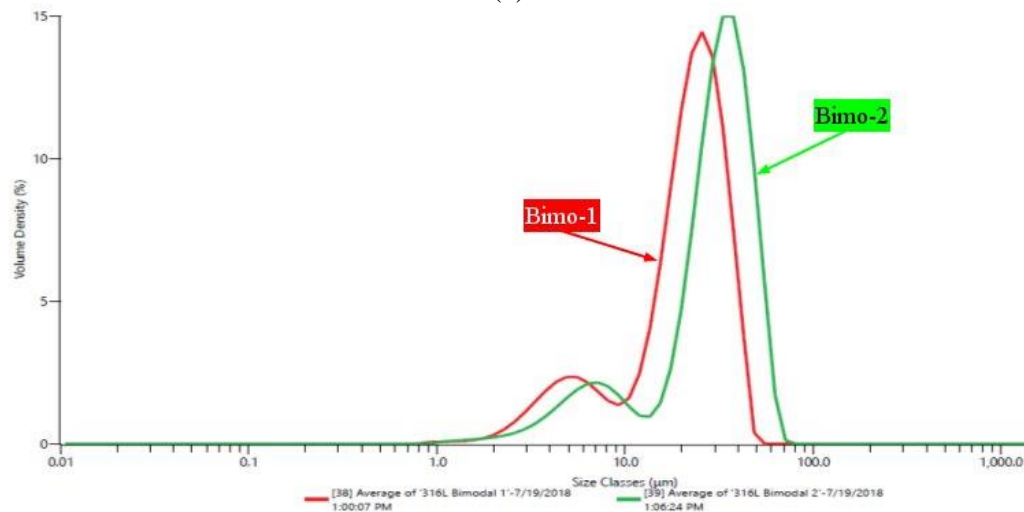
Figure 34. Particle size distribution histogram of fine particles (USRN-A) measured by Malvern particle size analyzer

It should be noted that while both large particle types were gas-atomized with a spherical particle shape, USRN-A possessed a combination of semi-spherical and irregular particles, as shown in the SEM micrographs of each powder type presented formerly Figures 28 and 29.

Similarly, Figure 35a shows the difference in particle size distribution between the as-supplied coarse powder (OM) and the powder that has been sorted for a narrow size distribution (OM-2).



(a)



(b)

Figure 35. Histogram of particle size distribution for (a) coarse 316L powders with normal PSD (OM) and narrow PSD (OM-2), and (b) bimodal mixtures containing coarse powder with normal PSD (Bimo-1) and narrow PSD (Bimo-2)

Both powders had a similar primary particle size ($\sim 35\mu\text{m}$ for OM, $\sim 38\mu\text{m}$ for OM-2), and both contain residual fine powder. The histogram in Figure 35b shows the PSD for the first two bimodal batches: Bimo-1 and Bimo-2.

The histogram shown in Figure 35b demonstrates two distinct modes in each bimodal mixture batch representing the primary value of the fine ($5\text{--}7\mu\text{m}$) and coarse powder ($25\text{--}40\mu\text{m}$) respectively. Note that the peak of the small particle size varies between Bimo-1 ($5\mu\text{m}$) and Bimo-2 ($7\mu\text{m}$). Since the coarse powder used in the Bimo-2 mixture has been sorted to eliminate the smallest of intermediate particle sizes, the volume % of intermediate sizes between the two primary sizes is lower, making the peaks of the two primary sizes more pronounced. The histogram for Bimo-1, however, shows a more gradual slope in that region, due to the overlap of the largest particles in the fine powder, and the smallest particles in the coarse powder.

4.1.2. Powder Density and Flow Properties

Figure 36 presents a comparison of tap and apparent density values for each of the single mode and bimodal powders used in producing SLMed samples.

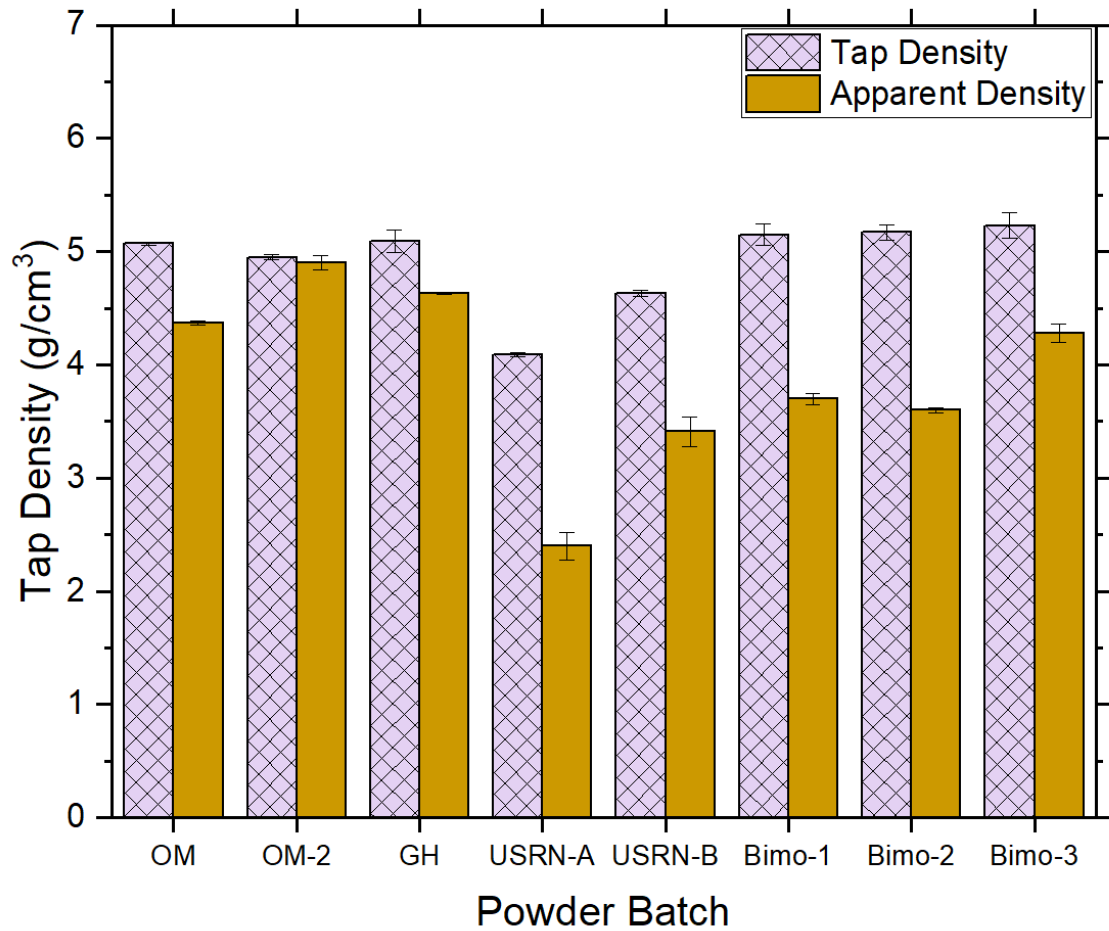


Figure 36. Powder bed densities for each powder type

The tap density of Bimo-2, while slightly higher, was nearly the same as the tap density of Bimo-1, as shown in Figure 36. Professor Randall German [8] observed that particles in a bimodal powder batch with diameters between that of the large and small primary sizes can prevent complete packing by forcing larger particles apart instead of filling the gaps between them. Therefore, Bimo-2 was expected to have a notably higher tap density than Bimo-1, due to the presence of intermediate particle sizes in Bimo-1. However, the apparent density of Bimo-1 was higher than that of Bimo-2. This was likely

due to the higher concentration of poor-flowing small particles in Bimo-2 (24.4% smalls by weight). This is illustrated in the comparison between Hausner ratios as illustrated in Figure 37.

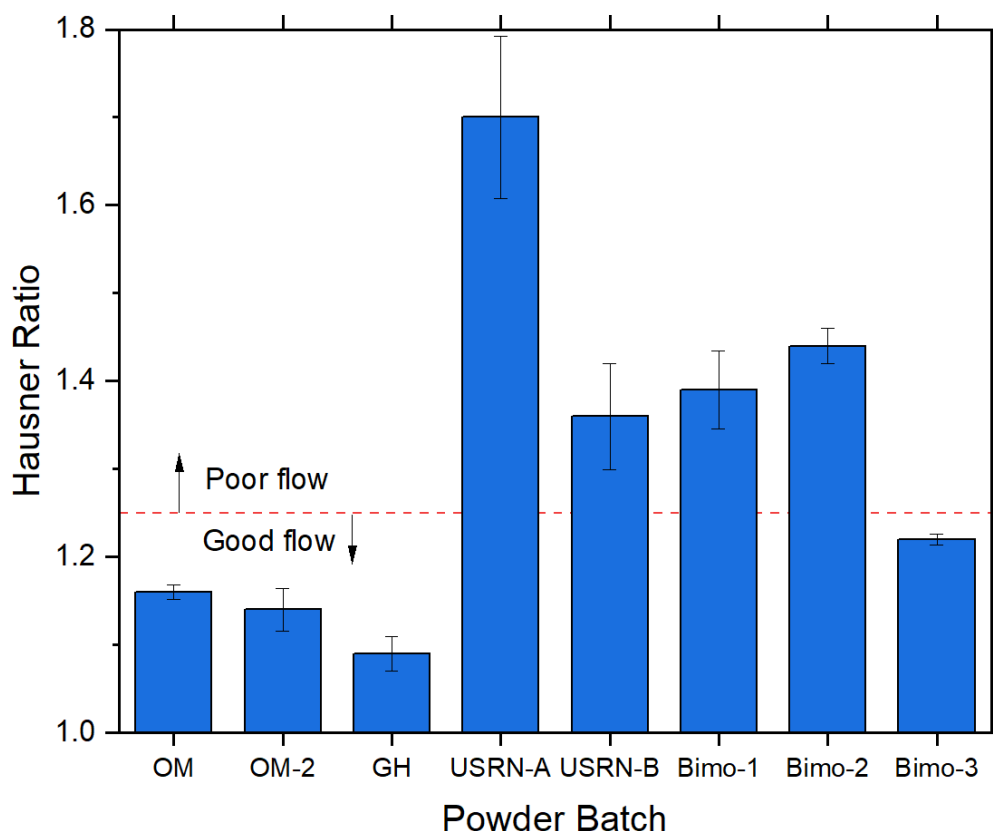


Figure 37. Hausner ratio measured for each powder type. The red dotted line shows upper limit of “good flow” at $H < 1.25$

Furthermore, the maximum packing density (tap density) of all three bimodal powders was slightly higher than that of the single mode powders. Small powders and bimodal powders containing the smalls had a significantly lower apparent density than the larger single mode powders.

The measured Hausner ratios of the fine powder (USRN-A and USRN-B) and the first two bimodal powders was much higher than the threshold for good flow ($H < 1.25$) and thus were considered to have poor flowability. The Hausner ratio was highest for the first batch of fine powder (USRN-A). The presence of non-spherical and agglomerated particles in USRN-A (shown in Figure 28 in Chapter 3) was likely the reason for this poor flowability [8]. Although all three bimodal batches had poor flowability compared to single mode large powders, Bimo-3 showed better flowability than Bimo-1 and Bimo-2. Since Bimo-1 and Bimo-2 contain the poor-flowing small powder, USRN-B, this was an anticipated result. Unlike Bimo-1 and Bimo-2, the Hausner ratio for Bimo-3 was sufficiently low to classify the powder as having “good flow” according to the standard [19].

4.1.3. Spread Density - Results of Experimental Testing Method

The tap density and apparent density of the powder used in testing the spread density measurement method is given in Table 10, along with the density results of four different spread methods using this feedstock.

Table 10 - Spread density of <149 μ m water-atomized 304 stainless steel with 0.41 mm layers

	Density (g/cm ³)
Single sheet	2.42 ± 0.045
Three sheets, single spread	2.91 ± 0.209
2 sheets, spread after each sheet	3.28 ± 0.251
layers, spread after each sheet	3.68 ± 0.155
Apparent Density	3.10
Tap Density	3.87

Wall effects were clearly dominant in a single layer sample, as evidenced by the increase in density per layer from one to three layers. These results were closer to the measured apparent density of $\sim 3.1 \text{ g/cm}^3$ than the tap density value. Three-layer samples appear to be denser when spread one layer at a time. However, excess powder trapped between layers may contribute to additional mass and thickness, distorting the results. In this case, a better spreading blade could provide a fully clear top surface of each layer and therefore could lead to more accurate results.

The layer thickness of actual SLM components in this study was closer to 50 or 60 μm , so using a millimeter-thick layer is not necessarily indicative of the accuracy of this process. The 114 μm stainless steel sheets used in the second set of spreading tests provided a scale that was more comparable to SLM. While the powder used in these tests is larger than those used for SLM, the larger spreading test powders were proportional to the sheet thickness in the same way SLM feedstock powders were proportional to the layer thickness. The spread powder density found with multiple powder size is given in Table 11 along with tap and apparent density for comparison.

Table 11 - Spread density of gas-atomized 316L stainless steel with 0.114 mm sheets

Particle Size (D ₅₀):	Density (g/cm ³)		
	49μm	66μm	89μm
Single sheet	3.27±0.599	4.33 ± 0.353	4.54 ± 0.726
Three sheets, single spread	4.60±0.456	4.36 ± 0.074	4.30 ± 0.027
2 sheets, spread after each sheet	4.64±0.139	4.90 ± 0.259	6.50 ± 0.245
3 layers, spread after each sheet	5.36 ± 0.387	5.83 ± 0.364	6.68 ± 0.421
Apparent Density	4.52	4.57	4.63
Tap Density	5.04	5.05	4.92

As shown in Table 11, the spread density taken from the test method is similar to the measured apparent density. Mean values for spread density were calculated to be higher than the tap density. Since this is not possible, the higher masses from these tests are likely due to powder spreading out between the layers. This excess mass is more for larger powder, where particles trapped between sheets have a greater effect on the height of the powder chamber.

To be useful as a tool for powder property determination, this prototype would require further additions and modifications. A standard method of seating, aligning and clamping the stacked pieces together should be developed to ensure higher consistency in the results. Other shapes for the test volume besides a round cylinder may contribute to more uniform spreading. Control over the spreading velocity and uniformity is also needed for better repeatability. In future work, validation of the significance of density measured using this method should be done by comparing the spread density to the density of printed parts. Comparison of spread sample density to density measured using the printed box

method shown in Figure 5 may also be useful in determining whether the test method is a suitable simulation for spreading in the SLM process.

4.1.4. Morphology

As shown in the Chapter 3, Figure 28 and Figure 29, USRN-A, the first fine powder selected for mixing, had a morphology that was far from spherical. The extremely poor flowability of this powder and subsequently the bimodal powders was largely attributed to this inconsistency in shape as well as size, due to agglomerations formed. The USRN-B powder used later in the Bimo-3 mixture was gas atomized, and particles had a consistently spherical composition as shown in Figure 38.

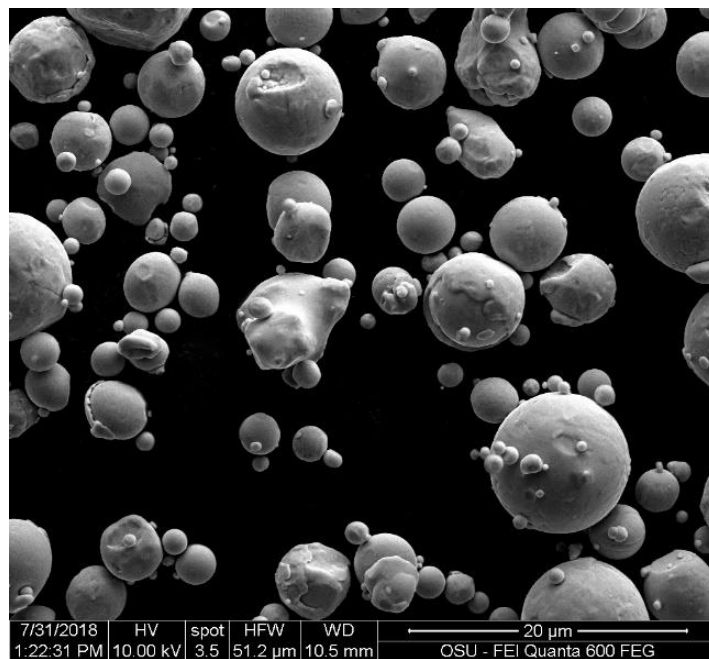


Figure 38. SEM micrograph of USRN-B. Note satellite powders forming on the outside, perhaps leading to poor flowability. Powders were relatively spherical.

However, even USRN-B particles were not perfectly spherical, and particles in this powder set were shown to have satellite micro-particles fused to them leading to poor flowability. The flowability of both powders and tendency to agglomerate was likely due to a higher oxygen content and larger surface-area-to-size ratio which resulted in adsorption of moisture in ambient air and thus agglomeration and interparticle forces.

4.2. Density of Bulk Samples

In the following section, the results of Archimedes density measurement for SLM samples produced at each parameter, from each powder type, are presented. This includes the density of arc melted samples produced from each batch of powder, used to determine the material density of the specific composition of each batch. In this section is shown that powders with the lowest Hausner ratios, and thus best flow quality, generally resulted in the highest relative density. Furthermore, it was shown that increasing VED does not indefinitely result in higher sample density, as high energy density can result in vaporization of the metal powder rather than conductive melting.

4.2.1. Nominal Density of Each Powder Type

The measured density of the arc-melted samples corresponding to each powder type used in printing are shown in Figure 39. While these material densities fall within a similar range, between 7.92 g/cm³ and 7.96 g/cm³, they appeared to be just below than the ASTM standard density value for 316L which is 8.0 g/cm³ [14]. The nominal densities suggest that both of the fine powder types (USRN-A and USRN-B) had a higher density than the three

coarse powders. Therefore, the bimodally distributed powders had higher densities than the large powder in single modes. The powder mixture that yielded the highest nominal density sample was (Bimo-2) with the largest quantity of fine powder.

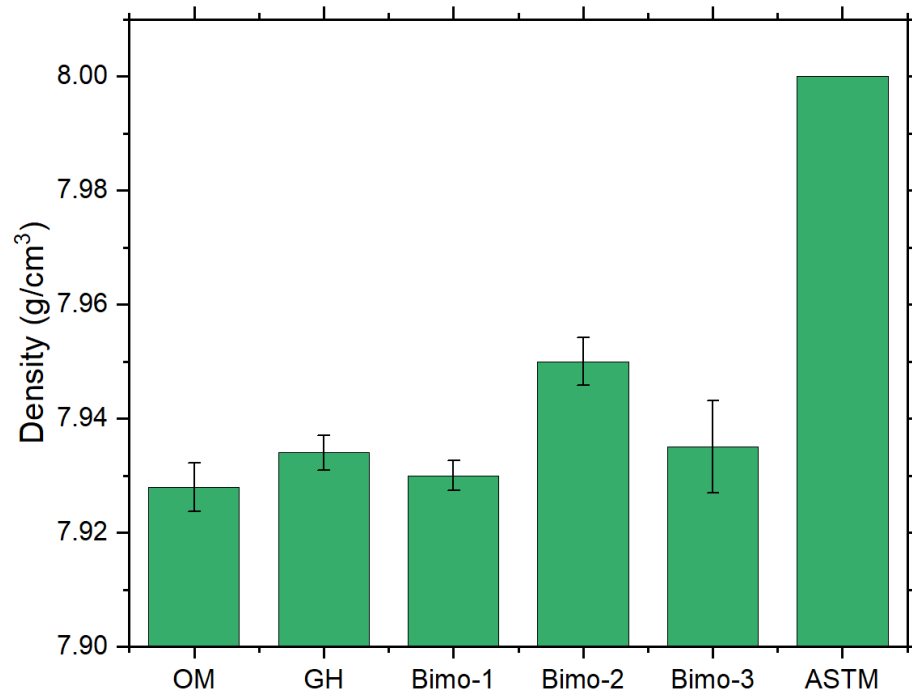


Figure 39. Measured nominal density of each powder type compared to standard value from literature [14]

4.2.2. Role of Volumetric Energy Density on SLMed Density

The following section presents the relative densities of SLMed samples produced at different VED levels using five different powder feedstocks. The densities were measured using the Archimedes method (Equation 20) and were compared to the previously mentioned nominal densities to determine percentage relative density for each SLMed sample.

In the first stage of density experiments, the single mode powder “OM” was SLMed at the same parameters as bimodal powders Bimo-1 (normally distributed large) and Bimo-2 (narrowly distributed large). The relative density of SLMed samples from each feedstock was plotted as a function of VED as shown in Figure 40.

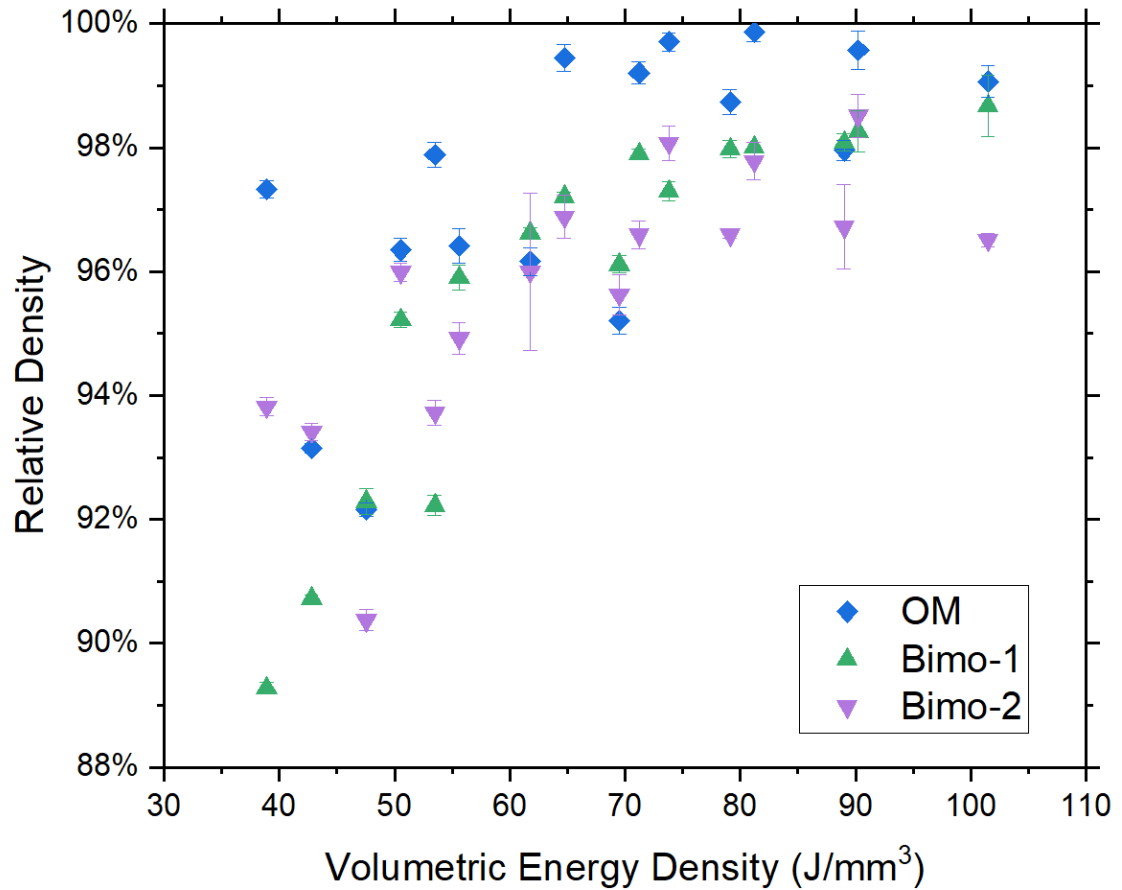


Figure 40. Relative density as a function of volumetric energy density for SLMed samples produced with single mode powder (OM), normally-distributed bimodal powder (Bimo-1), and bimodal powder with a narrow size distribution of large powder (Bimo-2).

Density was higher in SLMed samples using single mode powder feedstock than either of the bimodal PSD feedstocks. While the bimodal powders showed higher maximum packing density (tap density), the diminished flowability of the bimodal mixtures (as evidenced by their high hausner ratios) had a significant impact on the density of SLMed samples. One reason for poor flowability in mixtures containing small particles was that particles with higher surface area to mass ratios tended to absorb more moisture from the air.

The second batch of single mode and bimodal powder showed slightly higher relative densities than the first batch overall, although the top density was found in OM powder above. The USRN-B powder, used in the bimodal distribution Bimo-3 for this powder set, showed better flow characteristics and higher packing density than the previous two bimodals, as shown in Figure 37, which likely helped facilitate higher density in SLMed parts. For both the single mode and bimodal, the maximum density was found to be around 70 J/mm^3 . With relatively high laser power ($\sim 203\text{W}$) and high scan speeds (1000-1200 mm/s) at these VEDs relative densities were measured to be over 99.9%. Density began to decrease when VED was increased beyond 90 J/mm^3 . However, as discussed in the next section, similar VED values yielded different densities when performed at different power levels. These VED values for maximum density contradict the widely-regarded assertion by Cherry *et al.* that maximum density is achieved at an optimum VED of 125 J/mm^3 [33]. More recent studies [12-13, 43] have found that Cherry's theory is an over-simplification of the relationship between VED and relative component

density which fails to consider limitations of VED as a single predictor for powder consolidation behavior [13].

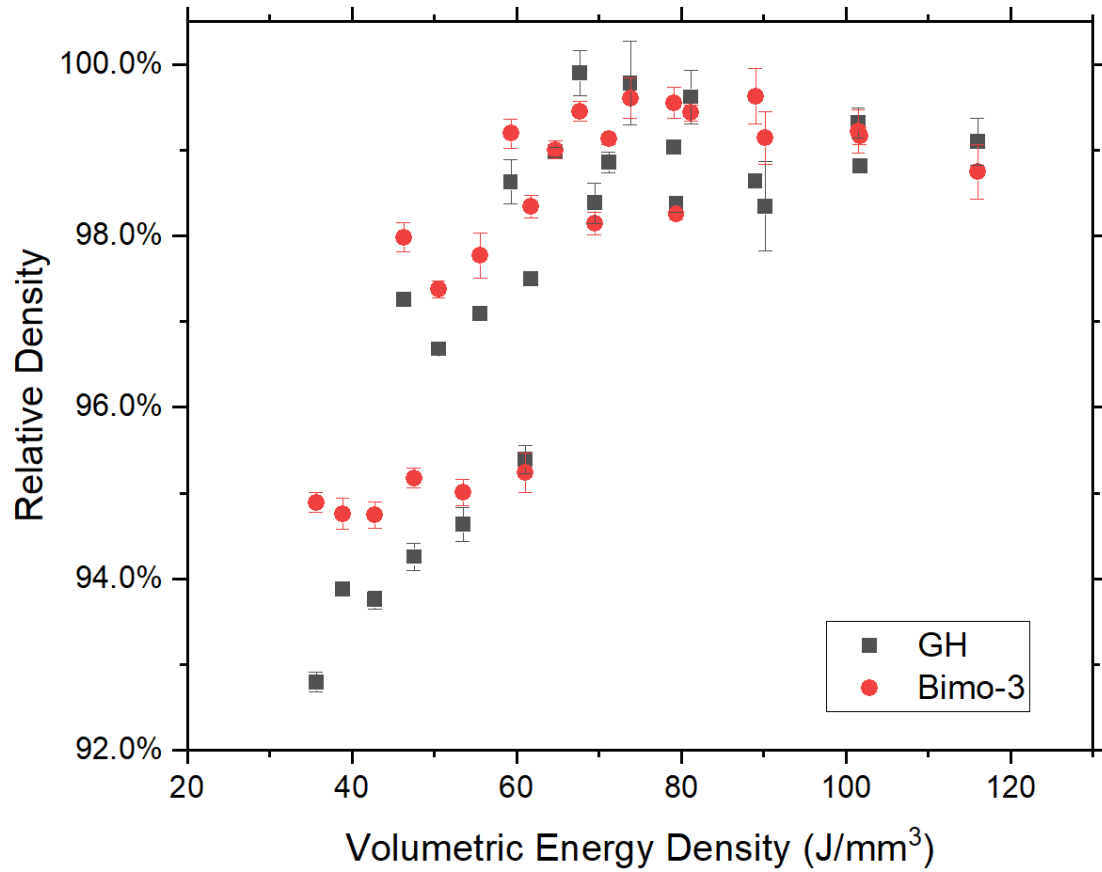


Figure 41. Relative density of 316L SLMed samples as a function of volumetric energy density for single mode feedstock powder (GH) and bimodal feedstock powder (Bimo-3)

4.2.3. Density Dependence on Laser Power and Limitations of Volumetric Energy Density

While the scatter plots in Figure 40 and Figure 41 and show an approximate trend towards increasing density with increasing VED, the relationship is not consistent enough

to achieve a curve fit that accurately describes this relationship with a mathematical equation. As implied by Bertoli *et al.* [13], using VED as a single parameter to predict density of an SLMed component ignores much metallurgical phenomena and process physics during the SLM process. However, a closer investigation of these same relative density vs VED values separated by each level of power input reveals a trend between density and VED when power is held constant. Figure 42 displays the same values as Figure 41, plotted to show each power level, with VED varying for different scan speeds.

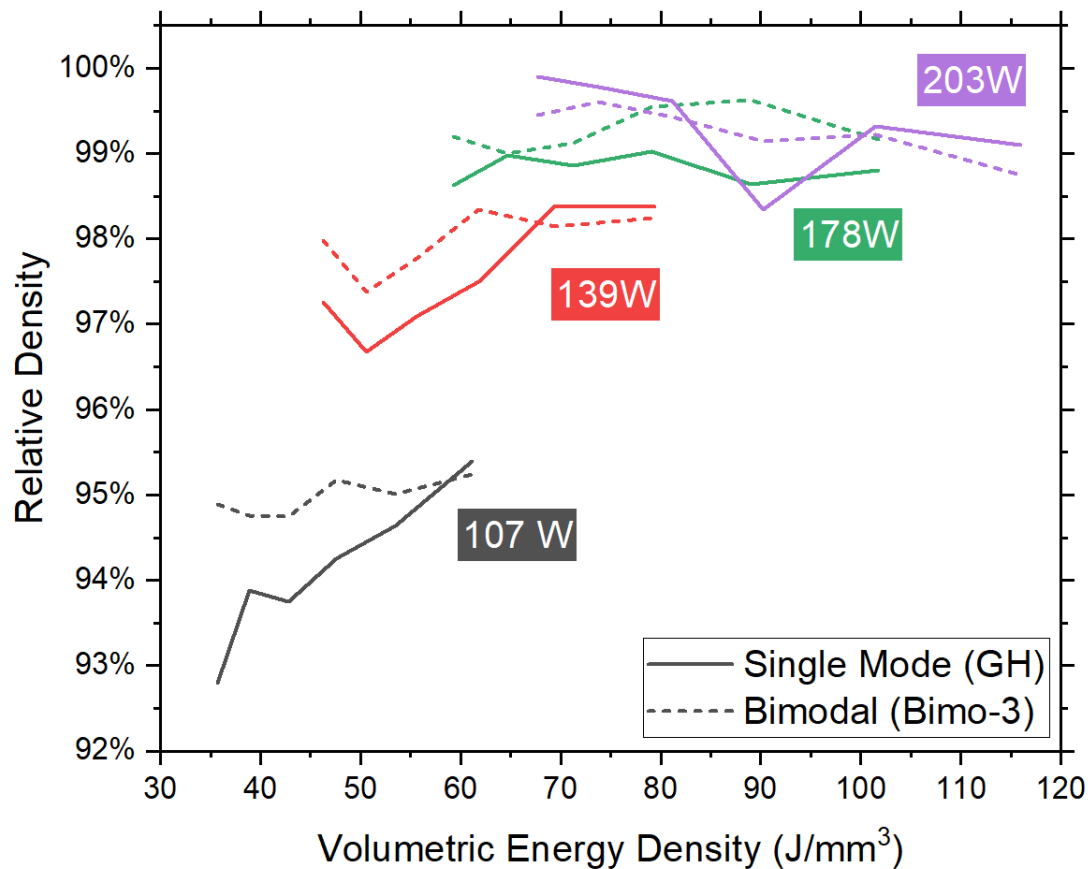


Figure 42. Relative density values as a function of volumetric energy density for different power: 107, 139, 178 and 203 W. For each power level, scan speed ranges from 700-1200 mm/s

Figure 42 shows that for GH single mode powder, density values increased with increasing VED at low power levels ($P < 178\text{W}$, $\text{VED} = 60\text{-}100\text{J/mm}^3$), but at a certain power threshold ($\sim 178\text{W}$), density remains relatively constant for increasing VED. At higher power levels ($\sim 200\text{W}$) for $\text{VED} > 70\text{ J/mm}^3$, density begins to decrease with increasing VED. This is consistent with well-documented laser-material interactions which demonstrate keyhole melting and vaporization beyond a particular limit of VED [13, 57]. Interestingly, however, the density in Figure 42 of samples produced from bimodal powder (Bimo-3) behaved differently with increasing VED than the single mode samples do. For bimodal samples, the relative density is nearly constant for increasing values of VED (i.e. decreasing scan speed) at a single power level. The limit at which density began to decrease with increasing VED occurs at a relative density of $\sim 99.6\%$ as opposed to the 99.9% density maximum of single mode powder. This implies that vaporization may be occurring at lower VEDs for bimodal powder than for single mode powder. Since the fine powder in each bimodal mixture is much smaller than the large powder, it is possible that VEDs high enough to achieve conduction melting for the larger particles may be well beyond the vaporization point of the small powders.

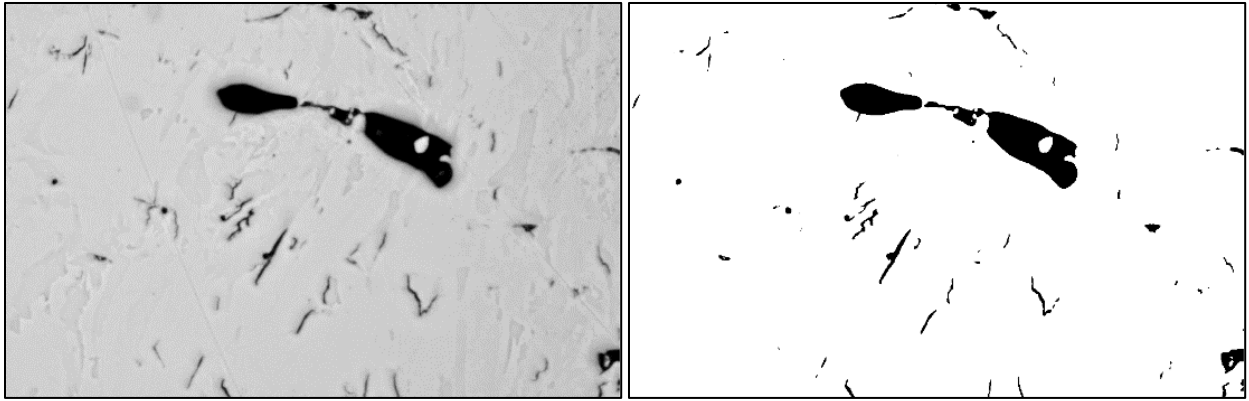
The trends displayed in Figure 42 implied that ultra-high energy densities were not necessarily needed for optimum consolidation. Using high power led to a higher demand on energy resources. However, higher scan speeds can mean faster build efficiency than low scan speed. The combined effect of using high power and high scan speed to achieve a desired VED was found to be most effective on densification.

4.3. Microstructural Characterization and Analysis

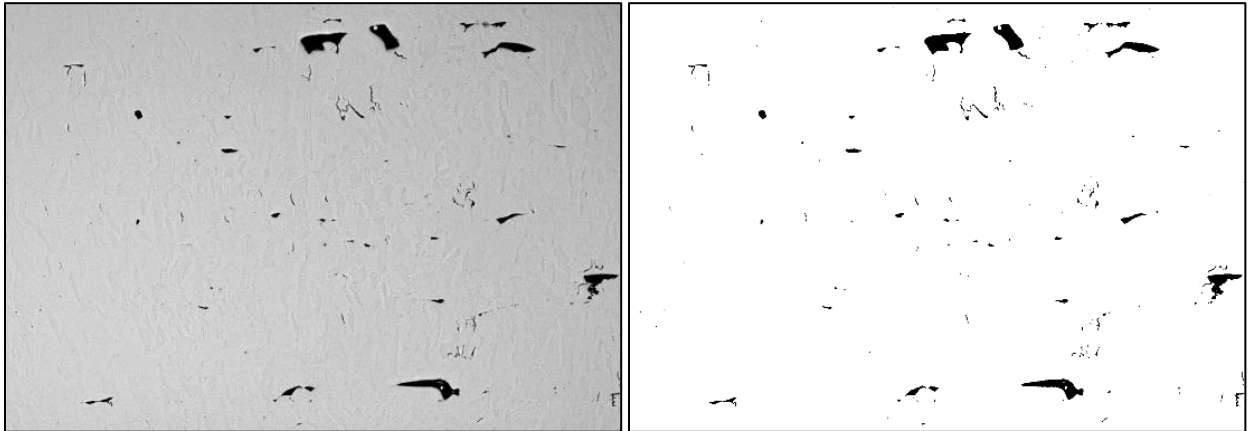
In this section, the microstructural characteristics of SLMed samples produced from single mode powder were compared to those of samples produced from bimodal powder, across several VED values. First, porosity and melt pool geometry were calculated by optical microscopy. Then, using scanning electron microscopy (SEM), sub-grain cellular size was measured and compared to existing models for the relationship between grain size and cooling rate. This cooling rate was applied to a model from literature for predicting grain size [12]. This calculated grain size was then compared to measured grain width predicted using the Hall-Petch equation for measured hardness values shown later in this chapter. Energy dispersive x-ray spectroscopy (EDS) was performed on one single mode (GH) and one bimodal (Bimo-3) sample to investigate any significant changes in chemical composition after melting.

4.3.1. Porosity Analysis

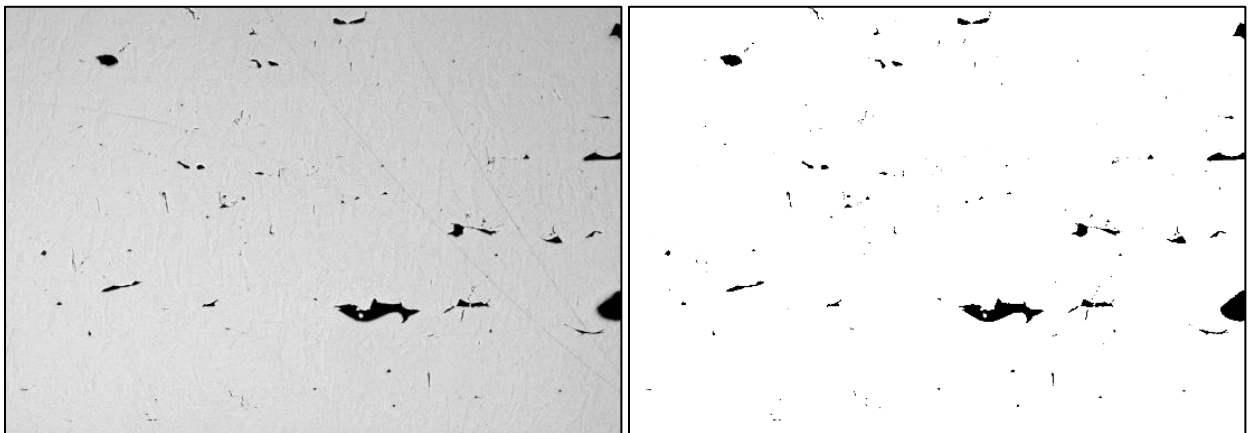
The cross section of as polished SLMed samples parallel to the build direction was observed by optical microscopy to determine the area% porosity for samples produced at several VEDs. The parallel cross-section with respect to build direction of several parts made from GH and Bimo-3 powder, and SLMed at power level of 203W was observed at magnification of 50x. Image J software was used to analyze the optical micrographs and quantification of porosity. The optical micrographs and corresponding Image J binary image for each set of parameters in single mode and bimodal powder are presented in Figure 43 and Figure 44, respectively.



(a) VED = 116.0 J/mm³, v=700 mm/s



(b) VED= 101.5 J/mm³, v=800 mm/s



(c) VED=90.2 J/mm³, v=900 mm/s



Figure 43. Optical micrographs and their corresponding Image J obtained from parallel cross-sections of GH single mode powder SLMed at 203W and at VED of (a) 90.2, (b) 101.5 and (c) 116.0 J/mm³

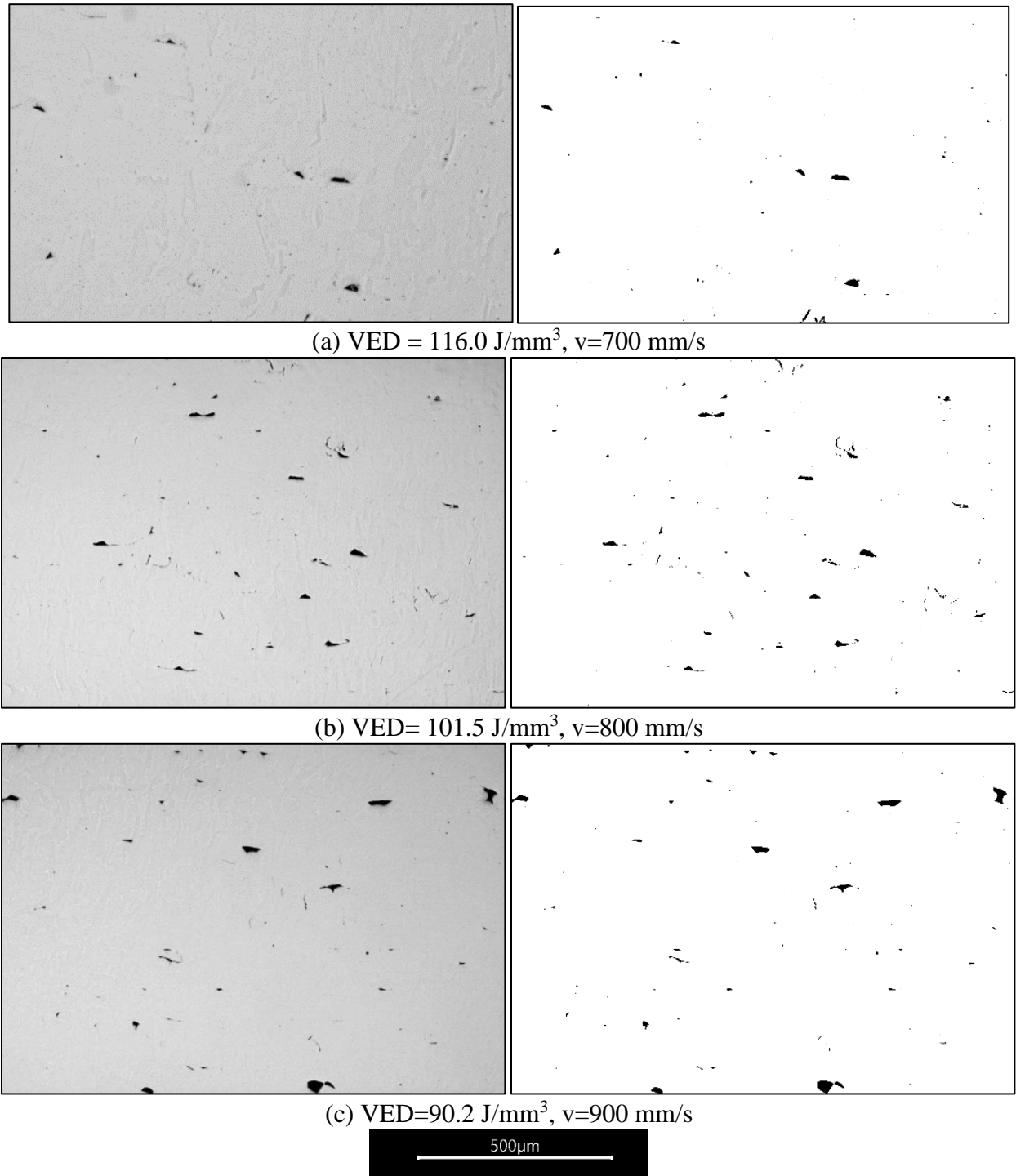


Figure 44. Optical micrographs and their corresponding Image J obtained from parallel cross-sections of bimodal size distribution powder Bimo-3 SLMed at 203W and at VED of (a) 90.2, (b) 101.5 and (c) 116.0 J/mm³

The area percent porosity of each of these sections was averaged to give an approximate % porosity for samples produced from each powder type as presented in Table 12.

Table 12 – Density values measured from area percent porosity based on analysis of optical micrographs of samples cut parallel to build direction and density values measured from Archimedes method for parts made from single mode GH powder and bimodal power Bimo-3 (parts were SLMed at VED of 90.2, 101.5 and 116 J/mm³)

VED		GH			Bimo-3	
J/mm ³	Area Density	Archimedes Relative Density	difference	Area Density	Archimedes Relative Density	difference
116.0	98.10%	99.1%	-1.00%	99.80%	98.7%	1.06%
101.5	98.83%	99.3%	-0.48%	99.42%	99.2%	0.20%
90.2	98.71%	98.3%	0.37%	99.55%	99.1%	0.41%

Since porosity was found to be most abundant between layers, only the parallel cross-section was used. In theory, this %porosity should be approximately equal to 100 minus the relative density measured for each sample. Area% porosity can provide an even better representation of the relative density of a sample than Archimedes method, due to the potential for unmelted powder to become trapped within in the voids within the material.

While a single cross-section may not consistently provide an accurate view of the overall porosity of the sample, measured porosity values aligned closely with measured densities in this case, as shown in Table 12. The largest disparity was 1.06% density.

4.3.2. Melt Pool Characterization

The height of the melt pool refers to the distance between the deepest level of penetration by a single melt track, and the deepest point of the next subsequent layer. The average melt pool height was determined by measuring the distance between the bottom edge of one melt pool to the bottom edge of a melt pool four layers above and dividing that distance by four. This was done because the shift angle of the scanning pattern in these builds was 45° , and the scanning direction was repeated every 4 layers. Figure 45 shows an example of layer identification and quadruple melt pool measurement for a parallel cross-section of Bimo-3 processed at 203W and 90 mm/s.

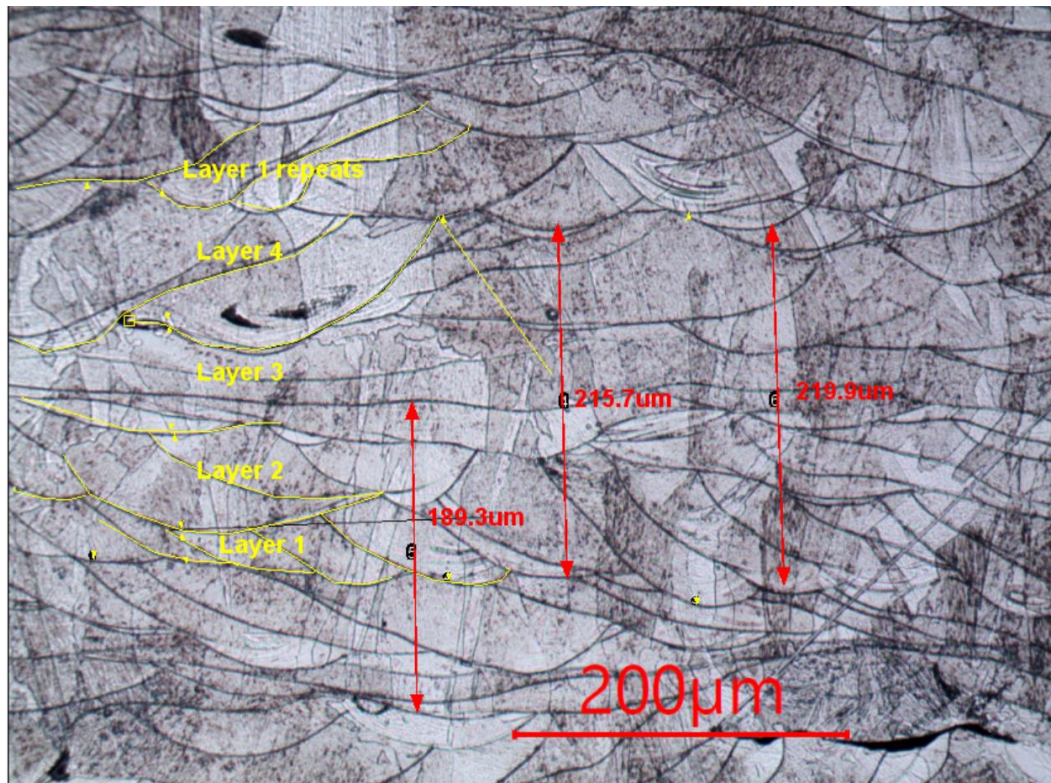
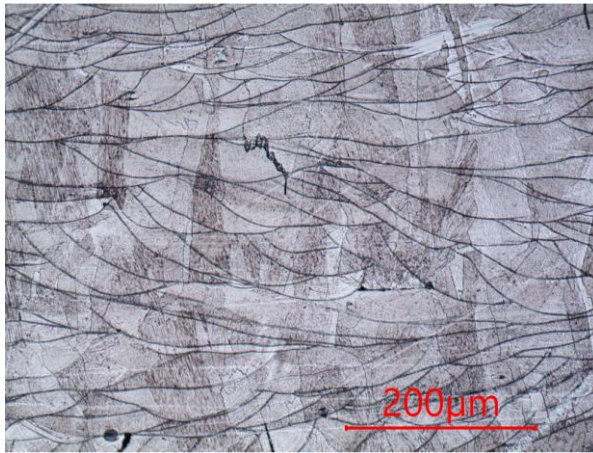


Figure 45. Optical micrograph showing melt pool measurement for Bimo-3 at $VED=90.2J/mm^3$

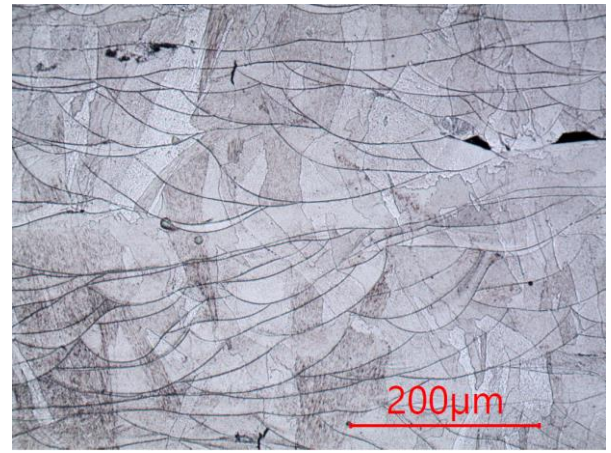
Table 13- Average thickness of melted layer for GH and Bimo-3 powder at VED of 90.2, 101.5 and 116 J/mm³

VED (J/mm ³)	Average thickness of melted layer (μm)	
	GH	Bimo-3
116.0	47.6 ± 2.83	49.7 ± 8.15
101.5	40.7 ± 6.01	49.2 ± 8.70
90.2	44.2 ± 11.04	57.3 ± 2.06

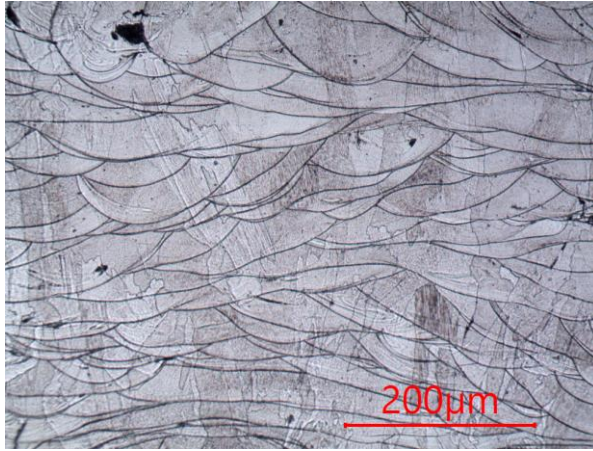
Figure 46 shows optical micrographs of samples from single mode and bimodal size distribution SLMed at VEDs of 90.2, 101.5, and 116 J/mm³. Optical micrographs were obtained from cross section parallel to build direction. The results in Table 13 show that average melt pool size does not vary significantly across this range of parameters. It is worth noting, however, that certain areas of porosity appear to result in inconsistent depth of melting, making the average layer height a rough approximation. Nonetheless, the layer height is shown to be, as anticipated, close to the machine-set layer height of 50μm, but slightly lower due to volume lost in consolidation of each powder layer. Interestingly, the layer height of the bimodal powders show higher values, suggesting that minimal consolidation from spread thickness occurs after melting.



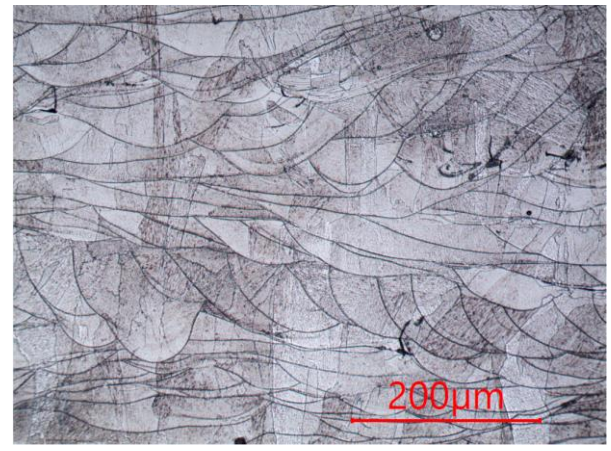
(a) Single mode (GH)
VED = 116.0 J/mm³, v=700 mm/s



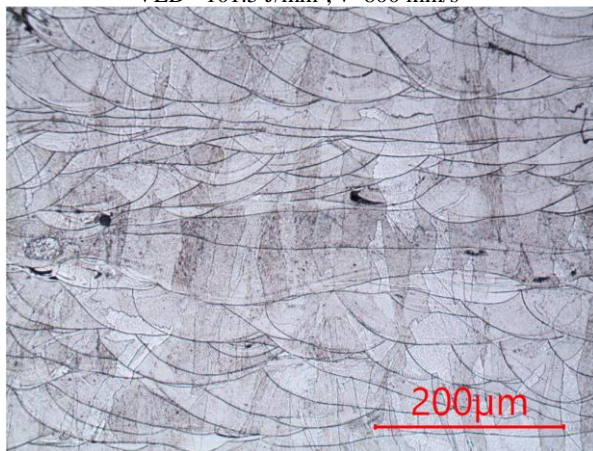
(b) Bimodal (Bimo-3)
VED = 116.0 J/mm³, v=700 mm/s



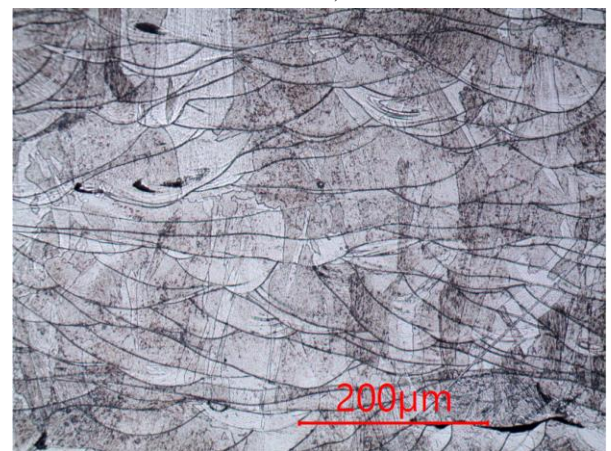
(c) Single mode (GH)
VED= 101.5 J/mm³, v=800 mm/s



(d) Bimodal (Bimo-3)
VED= 101.5 J/mm³, v=800 mm/s



(e) Single mode (GH)
VED=90.2 J/mm³, v=900 mm/s



(f) Bimodal (Bimo-3)
VED=90.2 J/mm³, v=900 mm/s

Figure 46. Optical micrographs showing melt pool in samples from single mode and bimodal size distribution powder SLMed at different VEDs

4.3.3. Intergranular Cell Growth

SEM was used to collect images from microstructure of samples made from single mode powder and bimodal powder size distribution and SLMed at VED of 81.2 and 116 J/mm³ as shown in Figure 47 and Figure 48, respectively.

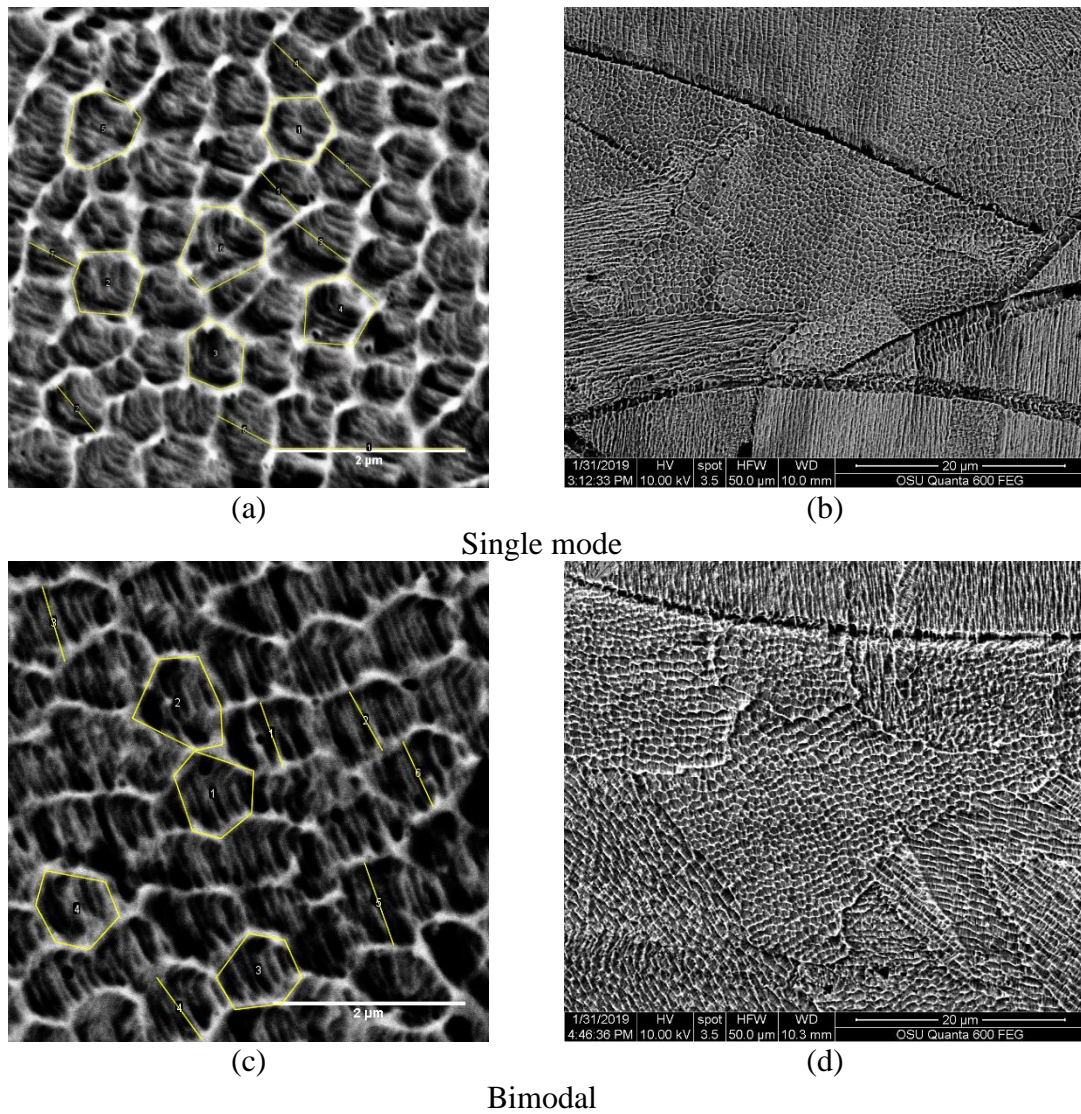


Figure 47. SEM micrographs obtained from (a)-(b) single mode powder and (c)-(d) bimodal SLMed at 80% power, 1000 mm/s, VED=81.2 J/mm³

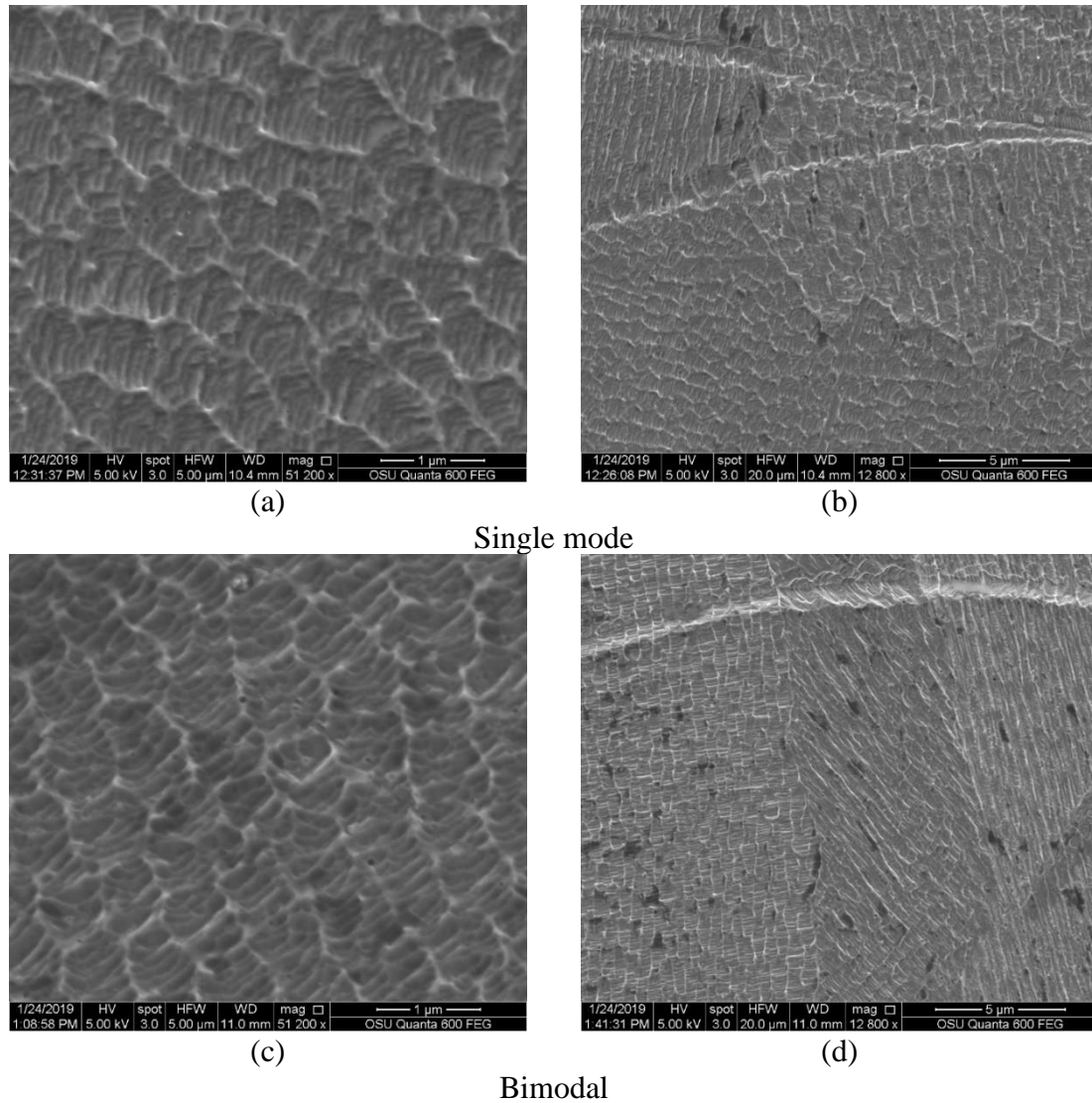


Figure 48. SEM micrograph obtained from single mode (a)-(b) and bimodal (c)-(d) powder size distribution SLMed at 80% power, 700 mm/s, $VED=700 \text{ J/mm}^3$

Corresponding cellular microstructure obtained from samples SLMed at VED of 81.2 and 116 J/mm^3 are also presented in Figure 47 and Figure 48.

After collecting micrographs, Image J analysis was used to measure cell area and cell width. Table 14 summarizes the cell area and cell width measured for SLMed samples. According to Figure 47, Figure 48 and Table 14, cells area and width were measured to be

larger at lower VED. Furthermore, cell area and width were larger for bimodal powder size distribution rather than in single mode powder samples. On the contrary, Wang *et al.* [42] reported lower energy density led to smaller intergranular cells, thus contributing to better mechanical properties. The reason for observing larger cells at lower VED in this study is not clear but could be likely due to cooling rate and scan speed difference in the samples. An investigation is needed to identify the formation and growth mechanisms of these cellular substructure.

Table 14- Measured cell area and cell width of cellular structure observed in single mode and bimodal powder size distribution SLMed at VED of 81.2 and 116 J/mm³

Unit		GH		Bimo-3	
VED	J/mm ³	116.0	81.2	116.0	81.2
Cell Area	μm ²	0.394 ± 0.0611	0.424 ± 0.0748	0.413 ± 0.0199	0.531 ± 0.0653
Cell width	μm	0.611 ± 0.0379	0.636 ± 0.0511	0.685 ± 0.0634	0.774 ± 0.0772

4.4. Phase Identification

As seen in previous studies [42–44], pure 316L stainless steel has a single phase of γ -austenite. The XRD patterns of powder feedstock and SLMed parts were analyzed to identify the phase(s) in powder and parts and investigate any phase transformation occurred during SLM process. As shown in the XRD patterns in Figure 49 and Figure 50 for each powder type, as well as the pattern for samples produced with each powder via SLM, most samples demonstrated patterns consistent with a pure austenite phase.

4.4.1. X-ray Diffraction

Figure 49 presents the XRD patterns for OM single mode powder, and SLMed samples produced from OM powder and Bimo-2 powder. Identified peaks of (111), (200) and (220) were attributed to presence of γ -austenite phase in OM single mode powder, and SLMed samples produced from OM powder and Bimo-2 powder.

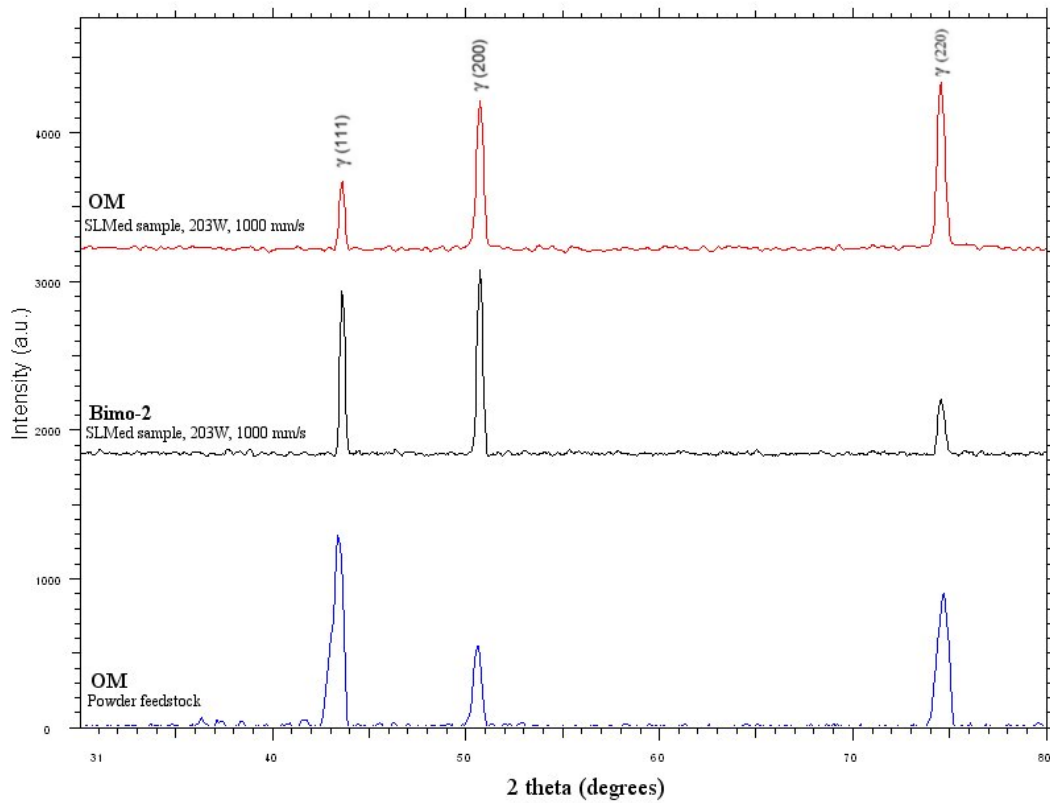


Figure 49. XRD pattern of OM single mode powder, and SLMed samples produced from OM powder and Bimo-2 powder

One difference in XRD patterns of OM powder feedstock, SLMed Bimo-2 and OM was the intensity of (111) and (200) peaks. The peak attributed to (111) showed higher intensity in OM powder and Bimo-2 SLMed samples. However, the peak attributed to

(200) showed lower intensity in OM powder and higher intensity in SLMed parts. This variation in peak intensity could reveal useful information about crystallographic orientation and developed texture in SLMed parts that will require additional characterization by electron back scattered diffraction (EBSD) and could be a potentially significant topic for future work.

Figure 50 presents the XRD patterns for large Hoeganaes powder, USRN-B small powder, and SLMed samples produced from bimodal powder size distribution (combination of USRN-B small powder and Hoeganaes large powder).

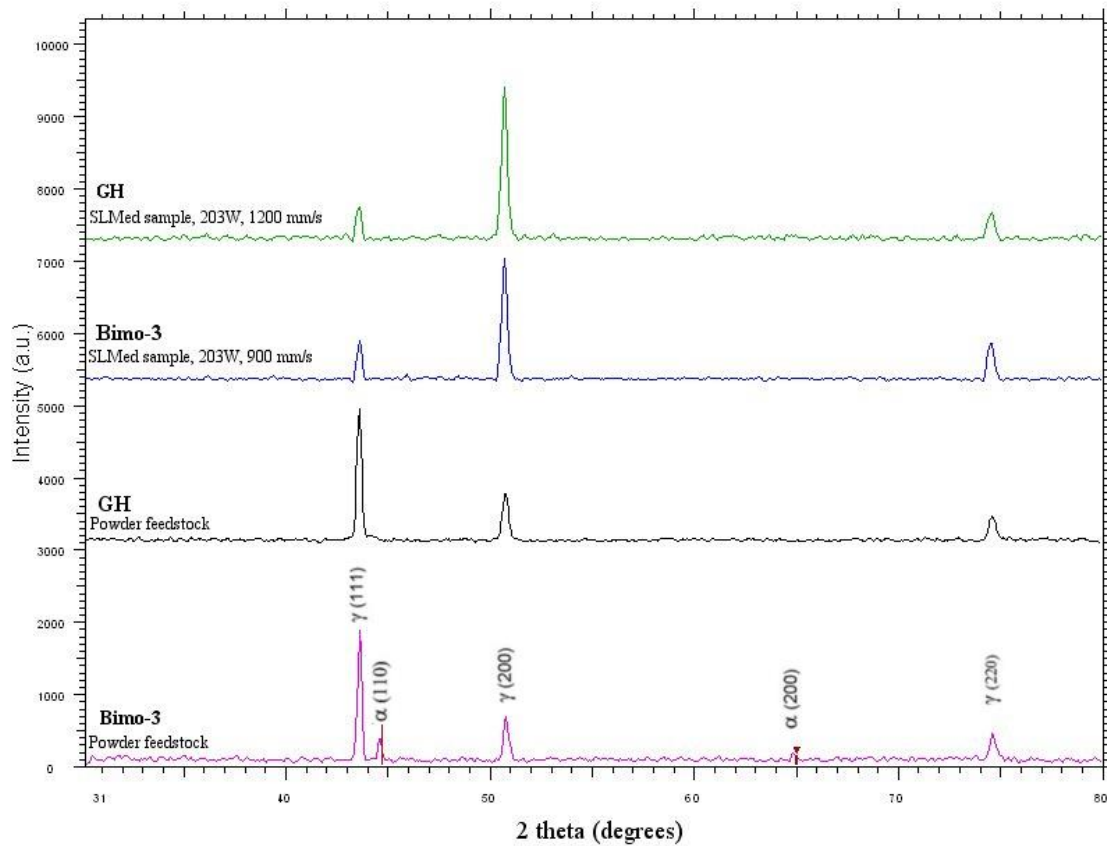


Figure 50. XRD pattern of Hoeganaes large powder, USRN-B small powder, and SLMed samples produced from bimodal powder size distribution (combination of USRN-B small powder and Hoeganaes large powder)

Identified peaks of (111), (200) and (220) were attributed to the presence of γ -austenite phase in Hoeganaes powder, and SLMed samples produced from bimodal powder size distribution with no additional phases observed. In USRN-B small powder, few peaks occurring at angles consistent with a ferrite phase were present. Similar evidence of some ferrite was seen in XRD scans of 316L SLM feedstock powder by Sun *et al.* and Kurzynowski *et al.* [35, 43]. However, in all cases, these peaks disappeared after SLM.

Similar to Figure 49, the peaks intensity varied between GH powder feedstock and SLMed parts. The former had (111) as the highest intensity peak, whereas (200) peaks had the highest intensity in the latter.

4.4.2. Chemical Analysis

Energy dispersive x-ray spectroscopy (EDS) was used to investigate the chemical composition of samples made from single mode and bimodal powder size distribution SLMed at $\text{VED} = 81.2 \text{ J/mm}^3$ (203W, 1000 mm/s). Figure 51 shows the SEM micrographs and corresponding EDS histogram from single mode (a-b) and bimodal powder (c-d) SLMed at 81.2 J/mm^3 .

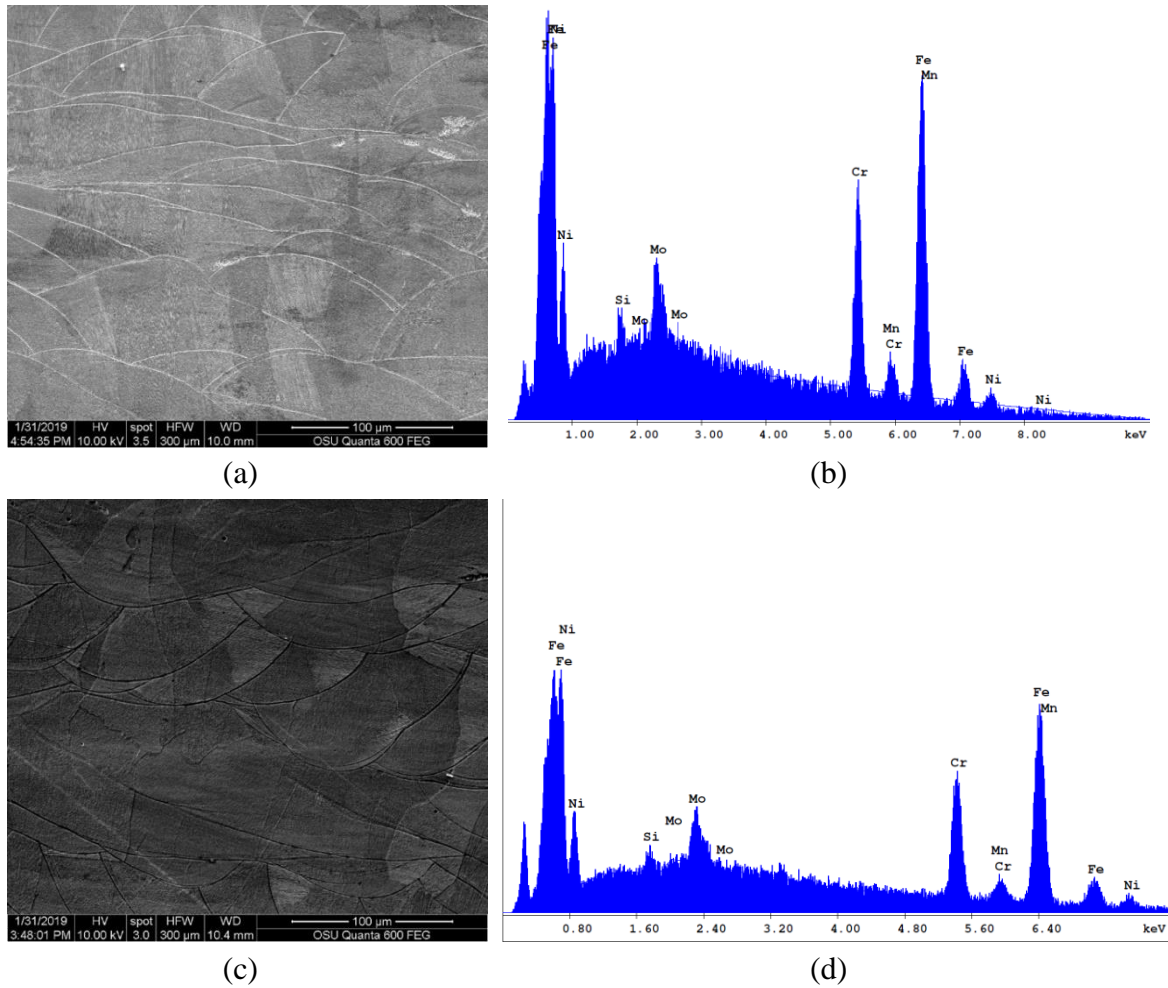


Figure 51. GH single mode powder SLMed at 80% power and 1000 mm/s: (a) SEM micrograph parallel to build direction, (b) corresponding EDS histogram, Bimo-3 Bimodal powder SLMed at 80% power and 1000 mm/s: (c) SEM micrograph parallel to build direction and (d) corresponding EDS histogram

Table 15 summarizes the chemical composition obtained from EDS histograms shown in Figure 51 b and d.

Table 15 Chemical composition (wt%) of single mode and bimodal powder size distribution SLMed at 80% power and 1000 mm/s, VED= 81.2 J/mm³ based EDS histogram shown in Fig. 14 b, d

Sample Type	Fe	Cr	Ni	Mo	Si	Mn
Single mode (GH)	44.85	35.9	11.54	5.88	0.87	0.97
Bimodal (Bimo-3)	43.73	36.14	10.40	5.26	0.69	3.79

EDS analysis for single mode and bimodal powder size distribution SLMed at the same VED of 81.2 J/mm³ (80% power and 1000 mm/s) VED was not significantly different. However, a higher percentage of Cr content was observed in the SLMed samples in comparison with powder. Further investigation is needed to identify the cause of this unusually high chromium content.

4.5. Hardness of SLMed 316L

Microhardness tests were conducted on the cut and polished surface of SLMed samples made from various powders (single mode and bimodal powder size distribution) at different VED values (66-116 J/mm³). Indentations were made in 10 locations around the cut and polished surface parallel to the build direction for each sample. The averages of these values were used to plot microhardness as a function of VED as shown in Figure 52a.

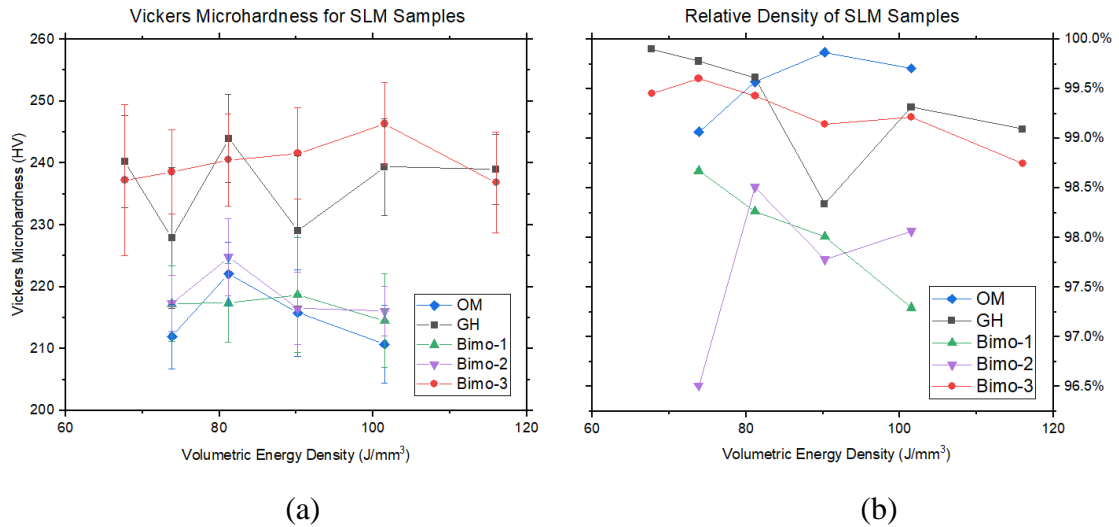


Figure 52. (a) Vickers microhardness of SLMed samples produced from different powders at various VEDs (66-116 J/mm³), (b) relative density of samples tested for hardness.

As shown in Figure 52b, the highest hardness values (243-246 HV) were associated with the powder that resulted in the highest density overall (GH and Bimo-3). The average microhardness values for single mode power (GH) and bimodal power (Bimo-3) approximately increased at higher VEDs. Bimodal powder SLMed samples showed higher hardness than single mode powder SLMed samples overall. For example, microhardness values of 246 ± 6.7 HV and 239 ± 7.8 HV were measured for bimodal powder (Bimo-3) and single mode (GH) powder, respectively, SLMed at VED of 101 J/mm³. These values are lower than results from prior work by Ma *et al.*[12] who reported hardness of ~ 261 at VED of 68 J/mm³, who notes that hardness tends to decrease with increasing surface energy density, but not necessarily with VED. However, hardness measured in this study tended to be higher than Tucho *et al.*'s [48] reported 179-213 HV at 50-125 J/mm³.

While hardness values measured in this study showed only a slight decrease with increasing VED (in powder batches OM, Bimo-1 and Bimo-2), and instead remain relatively constant for each powder batch within standard deviation of each other, studies over a wider range of VED show hardness decreasing with increasing VED [12, 42, 47]. This brings into consideration another purpose for optimizing SLM density at lower VED values than the 104 J/mm^3 reported by Cherry *et al.* [33] that if full density can be achieved at VEDs below 104 J/mm^3 , a finer grain structure can be maintained, resulting in higher hardness than the 225 HV as reported by Cherry *et al.* [33]. Kurzynowski *et al.* [43] reinforced this theory by demonstrating porosity of $< 0.2\%$ in samples SLMed at both 81 and 150 J/mm^3 . Between these two parameters, the as-built samples produced at 81 J/mm^3 had a measured hardness of $255 \pm 6 \text{ HV}$, whereas the 150 J/mm^3 samples with a similar porosity were found to be only $212 \pm 7 \text{ HV}$. Thus, if maximizing hardness is desirable, the lowest possible VED for achieving full density should be used.

4.5.1. Theoretical Cooling Rate

Using the relationship between cell spacing (width) and cooling rate described by Ma *et al.* [12] in Equation 15, the cooling rate of each of the four samples measured for cell size is given in Table 16 as follows:

Table 16 – Calculated cooling rate based on width of intergranular cells

	Unit	GH		Bimo-3	
VED	J/mm ³	116.0	81.2	116.0	81.2
Theoretical cooling rate	10 ⁶ (K/s)	2.30 ± 0.463	2.07 ± 0.539	1.67 ± 0.463	1.16 ± 0.317

As shown in Table 16, the calculated cooling rate was slightly higher for the higher value of VED. Cooling rates appeared to be lower for samples produced from the bimodal powder set. However due to the large standard deviation in these measurements, differences in calculated cooling rate of less than an order of magnitude are not considered significant.

4.5.2. Anticipated Grain Size

Based on the Hall-Petch relation (Equation 21) and constants experimentally determined by Ma *et al.* [12]), according to measured hardness values for samples produced at a range of VED values, from each powder type, the columnar grain width of SLM samples was calculated as follows:

Table 17 – Theoretical grain width in μm calculated from measured hardness

VED (J/mm ³)	OM	GH	Bimo-1	Bimo-2	Bimo-3
67.7		31.8			34.1
73.8	69.0	43.0	58.2	58.0	33.1
81.2	50.5	29.3	58.0	46.8	31.6
90.2	60.9	41.8	55.8	59.6	30.9
101.5	72.0	32.5	63.5	60.4	27.9
116.0		32.8			34.4

4.6. Post Processing of SLMed 316L (Annealing)

Annealed and etched GH sample SLMed at 73.8 J/mm^3 and Bimo-3 sample SLMed at 89.0 J/mm^3 are shown in Figure 53.

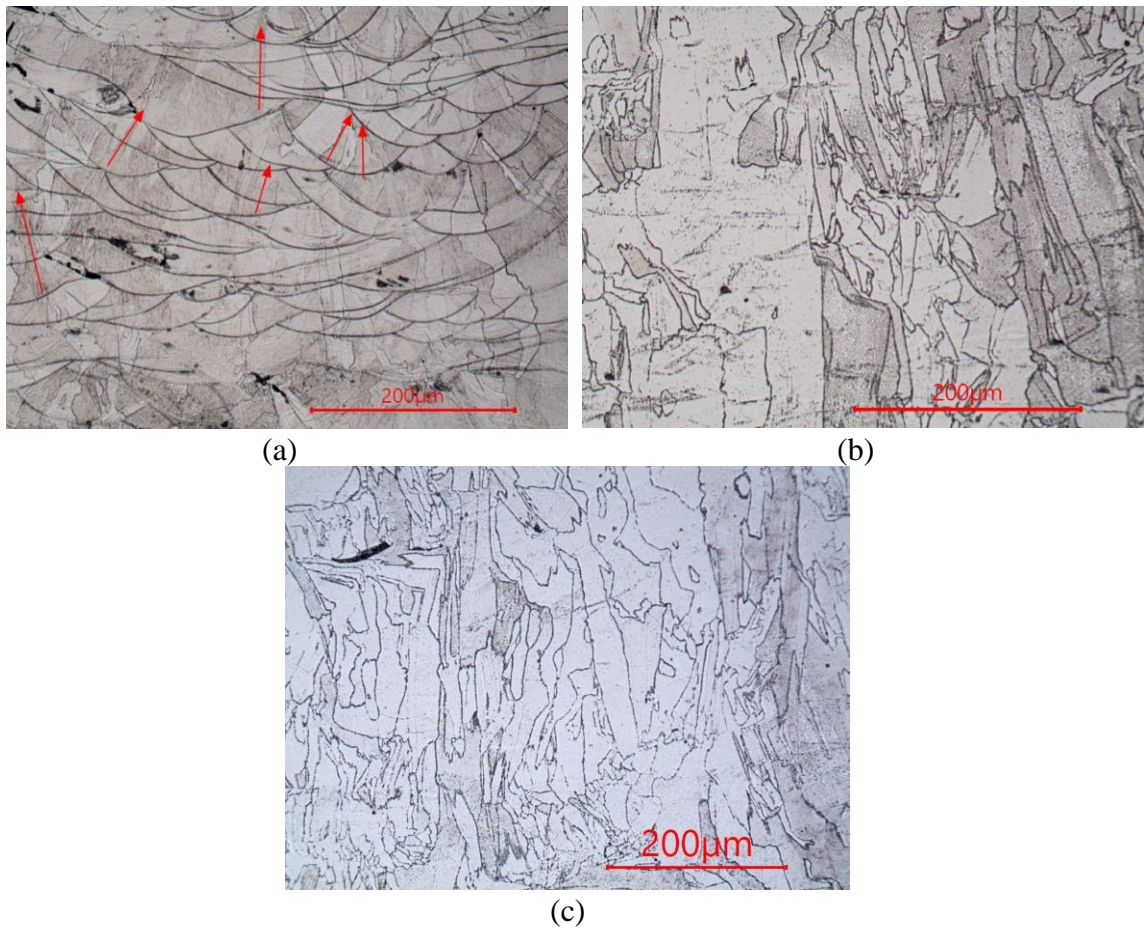


Figure 53. Optical micrograph obtained at 200x magnification: (a) Arrows show the direction of columnar grain growth for as-built single mode sample SLMed at 73.8 J/mm^3 (b) annealed single mode sample SLMed at 73.8 J/mm^3 with no melt pool boundaries, (c) annealed bimodal sample SLMed at 89.0 J/mm^3

Figure 53a shows the microstructure of SLMed samples with columnar grains and melt pool boundaries. Columnar grains in melted samples tended to grow preferentially

perpendicular to the melt pool boundaries as shown in Figure 53a, and these growth directions were primarily maintained in the annealed samples as shown in Figure 53b-c . However, melt pool boundaries disappeared after annealing.

Recrystallization and grain growth were observed in the micrograph shown in Figure 54 and Figure 55. Although the melt boundaries were no longer visible in the annealed samples, phantom melt lines could be traced by following the pattern of smaller, more equiaxed grains along trails like those traced by the dotted lines shown in Figure 55. High diffusivity paths along grain boundaries and melt pool boundaries could facilitate recrystallization and subsequently grains could grow lengthwise into columnar grains.



Figure 54. (a) Single mode GH sample SLMed at 73.8 J/mm^3 , annealed for two hours at 1020°C . Dotted lines trace regions of new grain growth along high-diffusivity paths that formed melt pool boundaries prior to annealing.

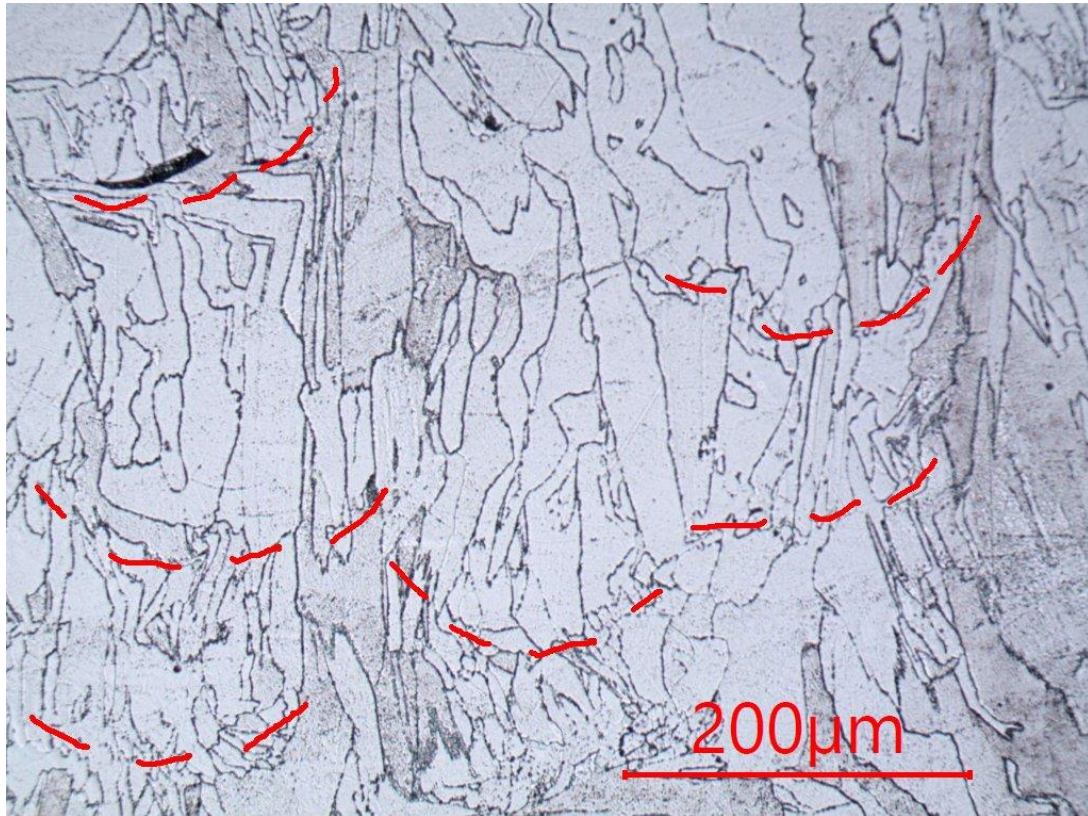


Figure 55. Bimodal Bimo-3 sample SLMed at 89.0 J/mm^3 , were annealed for two hours at 1020°C . Dotted lines trace regions of new grain growth along high-diffusivity paths that formed melt pool boundaries prior to annealing.

XRD patterns obtained from annealed GH sample, SLMed at 89.0 J/mm^3 and annealed Bimo-3 SLMed at 73.8 J/mm^3 revealed the presence of pure austenite as shown in Figure 56.

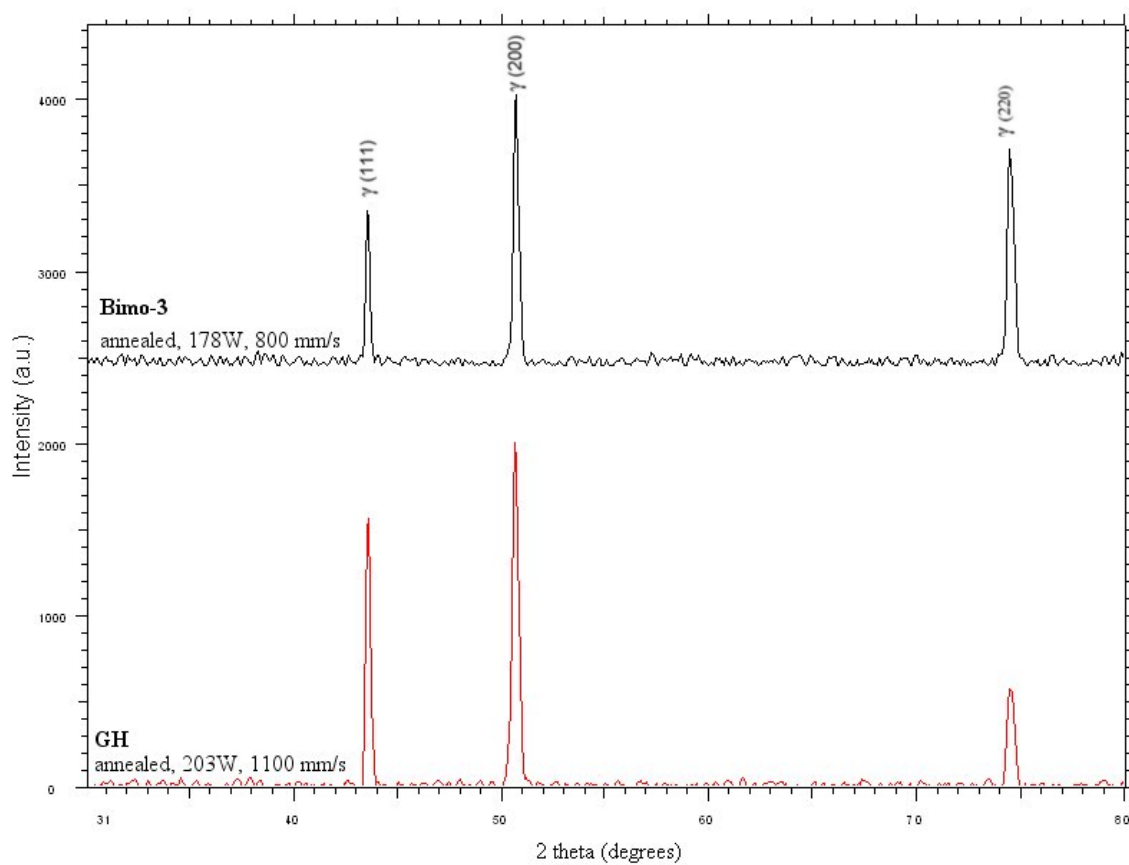


Figure 56. XRD patterns of annealed Bimo-3 and GH samples indicating a pure austenite phase

Chapter 5 – Conclusions and Future Work

5.1. Summary and Conclusions

The objective of this study was to evaluate the spreading properties and packing density of multiple 316L stainless steel powder bed feedstocks; with a single mode particle size distribution (typically used in SLM process) and bimodal particle size distribution (has not been explored in SLM process). In bimodal particle size distribution, three different powder mixtures were prepared and used as SLM feedstock. After comparing the packing density of these powder size distributions, solid samples were then manufactured via optimized SLM process. Density, microstructure, and mechanical properties of SLMed samples were characterized.

The goal of this Master's thesis was to enhance the final density of SLMed part by using bimodal powder bed size distribution and improving powder packing density. Experiments were designed and conducted to determine the role of particle size distribution of powder bed on density, microstructure and mechanical properties of the 316L stainless steel components additively manufactured via SLM process. In pursuit of this investigation, the following conclusions were reached:

1. Powder beds with bimodal size distributions could have higher maximum packing densities than normally distributed powders in a similar size range. The tap density of three bimodal powders compared to two single mode powders showed in this study that even when the secondary-sized particles lack sphericity and purity, the introduction of a secondary small particle size in the appropriate quantity and ratio could improve the

- packing density of the powder when particle arrangement is assisted by mechanical tapping. The tap densities of bimodal mixtures measured in this study were approximately 2% higher on average than their single mode precursor powders.
2. Bimodal powder size distribution showed poor flow characteristics compared to single mode powder. Low apparent density in small and bimodal powders resulted in higher Hausner ratios. Flowability was diminished when using bimodal powders in this size range. Use of spherical small particles in a bimodal powder distribution, under a low oxygen atmosphere, might have a positive effect on bulk printed samples, but moisture absorption and flow challenges in small particles of irregular shape (high friction and surface area) made them practically less useful for SLM experiments.
 3. Optimum VED for achieving high density SLMed parts does not exist as a single value for a given powder type, and rather dynamically changes with laser power. The relationship between VED and relative material density plateaus at lower power input levels for bimodal powders than for single mode. Below ~200W, with the constant parameters used in this study, bimodal powder had consistently higher as-built density than single mode powder. Beyond 200W, increasing VED (81.2 J/mm³) decreased material density in bimodal powders, possibly due to the small powder in the mixture vaporizing with higher energy input, leaving voids from vapor recoil pressure in the larger powder left behind.
 4. Melt pool depth is relatively consistent between single mode and bimodal samples at the same VED. Microstructure shows no discernable differences related to powder type used.

5. Hardness vs VED appears somewhat inversely proportional to density vs VED for both bimodal and single mode samples, but differences in material composition of each powder batch appeared to have a higher influence on hardness than the VED used to produce each sample.
6. Annealing samples resulted in coarsening of grains within the melt pool and formation of new grains along melt pool boundaries. Behavior of grain growth during annealing did not appear to differ between samples produced with bimodal and those produced with single mode.

5.2. Current Limitations and Future Work

Inherent limitations in the scope and assembly used in this study leave room for further investigation to validate current findings and explore other aspects of performing SLM with bimodal feedstock powder.

Unique rotational spreading motion of the SLM system used in this study resulted in an inconsistent powder coating velocity between different locations on the build platform relative to the center of rotation. Further study may require investigation of the effect of coater speed on the density of the powder bed. This may be particularly relevant to powders with less than excellent flow properties, such as the bimodal feedstock used in this study.

Furthermore, a wider set of power and scan speed for SLMed parts should be explored to investigate the density of parts produced at lower VEDs with higher power and scan speed. In this system, the power level can only reach approximately 225W, but

certainly the limits of the upward trajectory of the 100W (50% power) curve could be tested by running at extremely slow scan speeds. Single track experiments could be useful in the future work to quantify the effect of energy parameters on melt pool geometry. Tensile tests should be performed on samples with the highest densities to further explore the influence of feedstock PSD on mechanical strength of built parts.

Element analysis and mapping such as EDS should be performed in larger portions of the sample, as well as in the annealed SLM samples, to seek evidence of any segregation and unexpected compounds in the build matrix that may help explain melting behavior. Since this study was performed using nitrogen for the gas atmospheres in the SLM build chamber, and most studies on SLM of 316L use argon instead, samples should be built in an argon environment, under the same conditions as this study, to determine if the type of inert gas has any influence in this case.

A more aggressive and automated mixing strategy should be employed in the future to ensure bimodal distribution carries throughout the spreading and melting process. Furthermore, since bimodal powder beds show significant increase in density through mechanical tapping, development and implementation of a vibrating build platform in SLM that would assist powder in consolidating into optimal packing arrangement could be a solution to many of the flow and spreading difficulties that limit the advantages of using bimodal powder feedstock.

6. References

- [1] C. Kamath, B. El-dasher, G. F. Gallegos, W. E. King, and A. Sisto, "Density of additively-manufactured, 316L SS parts using laser powder-bed fusion at powers up to 400 W," *Int. J. Adv. Manuf. Technol.*, vol. 74, no. 1–4, pp. 65–78, 2014.
- [2] M. Rombouts, J.-P. Kruth, L. Froyen, and P. Mercelis, "Fundamentals of selective laser melting of alloyed steel powders," *CIRP Ann.-Manuf. Technol.*, vol. 55, no. 1, pp. 187–192, 2006.
- [3] B. Zhang, L. Dembinski, and C. Coddet, "The study of the laser parameters and environment variables effect on mechanical properties of high compact parts elaborated by selective laser melting 316L powder," *Mater. Sci. Eng. A*, vol. 584, pp. 21–31, 2013.
- [4] E. Liverani, S. Toschi, L. Ceschini, and A. Fortunato, "Effect of selective laser melting (SLM) process parameters on microstructure and mechanical properties of 316L austenitic stainless steel," *J. Mater. Process. Technol.*, vol. 249, pp. 255–263, 2017.
- [5] A. B. Spierings and G. Levy, "Comparison of density of stainless steel 316L parts produced with selective laser melting using different powder grades," presented at the Proceedings of the Annual International Solid Freeform Fabrication Symposium, 2009, pp. 342–353.
- [6] H. H. Zhu, J. Y. H. Fuh, and L. Lu, "The influence of powder apparent density on the density in direct laser-sintered metallic parts," *Int. J. Mach. Tools Manuf.*, vol. 47, no. 2, pp. 294–298, Feb. 2007.
- [7] R. K. McGEARY, "Mechanical Packing of Spherical Particles," *J. Am. Ceram. Soc.*, vol. 44, no. 10, pp. 513–522, 1961.
- [8] R. German, *Particle Packing Characteristics*. Princeton, NJ: Metal Powder Industries Federation, 1989.
- [9] N. Karapatis, G. Egger, P. Gygax, and R. Glardon, "Optimization of powder layer density in selective laser sintering," presented at the Proc. of Solid Freeform Fabrication Symposium 1999, 1999, pp. 255–263.
- [10] T. Do, P. Kwon, and C. S. Shin, "Process development toward full-density stainless steel parts with binder jetting printing," *Int. J. Mach. Tools Manuf.*, vol. 121, pp. 50–60, 2017.

- [11] B. Liu, R. Wildman, C. Tuck, I. Ashcroft, and R. Hague, "Investigation the effect of particle size distribution on processing parameters optimisation in selective laser melting process," *Addit. Manuf. Res. Group Loughb. Univ.*, pp. 227–238, 2011.
- [12] M. Ma, Z. Wang, and X. Zeng, "A comparison on metallurgical behaviors of 316L stainless steel by selective laser melting and laser cladding deposition," *Mater. Sci. Eng. A*, vol. 685, pp. 265–273, 2017.
- [13] U. Scipioni Bertoli, A. J. Wolfer, M. J. Matthews, J.-P. R. Delplanque, and J. M. Schoenung, "On the limitations of Volumetric Energy Density as a design parameter for Selective Laser Melting," *Mater. Des.*, vol. 113, pp. 331–340, Jan. 2017.
- [14] G. Aggen and M. Allen, "ASM Handbook Volume I Properties and Selection: Irons, Steels, and High-Performance Alloys," 2018.
- [15] Y. Y. Sun, S. Gulizia, C. H. Oh, C. Doblin, Y. F. Yang, and M. Qian, "Manipulation and Characterization of a Novel Titanium Powder Precursor for Additive Manufacturing Applications," *JOM*, vol. 67, no. 3, pp. 564–572, Mar. 2015.
- [16] "Standard Test Methods for Flow Rate of Metal Powders Using the Hall Flowmeter Funnel," 17.
- [17] "Standard Test Methods for Flow Rate of Metal Powders Using the Carney Funnel," 16.
- [18] H. Y. Saw, C. E. Davies, A. H. J. Paterson, and J. R. Jones, "Correlation between Powder Flow Properties Measured by Shear Testing and Hausner Ratio," *Procedia Eng.*, vol. 102, pp. 218–225, Jan. 2015.
- [19] R. O. Grey and J. K. Beddow, "On the Hausner Ratio and its relationship to some properties of metal powders," *Powder Technol.*, vol. 2, no. 6, pp. 323–326, Sep. 1969.
- [20] M. Krantz, H. Zhang, and J. Zhu, "Characterization of powder flow: Static and dynamic testing," *Powder Technol.*, vol. 194, no. 3, pp. 239–245, Sep. 2009.
- [21] S. L. Sing, W. Y. Yeong, and F. E. Wiria, "Selective laser melting of titanium alloy with 50 wt% tantalum: Microstructure and mechanical properties," *J. Alloys Compd.*, vol. 660, pp. 461–470, 2016.
- [22] M. Van den Eynde, L. Verbelen, and P. Van Puyvelde, "Assessing polymer powder flow for the application of laser sintering," *Powder Technol.*, vol. 286, pp. 151–155, Dec. 2015.
- [23] Y. Bai and C. B. Williams, "An exploration of binder jetting of copper," *Rapid Prototyp. J.*, vol. 21, no. 2, pp. 177–185, Mar. 2015.

- [24] H. W. Mindt, M. Megahed, N. P. Lavery, M. A. Holmes, and S. G. R. Brown, "Powder Bed Layer Characteristics: The Overseen First-Order Process Input," *Metall. Mater. Trans. A*, vol. 47, no. 8, pp. 3811–3822, Aug. 2016.
- [25] F. Zok, F. F. Lange, and J. R. Porter, "Packing Density of Composite Powder Mixtures," *J. Am. Ceram. Soc.*, vol. 74, no. 8, pp. 1880–1885, 1991.
- [26] Y. Liu, Y. Yang, S. Mai, D. Wang, and C. Song, "Investigation into spatter behavior during selective laser melting of AISI 316L stainless steel powder," *Mater. Des.*, vol. 87, pp. 797–806, Dec. 2015.
- [27] P. Yuan and D. Gu, "Molten pool behaviour and its physical mechanism during selective laser melting of TiC/AlSi10Mg nanocomposites: simulation and experiments," *J. Phys. Appl. Phys.*, vol. 48, no. 3, p. 035303, 2015.
- [28] J. Ciurana, L. Hernandez, and J. Delgado, "Energy density analysis on single tracks formed by selective laser melting with CoCrMo powder material," *Int. J. Adv. Manuf. Technol.*, vol. 68, no. 5, pp. 1103–1110, Sep. 2013.
- [29] H. Gong, K. Rafi, H. Gu, T. Starr, and B. Stucker, "Analysis of defect generation in Ti–6Al–4V parts made using powder bed fusion additive manufacturing processes," *Addit. Manuf.*, vol. 1–4, pp. 87–98, Oct. 2014.
- [30] H. Gong, K. Rafi, H. Gu, G. D. Janaki Ram, T. Starr, and B. Stucker, "Influence of defects on mechanical properties of Ti–6Al–4V components produced by selective laser melting and electron beam melting," *Mater. Des.*, vol. 86, pp. 545–554, Dec. 2015.
- [31] S. A. Khairallah, A. T. Anderson, A. Rubenchik, and W. E. King, "Laser powder-bed fusion additive manufacturing: Physics of complex melt flow and formation mechanisms of pores, spatter, and denudation zones," *Acta Mater.*, vol. 108, pp. 36–45, Apr. 2016.
- [32] C. Qiu, C. Panwisawas, M. Ward, H. C. Basoalto, J. W. Brooks, and M. M. Attallah, "On the role of melt flow into the surface structure and porosity development during selective laser melting," *Acta Mater.*, vol. 96, pp. 72–79, Sep. 2015.
- [33] J. Cherry, H. Davies, S. Mehmood, N. Lavery, S. Brown, and J. Sienz, "Investigation into the effect of process parameters on microstructural and physical properties of 316L stainless steel parts by selective laser melting," *Int. J. Adv. Manuf. Technol.*, vol. 76, no. 5–8, pp. 869–879, Feb. 2015.
- [34] R. Casati, J. Lemke, and M. Vedani, "Microstructure and fracture behavior of 316L austenitic stainless steel produced by selective laser melting," *J. Mater. Sci. Technol.*, vol. 32, no. 8, pp. 738–744, 2016.

- [35] Z. Sun, X. Tan, S. B. Tor, and W. Y. Yeong, "Selective laser melting of stainless steel 316L with low porosity and high build rates," *Mater. Des.*, vol. 104, pp. 197–204, Aug. 2016.
- [36] S. Wang *et al.*, "Research on high layer thickness fabricated of 316L by selective laser melting," *Materials*, vol. 10, no. 9, p. 1055, 2017.
- [37] T. Simson, A. Emmel, A. Dwars, and J. Böhm, "Residual stress measurements on AISI 316L samples manufactured by selective laser melting," *Addit. Manuf.*, vol. 17, pp. 183–189, Oct. 2017.
- [38] A. Röttger, K. Geenen, M. Windmann, F. Binner, and W. Theisen, "Comparison of microstructure and mechanical properties of 316L austenitic steel processed by selective laser melting with hot-isostatic pressed and cast material," *Mater. Sci. Eng. A*, vol. 678, pp. 365–376, Dec. 2016.
- [39] J. Suryawanshi, K. G. Prashanth, and U. Ramamurty, "Mechanical behavior of selective laser melted 316L stainless steel," *Mater. Sci. Eng. A*, vol. 696, pp. 113–121, Jun. 2017.
- [40] R. Li, Y. Shi, Z. Wang, L. Wang, J. Liu, and W. Jiang, "Densification behavior of gas and water atomized 316L stainless steel powder during selective laser melting," *Appl. Surf. Sci.*, vol. 256, no. 13, pp. 4350–4356, Apr. 2010.
- [41] Y. Sun, A. Moroz, and K. Alrbaey, "Sliding Wear Characteristics and Corrosion Behaviour of Selective Laser Melted 316L Stainless Steel," *J. Mater. Eng. Perform.*, vol. 23, no. 2, pp. 518–526, Feb. 2014.
- [42] D. Wang, C. Song, Y. Yang, and Y. Bai, "Investigation of crystal growth mechanism during selective laser melting and mechanical property characterization of 316L stainless steel parts," *Mater. Des.*, vol. 100, pp. 291–299, Jun. 2016.
- [43] T. Kurzynowski, K. Gruber, W. Stopyra, B. Kuźnicka, and E. Chlebus, "Correlation between process parameters, microstructure and properties of 316 L stainless steel processed by selective laser melting," *Mater. Sci. Eng. A*, vol. 718, pp. 64–73, Mar. 2018.
- [44] Y. Zhong, L. Liu, S. Wikman, D. Cui, and Z. Shen, "Intragranular cellular segregation network structure strengthening 316L stainless steel prepared by selective laser melting," *J. Nucl. Mater.*, vol. 470, pp. 170–178, Mar. 2016.
- [45] F. Bartolomeu *et al.*, "316L stainless steel mechanical and tribological behavior—A comparison between selective laser melting, hot pressing and conventional casting," *Addit. Manuf.*, vol. 16, pp. 81–89, Aug. 2017.

- [46] J. W. Fu, Y. S. Yang, J. J. Guo, and W. H. Tong, "Effect of cooling rate on solidification microstructures in AISI 304 stainless steel," *Mater. Sci. Technol.*, vol. 24, no. 8, pp. 941–944, Aug. 2008.
- [47] M. Nastac, R. L. A. Klein, and I. ExOne, "MICROSTRUCTURE AND MECHANICAL PROPERTIES COMPARISON OF 316L PARTS PRODUCED BY DIFFERENT ADDITIVE MANUFACTURING PROCESSES."
- [48] W. M. Tucho, V. H. Lysne, H. Austbø, A. Sjolyst-Kverneland, and V. Hansen, "Investigation of effects of process parameters on microstructure and hardness of SLM manufactured SS316L," *J. Alloys Compd.*, vol. 740, pp. 910–925, Apr. 2018.
- [49] M. A. Easton and D. H. StJohn, "Improved prediction of the grain size of aluminum alloys that includes the effect of cooling rate," *Mater. Sci. Eng. A*, vol. 486, no. 1, pp. 8–13, Jul. 2008.
- [50] J. Dai *et al.*, "Effects of Cooling Rate and Solute Content on the Grain Refinement of Mg-Gd-Y Alloys by Aluminum," *Metall. Mater. Trans. A*, vol. 45, no. 10, pp. 4665–4678, Sep. 2014.
- [51] A. B. Spierings, M. Schneider, and R. Eggenberger, "Comparison of density measurement techniques for additive manufactured metallic parts," *Rapid Prototyp. J.*, Apr. 2013.
- [52] H. Alsalla, L. Hao, and C. Smith, "Fracture toughness and tensile strength of 316L stainless steel cellular lattice structures manufactured using the selective laser melting technique," *Mater. Sci. Eng. A*, vol. 669, pp. 1–6, 2016.
- [53] P. Li, "Constitutive and failure behaviour in selective laser melted stainless steel for microlattice structures," *Mater. Sci. Eng. A*, vol. 622, pp. 114–120, Jan. 2015.
- [54] C. Yan, L. Hao, A. Hussein, P. Young, and D. Raymont, "Advanced lightweight 316L stainless steel cellular lattice structures fabricated via selective laser melting," *Mater. Des.*, vol. 55, pp. 533–541, Mar. 2014.
- [55] R. Song, J. Xiang, and D. Hou, "Characteristics of Mechanical Properties and Microstructure for 316L Austenitic Stainless Steel," *J. Iron Steel Res. Int.*, vol. 18, no. 11, pp. 53–59, Nov. 2011.
- [56] "Standard Test Method for Tap Density of Metal Powders and Compounds," 15.
- [57] M. Yakout, M. A. Elbestawi, and S. C. Veldhuis, "Density and mechanical properties in selective laser melting of Invar 36 and stainless steel 316L," *J. Mater. Process. Technol.*, vol. 266, pp. 397–420, Apr. 2019.

- [58] C. Kamath, B. El-dasher, G. F. Gallegos, W. E. King, and A. Sisto, "Density of additively-manufactured, 316L SS parts using laser powder-bed fusion at powers up to 400 W," *Int. J. Adv. Manuf. Technol.*, vol. 74, no. 1–4, pp. 65–78, 2014.
- [59] McGEARY R. K., "Mechanical Packing of Spherical Particles," *J. Am. Ceram. Soc.*, vol. 44, no. 10, pp. 513–522, Jun. 2006.
- [60] R. B. Shah, M. A. Tawakkul, and M. A. Khan, "Comparative Evaluation of Flow for Pharmaceutical Powders and Granules," *AAPS PharmSciTech*, vol. 9, no. 1, pp. 250–258, Mar. 2008.
- [61] C. V. Navaneethan, S. Missaghi, and R. Fassihi, "Application of powder rheometer to determine powder flow properties and lubrication efficiency of pharmaceutical particulate systems," *AAPS PharmSciTech*, vol. 6, no. 3, pp. E398–E404, Sep. 2005.
- [62] J. Clayton, D. Millington-Smith, and B. Armstrong, "The Application of Powder Rheology in Additive Manufacturing," *JOM*, vol. 67, no. 3, pp. 544–548, Mar. 2015.
- [63] G. Egger, P. E. Gygax, R. Glardon, and N. P. Karapatis, "Optimization of powder layer density in selective laser sintering," *Solid Free. Fabr. Proc. August 1999*, pp. 255–263, 1999.
- [64] K. Bala, P. R. Pradhan, N. S. Saxena, and M. P. Saksena, "Effective thermal conductivity of copper powders," *J. Phys. Appl. Phys.*, vol. 22, no. 8, p. 1068, 1989.
- [65] G. Guan, M. Hirsch, W. P. Syam, R. K. Leach, Z. Huang, and A. T. Clare, "Loose powder detection and surface characterization in selective laser sintering via optical coherence tomography," *Proc R Soc A*, vol. 472, no. 2191, p. 20160201, Jul. 2016.
- [66] "byko-drive XL – Automatic Film Applicator with the most flexible design to perform drawdowns of coating and inks," *BYK-Gardner Laboratories Blog*, 26-May-2017. .

Appendix A – Publication from Thesis

Conference Proceedings Publication – Presented at MS&T 2018:

USE OF 316L STAINLESS STEEL POWDER WITH BIMODAL SIZE DISTRIBUTION IN SELECTIVE LASER MELTING

Hannah G. Coe¹, Dr. Somayeh Pasebani¹

¹School of Mechanical, Industrial & Manufacturing Engineering
Oregon State University
Corvallis, Oregon

Keywords:

316L, Selective laser melting, Additive manufacturing, Bimodal powder size distribution

Abstract

One issue of manufacturing fully dense metal parts via selective laser melting (SLM) can be addressed by maximizing the packing density of the powder feedstock in the powder bed before melting. Voids between particles can result in poor mechanical behavior due to low relative densities and warping due to non-uniform shrinkage. In this study, our objective was to improve the density of 316L stainless steel samples produced by SLM by using a bimodal powder size distribution. To do this, a primary powder of a larger size range was combined with a smaller particle size that fills the interstitial regions between the larger particles. The packing density and flowability of the mixed bimodal feedstock powder was determined by measuring tap density and Hausner ratio. These mixed powders were then processed by SLM and the resulting samples were measured for density relative to the parent material. Bimodal feedstock powder mixtures with the powders used in this study did not yield higher density SLM powders than a normally distributed, single mode feedstock. However, maximum (tapped) density of the bimodal size distributions were up to 2% greater than the normally distributed powder. This indicates the potential for future studies to explore the use of bimodal powders to increase powder bed density.

1. Introduction

Over the last few decades, powder-based additive manufacturing technologies such as selective laser melting (SLM) have been developed rapidly into useful tools that could soon replace or supplement many traditional metal manufacturing methods such as subtractive machining and casting [2]. In SLM, a solid metallic part can be produced as a single solid object by melting thin layers of metal, with a high-powered laser, in the shape of individual “slices” of the 3D object. Each layer then solidifies quickly, allowing a 3D object to be built by repeatedly spreading, and then melting, a new layer of powder over the surface of the previously solidified layer [58].

Recent SLM studies have shown that many metal alloys can be printed to ~ 99% of full density [3]. Maximum density is critical to the quality of parts produced by SLM. Partially melted powder, poor layer adhesion, contaminants in the feedstock or atmosphere gas, or uneven spreading during SLM can result in voids and porosity in the solidified material [3-5]. These defects, even in small concentrations, can reduce the density of the material and negatively affect the mechanical characteristics of parts produced by SLM. Powder layer thickness, laser power, laser scan speed and other build parameters can be adjusted to increase the consolidation of the powder bed and ensure high density in the final part, but these parameters cannot control the density of the pre-melted powder bed. The powder bed density for normally distributed powder sizes is typically around 60% of the bulk material density. [6]. Maximizing this relative density of the powder bed could result in improved density and dimensional accuracy in solid parts produced by SLM

Our objective in this study was to compare the packing density of a typical SLM feedstock powder, having a normal particle size distribution, with two powders having bimodal distributions of particle sizes. After comparing the packing density of these three powder size distributions, our goal was then to manufacture solid samples via SLM and compare the density of samples produced with bimodal powders to samples produced with a single mode powder size distribution. Our theory was that the bimodal powders would have greater packing density in the SLM powder bed and would thus result in denser solid parts.

1.1. Bimodal Powder

The fractional packing density, f , refers to the ratio of the density of the powder bed relative to the density of the bulk material (Equation 1). In this study, 316L stainless steel will be used, which has a material density, ρ_{material} , of approximately 8.0 g/cm³ [14].

$$f = \frac{\rho_{\text{powder}}}{\rho_{\text{material}}} \quad \text{Equation 1}$$

Intermediate-sized particles in normally-distributed powder can inhibit complete packing of larger particles in a powder bed. Since these particles are not small enough to fill the interstices between large particles in contact with each other, they can push the large particles apart, resulting in lower fractional packing density than mixtures with two distinct particle sizes [8]. Early work by McGearry [59] showed that for powder bulks, the optimal

achievable density was found using a mixture of fine and coarse powders, with a size ratio between them being approximately 1:7, and a composition of approximately 30% fine particles. In addition to being experimentally validated, the size relationship can be approximated geometrically according to Equation 2, where r is the radius of fine particles and R is the radius of coarse particles.

$$r = \left(\frac{2}{\sqrt{3}} - 1 \right) \cdot R \cong \frac{1}{7} R \quad \text{Equation 2}$$

Studies reported by R. German in 1989 [8] showed that, in practice, the fractional packing density in bimodal powder beds continues to increase with increasing particle size ratio beyond 7:1, with the effect beginning to plateau around 20:1 as shown in Figure 1. However, as the plot shows, the size ratio at which a bimodal distribution begins to significantly improve the powder bed density is still identified as approximately 7:1, which agrees with Equation 2.

For spherical particles of the same material, the weight fraction of large particles required for saturation (all the gaps in the large particles filled by small particles, resulting in optimal packing density), can be mathematically determined from the fractional packing density of the fine and coarse powders as described by Equation 3 [8,62].

$$X_L^* = \frac{f_L}{(f_L + (1 - f_L)f_S)}, \quad X_S^* = 1 - X_L^* \quad \text{Equation 3}$$

Where f_L is the fractional packing density of the large particles and f_S is the fractional packing density of the small particles.

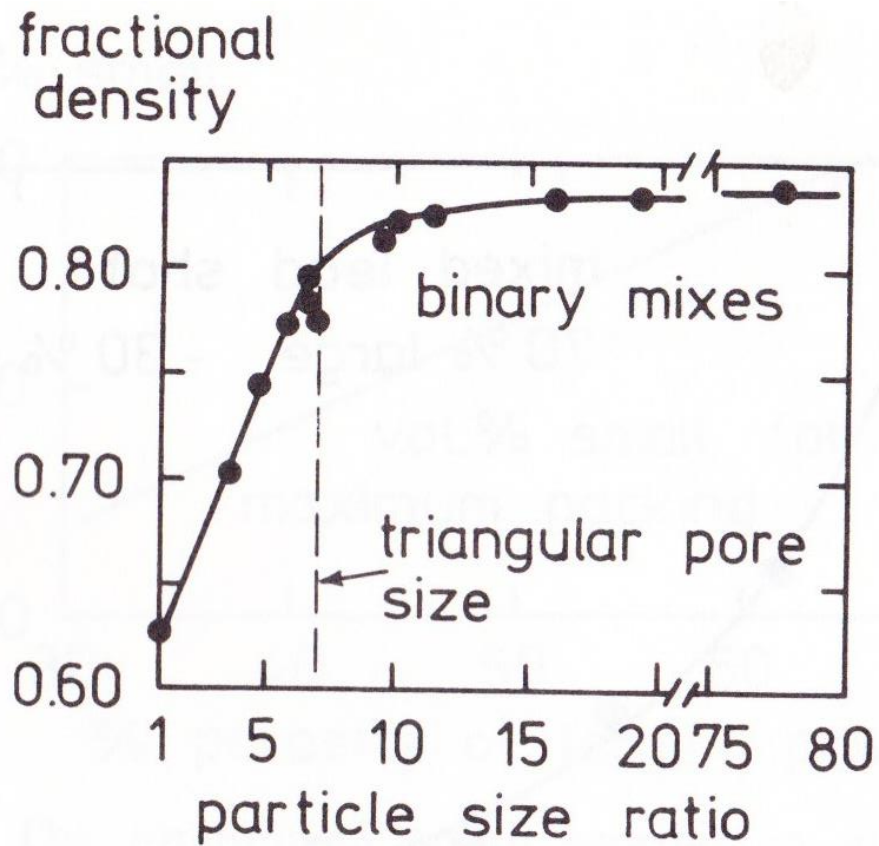


Figure 1. Ratio of large to small particles and its effect on fractional packing density [8]

2. Materials

An alloy of particular interest for use in selective laser melting and other additive manufacturing process is 316L stainless steel. As a low-carbon, austenitic steel, 316L is less prone to embrittlement due to carbide formation, and is desirable for its strength, toughness, and corrosion resistance. In this study, we determined mixing ratios and packing density for two size distributions of Oerlikon Metco gas-atomized 316L spherical powder (A and B) combined with small, morphologically irregular 316L powder from US Nano Research (C). The reported chemical composition of each powder is given in Table 1. The size range of the constituent powders and bimodal mixtures are given in Table 2.

Table 1 - Composition of powders reported by manufacturer (wt%)

Powder	Supplier	Fe	Cr	Ni	Mo	Si	Mn	C	O	Other
A, B	Oerlikon Metco	Balance	17.0	12.0	2.5	2.3	1.0	0.03	-	<0.5
C	US Nano Research	Balance	16.5	12.4	2.6	0.5	0.075	0.02	0.337	<0.013

2.1. Size Analysis

As shown in Table 2, each bimodal powder was composed of a large primary particle size distribution mixed with a smaller secondary particle size distribution. In the first bimodal powder, the primary powder (A) was normally distributed with a D_{50} of ~30-35 μm ; and in the second bimodal powder (B), the primary powder was sorted to have a narrow size distribution between 38 μm and 45 μm . Size analysis performed by a Malvern Mastersizer 3000 showed that the secondary particle size for both bimodal powders (C) follows a normal size distribution with $D_{50}=5.68\pm0.072\mu\text{m}$, as shown in Figure 2. It should

be noted that while both large particle types are gas-atomized with a spherical particle shape, powder C possesses a combination of semi-spherical and irregular particles.

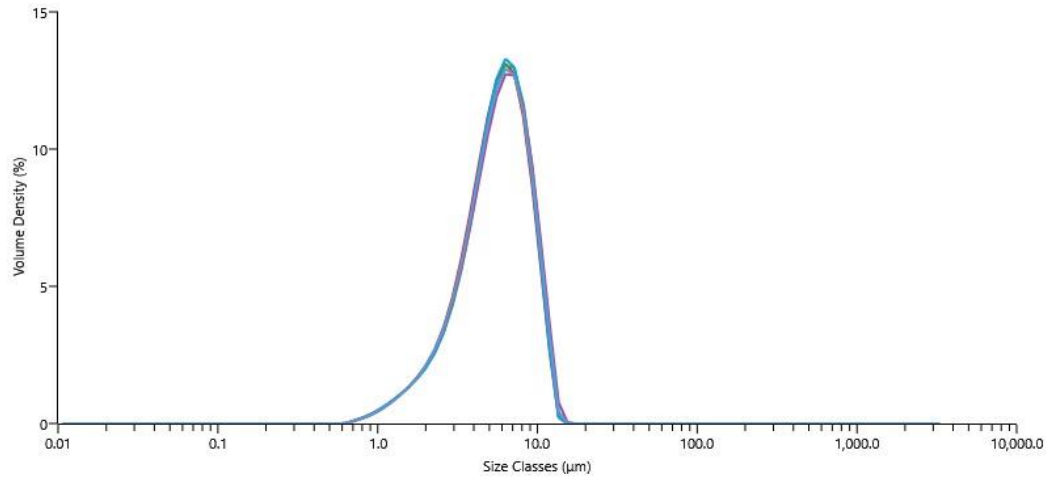


Figure 2. Particle size distribution histogram of small particles measured by Malvern particle size analyzer

2.2. Maximum Powder Density

Fractional packing density, f , was determined from the tap density of the powders. Tap density was measured according to standard procedure ASTM B527 [56]. The theoretical optimal mixing ratio of large and small particle sizes can be calculated using tap density (Equation 3), but apparent density is useful as well, since apparent density of a bulk powder is often similar to the density of a spread powder bed [6]. The tap density and apparent density are given in Table 2.

Table 2 - Powder size, mixing ratios and density values for different powder size distributions

	Powder type	Size range (μm)	Tap Density ρ_t (g/cm^3)	Fractional Packing Density $f = \left(\frac{\rho_t}{8.0 \text{ g}/\text{cm}^3}\right)$	Apparent Density ρ_a (g/cm^3)	Hausner Ratio $H = \left(\frac{\rho_t}{\rho_a}\right)$
A	gas-atomized, spherical	15-45	5.07 \pm 0.015	0.634	4.37 \pm 0.020	1.16
B	gas-atomized, spherical	38-45	4.95 \pm 0.021	0.619	4.90 \pm 0.061	1.14
C	irregular morphology	5-10	4.09 \pm 0.015	0.511	2.40 \pm 0.120	1.70
D	77.8 wt% A 22.8wt% C	5-30	5.15 \pm 0.096	0.644	3.70 \pm 0.049	1.39
E	75.6wt%B 24.4 wt%C	5-40	5.17 \pm 0.067	0.646	3.60 \pm 0.021	1.44

2.3. Flow Characteristics

The flowability of a powder used in SLM is closely related to quality at which powder will spread to evenly coat each layer of the build platform during the SLM process. The ratio of the tap density and the apparent density of a powder, known as the Hausner ratio, is often used to quantify the quality of powder flow [18]. Powders with an average Hausner ratio over 1.25 are generally considered to have poor flowability [18]. As shown in Table 2, the Hausner ratio of the small and bimodal powders is much higher than this threshold and thus are considered to have poor flowability, while fractional packing density is higher in both bimodal size distributions.

3. Experimental Methods

Since the exact ratio of powder sizes is limited by the distribution of the precursor powders, as well as the ability to effectively sort into distinct sizes, approximations were used in the ratio calculation. For the narrow and normal large powder size distributions, the D_{50} powder size is approximately $38\mu\text{m}$. If both large powders are assumed to be approximately $35\mu\text{m}$, and the small powder is assumed to be approximately $5\mu\text{m}$, then the required 7:1 size ratio is achieved. The composition of small as compared to large in the bimodal mixtures was calculated using the maximum density, f , of the individual modes from Table 2, according to Equation 3. The resulting calculated ideal mixing ratios are given in Table 2. Powders were mixed first by inverting the container by for hand 50 times, then mixing with a vortex shaker for 30 seconds at ~ 3000 rpm. Tap density of each bimodal composition is also given in Table 2.

3.1. Selective Laser Melting

SLM was performed using an OR LASER CREATOR - 1070nm, 250W Yb Fibre Laser under nitrogen atmosphere below 0.1% oxygen. A baseline for initial parameters was first determined by printing a set of samples with the single-mode powder distribution. Figure 3 shows the layout of $0.5 \times 0.5 \times 0.5 \text{ mm}^3$ test sections in the build envelope with different parameters printed simultaneously.

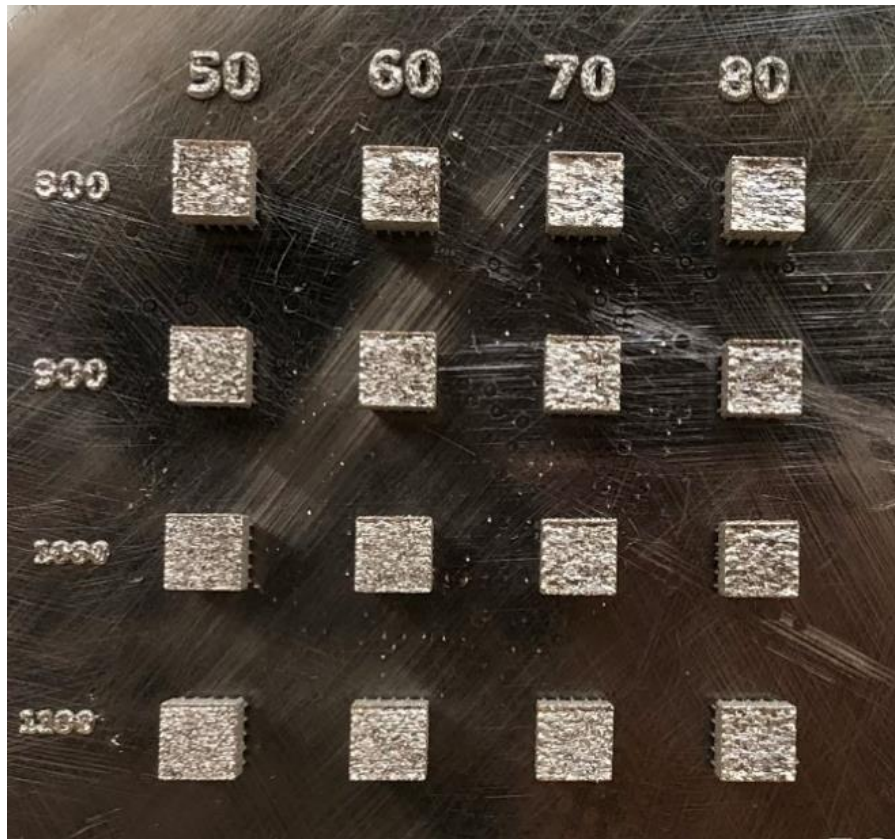


Figure 3. Layout of build platform with varied parameters (single mode particle size distribution is shown). Column labels are in power percentage increasing linearly, where 50% power = 107 W, 60% = 139 W, 70% = 178 W and 80% = 203W. Row labels are laser scan speed in mm/s. Each sample cube has dimensions of $0.5 \times 0.5 \times 0.5 \text{ mm}^3$.

The same layout was used for both bimodal powder size distributions and single mode powder size distribution. In addition to the power and scan speed shown in Figure 3, constant parameters included a spot size of $50 \mu\text{m}$, layer thickness of $50 \mu\text{m}$, line spacing of $50 \mu\text{m}$ and a horizontal scan pattern that rotates by a 45-degree angle for each new layer.

4. Results and Discussion

As shown in Figure 4, density is higher in SLM samples printed with single mode powder than for either of the bimodal distributions.

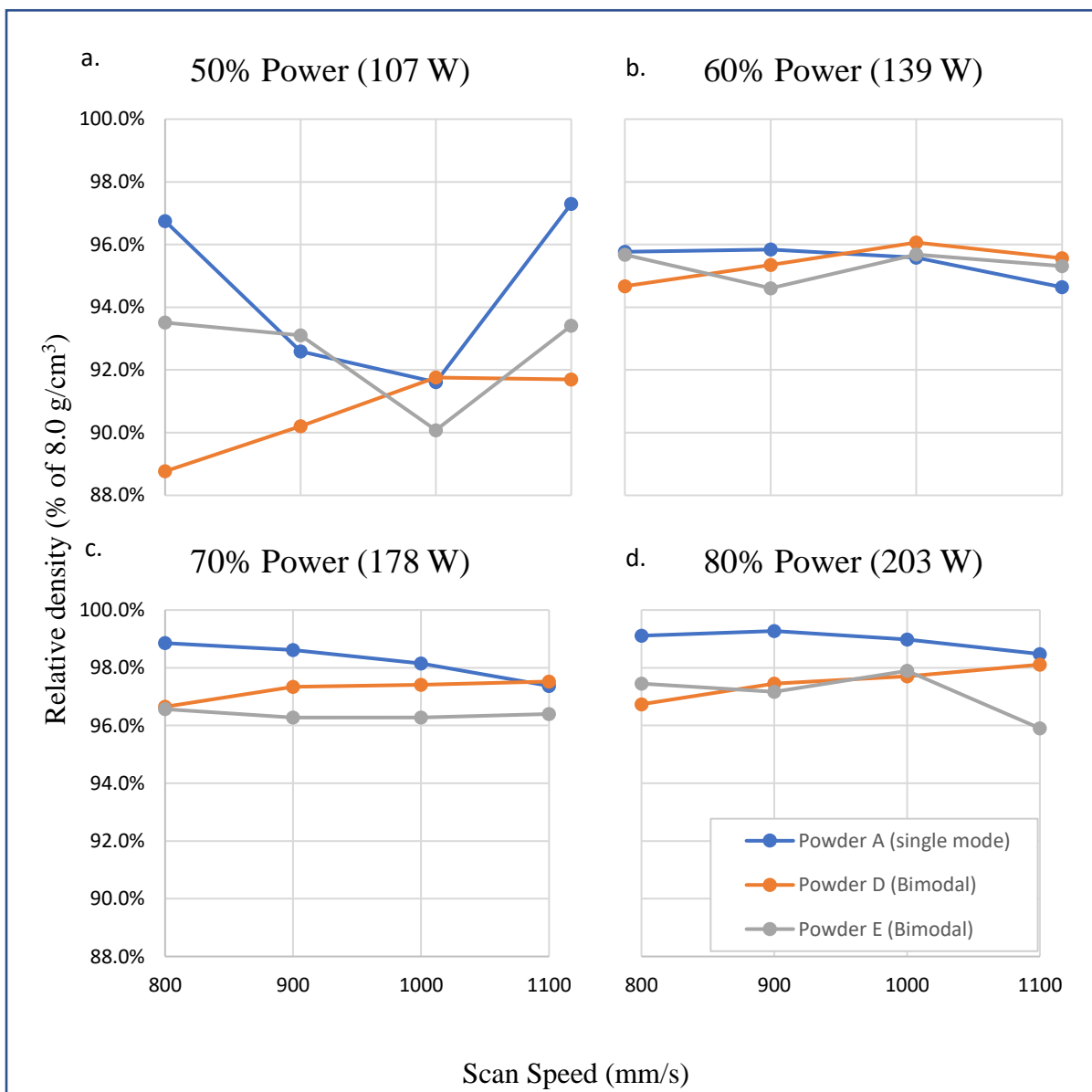


Figure 4. Relative density of samples manufactured by SLM at a.) 107W, b.) 139W, c.) 178W and d.) 203W

While the bimodal powders showed higher maximum packing density, the diminished flowability of the bimodal mixtures (as evidenced by their high hausner ratios) appears to have a significant impact on the density of the bulk samples manufactured by SLM. One reason for poor flowability in mixtures containing small particles is that particles with higher surface area to mass ratios tend to absorb more moisture from the air. In future work, effort must be made to ensure purity of fine powders and avoid moisture absorption, which can affect powder flowability.

Distribution E was expected to have a much higher packing density than distribution D, due to the presence of intermediate particle sizes in E. However, the tap density of distribution E, while slightly higher, is nearly the same as the tap density of distribution D, as shown in Table 2. The apparent density of distribution D is higher than that of distribution E, though this is mainly attributed to the higher concentration of poor-flowing small particles in distribution E.

Table 1 reveals some differences in nominal composition of the two powder types (Large powder manufactured by Metco, and small powder manufactured by US Nano Research). These differences in composition could significantly alter the accuracy of relative density measurements if the bulk density is assumed to be the same for both. For future accuracy, bulk density should be calculated for each precursor powder using nominal composition of each constituent powder. Further study is needed to investigate the effect of bimodal powder feedstock on porosity, mechanical properties, and microstructure.

5. Conclusions

In this preliminary study of the effects of bimodal powder size distributions on SLM of 316L stainless steel, we concluded the following:

- Bimodal size distributions can have higher maximum packing densities than normally distributed powders in a similar size range, even when the secondary-sized particles lack sphericity and purity.
- Despite higher packing density, samples manufactured via SLM using the bimodal compositions in this study have lower densities than samples produced using normal powder distributions. This is likely due to poor flow characteristics resulting in poor spreadability in the powder bed.
- Use of spherical small particles in a bimodal powder distribution, under a low oxygen atmosphere, may have a positive effect on bulk printed samples, but moisture absorption and flow challenges in small particles of irregular shape (high surface area) make them less useful for SLM.

6. Acknowledgements

The authors sincerely acknowledge the Oregon Manufacturing Innovation Center (OMIC) and the Oregon Metals Initiative (OMI) for their financial support. The authors are also grateful to the faculty and staff of the Advanced Manufacturing and Technology Institute (ATAMI) and the OR LASER technical support team.

Appendix B – Business Value and Impact on Industry

Metal powders are made for conventional press and sintering powder metallurgy should be evaluated as potential feedstock for SLM process. ATI Specialty Alloys and Components is an Oregon metal manufacturing company specializing in high temperature structural alloys (powder and bulk) for high performance applications and near-net shapes for the Defense, Aerospace, Nuclear and Energy production industries. ATI was going to work on qualifying their atomized metal powders for additive manufacturing applications and markets. Furthermore, ATI was interested in building a custom designed device to evaluate spreading ability of their powders and quantitatively measure powder layer properties. Figure B.1 illustrates an industrial application of this thesis.

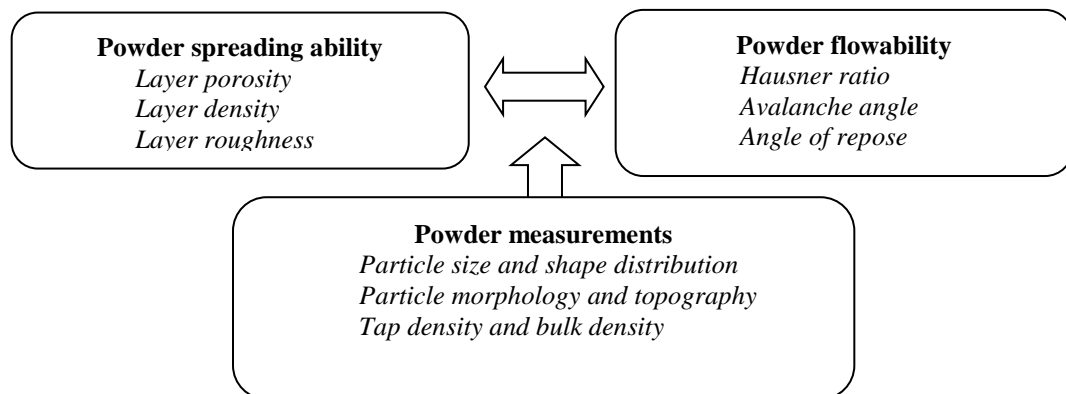


Figure B.1. Flowchart showing the quantitative measurements of powder characteristics required for SLM

Measuring correlation between flowability, spreading ability, powder layer density, particle size distribution and particle shape and morphology would present great interest to assess their impact on SLMed part quality. Test measurement techniques and methods to quantitatively measure ATI powder spreading quality and properties such as layer density, layer roughness and layer thickness were reviewed and summarized for ATI. The knowledge gained in this project could be used to design a re-coater device to test quality of powder spreading.

Industry Project Report:

Measurement of Characteristics of Spread Metal Powders for Selective Laser Melting: Investigation of Previous Work and Development of Experimental Prototype

INDUSTRY SPONSOR: ATI Specialty Alloys and Components, Dr. Nicholas Cunningham, (541)926-4211 x6254, Nicholas.Cunningham@ATImetals.com and Dr. Noah Philips, Noah.Philips@ATImetals.com

Abstract:

Metal feedstock powders used in additive manufacturing (AM) process like selective laser melting (SLM) vary in size, shape, and composition. Understanding the physical characteristics of the powder before printing is crucial in order to print high fidelity components. As AM is still an emerging industry, little effort has been made to find a correlation between the properties of a given powder and the achievable density or overall quality of a layer-by-layer spread powder bed. The goal of this project was to explore commonly practiced methods of measuring flow properties and density. This can be used to quantify spreadability in order to enhance quality of spread powder layers. In this project, we first reviewed current literature on methods for evaluating the behavior of powder during spreading in powder bed AM. Next, we designed and tested a simple method for measuring density of layer-wise spread powder to predict the density of a powder bed during SLM process.

1. Introduction

The purpose of this project was to develop a method for determining properties of metal powder feedstock used in powder bed-laser additive manufacturing processes. The goal was to develop a device for making simple, cheap and repeatable, relative measurements of powder layer properties; such as spread powder density, layer roughness, powder mobility, and thermal conductivity with minimal powder consumption or loss. These characteristics could then be compared to samples produced by SLM to identify a relationship between the layer properties of a powder, and the quality of a produced part.

2. Review of Literature on Particle Spreading and Packing Behavior

Various measurement methods are used for determining powdered material characteristics. These characteristics include density and surface roughness of spread powder, powder flowability, and thermal conductivity of pre-melted powder beds. The measurement methods described in the following review can be used to help understand the behavior of metal precursor powder used in powder bed fusion AM methods such as SLM and selective laser sintering (SLS). Although the goal is to apply these methods to metal powders, literature related to other powdered materials such as pharmaceuticals and polymer AM precursors were also reviewed. In the following section, studies performing these measurements have been summarized, followed by a discussion of possible applications for use in metal AM.

2.1. Flowability of Powders

Flowability, though not an absolute property of a given powder, is a characteristic commonly used to make predictions about the behavior of powders when they are spread into the powder bed. Properties that are generally attributed to powders with good flowability include density and surface roughness. Several types of values are commonly used to indicate the relative flow quality of powders, determined by a standard methodology.

2.1.1. Hall and Carney Flow Test Methods

One of the ASTM standard test methods commonly used to quantify flowability of powder is the Hall Flow test method [16]. The Hall technique is performed by first placing a funnel, like the one in Figure 1a, into a test stand as shown in Figure 1b. Then, a known mass of powder (typically 50g) is poured into the funnel while blocking the funnel tip. The tip barrier is then removed at the moment that a timer is started. The elapsed time required for all the powder to flow from the funnel into a container at the base is then used to calculate the Hall flow rate (FR_H) according to Equation 1, where t is the elapsed time in seconds.

$$FR_H = \frac{t}{50g} \quad \text{Equation 1}$$

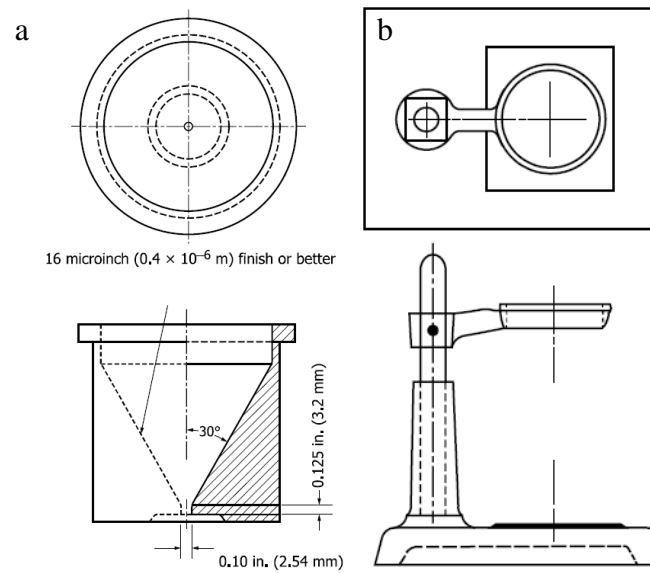


Figure 1. ASTM standard apparatus for Hall flow test method: (a) funnel and (b) stand [16]

The Carney flow test method is similar to the Hall technique, as illustrated by the familiar apparatus shown in Figure 2 [17]. For the carney method, however, the mass of powder varies (typically between 150g and 200g) depending on the material used. The same measurement procedure is used for both the Hall and Carney method. The Carney flow rate determined from elapsed time in seconds (t) and the powder mass in grams (M) as shown in Equation 2.

$$FR_C = \frac{t}{M}$$

Equation 2

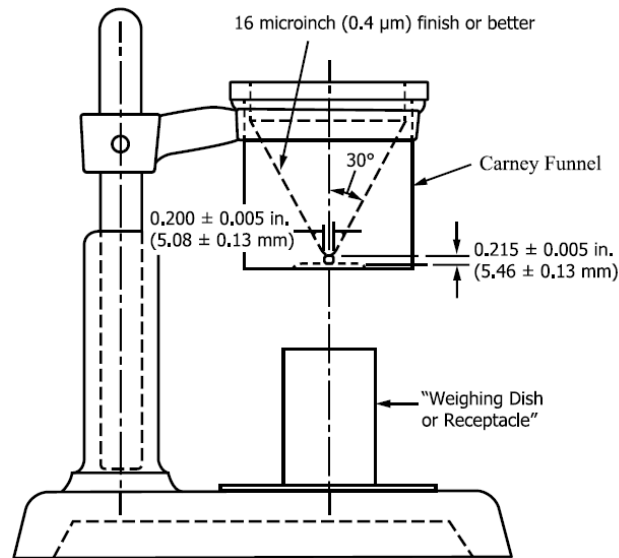


Figure 2. ASTM standard funnel and stand for carney flow method [17]

2.1.2. Hausner Ratio

Another attribute that determines good flowability is the Hausner ratio, H , of a powder. The Hausner ratio is a value found by comparing the bulk, or apparent density (AD) of a powder, ρ_B to the tapped density (TD) ρ_T , of the powder, according to Equation 3. Powders with a Hausner ratio less than 1.25 are generally considered to be “free flowing”[18].

$$H = \frac{\rho_T}{\rho_B} \quad \text{Equation 3}$$

Bulk density, also known as apparent density in many cases, is the density of the powder in the “as-filled” or “as-spread” state. Apparent density is often measured by pouring powder into a container of known volume from a funnel like those used in the Hall

and Carney methods. The mass of the powder, once leveled in the container, can then be divided by the volume to determine the density of the powder density in the cup. In the case of powders used in AM, apparent density may refer to the density of the powder that has been spread into the powder bed layer by layer [6]. Tapped density is the density of powder as measured from the volume occupied by a given mass of powder after it has been “tapped” or consolidated to its minimum height in a container by mechanical vibration. Neither the tapped density nor the bulk density is constant values for a given shape, size and composition of particle, as the results of such measurements may vary greatly by container size and shape. In the case of bulk density, the method used to distribute powder into the container can lead to different values.

2.1.3. Avalanche Angle and Angle of Repose

Another method for measuring the flowability and cohesiveness of powder is by determining the maximum angle a pile of powder that retains on its sides before the powder falls. Two of these types of measurements include the avalanche angle and the angle of repose. A study by Krantz, Zhang and Zhu, 2009, compares and describes these and other methods utilized by various industries for characterizing powders [20].

Angle of repose (AOR) is determined by a standard procedure in which powder is poured from a funnel onto a circular plate. As powder accumulates, it reaches a certain height such that, rather than accumulating into a taller peak, powder pours down the side of the pile, ultimately forming a cone. The angle of from the base plate to the side of the

cone is known as the angle of repose, as shown in the schematic in Figure 3. An AOR of $<30^\circ$ is generally regarded as excellent flow.

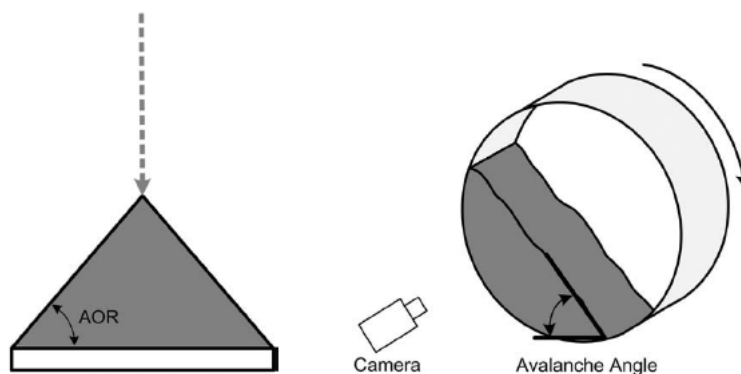


Figure 3. Angle of repose (left) and avalanche angle (right) schematics [20]

To measure the avalanche angle of a powder, a known tapped volume of powder is poured into a large cylindrical drum which is then rotated at a low, constant rpm with the cylinder's axis parallel to the ground. During rotation, cohesion between particle and between particles and the walls of the drum cause the heap of powder to maintain contact briefly with the wall. When the powder is carried high enough along the wall, it then “avalanches” at a characteristic angle known as the avalanche angle, as shown in Figure 3. A digital camera is used to observe this motion and determine the avalanche angle for a given powder.

2.1.4. Packing Ratio

In the production of pharmaceutical powders and other industries concerned with handling granular material, flowability (or the ability of a powder to be “poured”) accurately represent the quality of the material. However, for correlating flow properties

to success in powder bed fusion AM, a better descriptor for the behavior of particles would be the “spreadability” of a powder. Because, the bulk density described by powder flow models would then refer to the density of a powder after it has been spread, not poured. Therefore, a more appropriate measurement for correlating the spreading properties of a powder for its usefulness in SLS process is the packing density, ρ_p , as given in Equation 4 [22].

$$\rho_p = \frac{\rho_{layer}}{\rho_m} \quad \text{Equation 4}$$

Where ρ_{layer} is the density of a layer spread during the laser sintering processes and ρ_m is the density of the material from which the powder is made. Since, in practice, the maximum density that can be achieved in a powder bed is the tapped density, a measurement by which particles can be compared for their efficiency in laser sintering is the packing ratio, PR, in Equation 5.

$$PR = \frac{\rho_{layer}}{\rho_{tap}} \quad \text{Equation 5}$$

In a study by Bai and Williams, the Hausner ratio of a copper powder used for binder jetting was found by capturing the in-situ apparent density of powder that has undergone the spreading process. This was done by AM of an open cube of known volume, as shown in Figure 4, and measuring the mass of the loose powder bed inside the cube. The

method could potentially be adapted to selective laser melting to determine the density of the powder that was spread during the melting process [23].

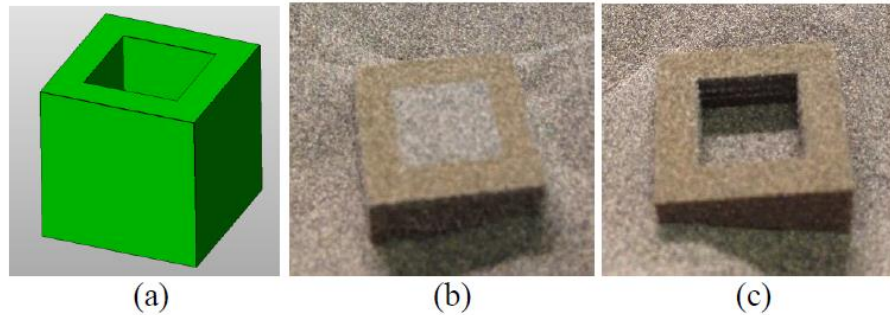


Figure 4. Test volume for measuring density of spread powder during binder jetting [23]

Van den Eynde et al (2015) designed a technique that mimics the spreading process in a laser sintering machine using polymer powder. This powder spreader device, shown in Figure 5, is composed of a modified spreading blade from a commercial motorized film applicator, which spreads a thin layer of powder, loaded into the front of the spreading blade, across a measurement plate. The measurement plate is located on a balance below the support plate, allowing for the mass of a powder sample to be measured. The density of the spread sample was then determined from this mass, and the volume of the sample (taken from the dimensions of the plate times the layer thickness) [22].

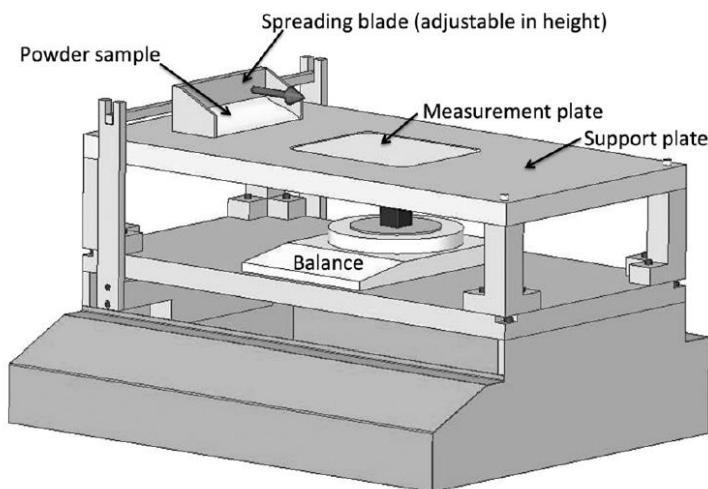


Figure 5. Powder spreader designed by Van den Eynde et al [22]

Layer thickness was set by raising or lowering the spreading blade (adjustable to a precision of $10\mu\text{m}$). To establish a uniform powder layer at the beginning of the measurement, the measuring plate was set to 1mm below the top surface of the support plate, and a layer of powder was spread with the blade set at $0\mu\text{m}$. Subsequent layers were added by raising the blade by $100\mu\text{m}$, loading about twice the amount of powder needed for a layer, and spreading the new layer. This was performed for 20 layers, with the balance being reset before each, thus allowing for the density of each layer to be recorded and averaged.

2.1.5. Rheological Methods for Evaluating Flow of Powder

Rheological methods have been widely used to measure and predict powder flowability, particularly for pharmaceutical powders [58-59]. However, some interest has recently been generated for exploring the use of powder rheology for characterizing metal

powders used in AM [62]. Cohesion and caking tend to be a less significant problem for metal powders than they are in pharmaceutical powders, given a higher influence of moisture content and Vander Waals forces in pharmaceuticals. However, powder speed flow dependence may still be a useful property to be aware of in powder spreading for AM. If a powder flows past the rheometer blade more easily at some rotational speeds than others, it may correlate to more consistent distribution and more efficient packing of particles spread in a powder bed for AM.

A study by Shah et al (2008) compared different methods for evaluating flow properties in pharmaceutical powders and granules. They used a force displacement transducer to analyze the cohesion, caking, and powder speed flow dependence of various dry and lubricated powders. A cylindrical container holds the powder, through which a rotating blade is passed as shown in Figure 6 . As the blade moves through the powder, it experiences a force of resistance. This force can be compared to the travelling distance to determine the force displacement profile generated by the rheometer [60].

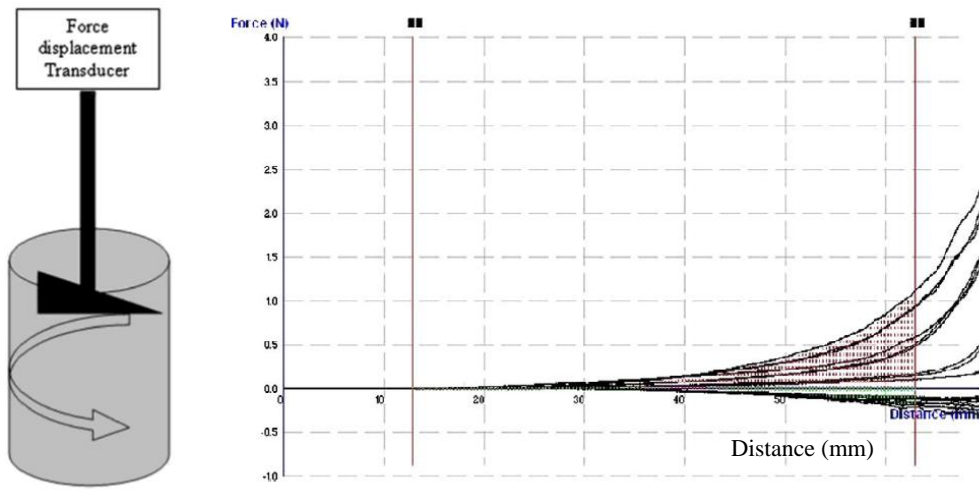


Figure 6. Typical force displacement profile (right) generated by a powder rheometer (schematic, left) in a powder flow stability test [60]

Similar work by Navaneethan et al (2005) used a powder rheometer to measure the torque experienced by a rotating propeller as it moves upward or downward through in a cylindrical powder container. Again, the amount of resistance (torque) experienced by the rheometer arm as it travels a known distance up or down through the cell is proportional to the flow quality. Force versus distance curves are used to characterize the cohesivity and flow of pharmaceutical powders with consistent and repeatable experiments [61].

Clayton et al (2015) suggest that powder rheology can be a useful tool in powder bed AM for detecting small changes in powder compositions. Whereas, the effects of powder composition on its behavior can be accurately measured in less sophisticated methods like angle of repose, and avalanche angle. By detecting subtle differences in batches, the process of reusing excess powder collected from a previous build can be optimized, thus contributing to less material waste. In their study, Clayton et al. (2015) used rheometer measurements of loose powder to compare the required displacement

energy of different batches: (1) from the same supplier, (2) powders of the same specifications from different suppliers, and (3) powders of the same size and composition but from different atomization methods (water atomized, gas atomized, etc.). The results were used to compare the effects of different additives on the properties of feedstock, and to identify differences between used and unused powders [62].

Since flowability is not an inherent material property, powder rheology does not necessarily provide thorough information on ability of a powder to flow in other equipment such as within the SLM machine. However, it can provide a reference for whether or not one powder might out-perform another. In this way, it is possible to claim that this method may be useful for selecting optimal materials for AM processes as well as managing the lifecycle of feedstock powders. To adequately explore and utilize properties determined by rheology, these properties must be correlated to the density of parts printed with the powder using SLM.

2.2. Density of Powder Beds

In powder manufacturing processes, the density of the loose powder bed has a direct impact on the density of the printed part. Therefore, by optimizing the density of the powder bed before printing, higher density and dimensional accuracy can be achieved in printed parts.

2.2.1. Effect of Morphology on Flowability and Density

In practice, most powder industries involve particles of irregular or non-spherical shape. Roughness of shape and surface can create friction between particles which limits their ability to flow into a packed structure. Randal German (1989) characterized powder roughness by the “relative roundness” of an irregular shaped particle, where a perfectly spherical particle has a roundness value of 1. Round particles flow past each other more easily and stack more neatly than irregular powders. So, the fractional packing density of a powder tends to be greater the more spherical the particle shape. This relationship between irregularity of shape and fractional density is shown in Figure 7 [8].

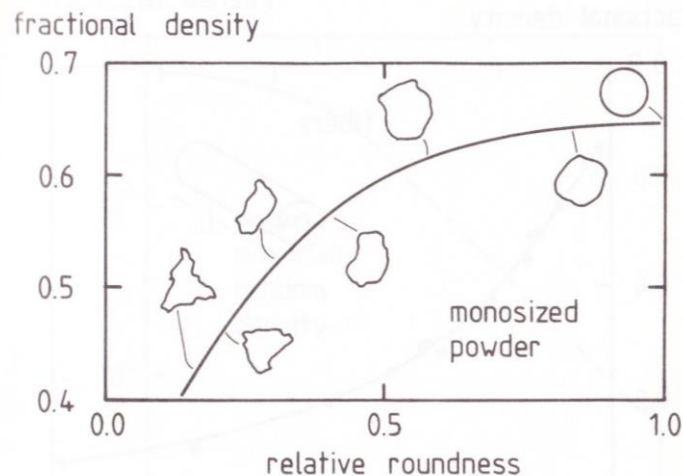


Figure 7. For randomly packed monosized particles, the fractional density can be heavily influenced by the relative roundness of the particles [8].

The sphericity, Ψ of a particle can be described by Equation 6, where S is the actual surface area of a particle and S_s is the surface area of a sphere of the same volume as the particle. The sphericity of a particle type may be experimentally approximated based on

the fractional tap density, f_t , according to the experimentally determined relationship in Equation 7.

$$\Psi = \frac{S_s}{S} \quad \text{Equation 6}$$

$$\Psi = 0.79 + 0.831f_t + 1.53f_t^3 \quad \text{Equation 7}$$

2.2.2. Effect of Particle Size Distribution and Composition

In a study by Karapatis (1999), both mathematical models and experimental procedures were used to determine the parameters influencing the powder layer density in SLS [63]. Early work by McGeary [59] showed that for powder bulks, the optimal achievable density was achieved using a mixture of fine and coarse powders, with a size ratio between them being of about 1:7, and a composition of about 30% fine particles. In addition to being experimentally validated, the size relationship can be expressed geometrically according to Equation 8, where r is the radius of fine particles and R is the radius of coarse particles.

$$r = \left(\frac{2}{\sqrt{3}} - 1 \right) \cdot R \equiv \frac{1}{7} R \quad \text{Equation 8}$$

The weight percentage of fine powders, X_{fines} that is required for optimal packing density can be determined from the relative density of the fine and coarse powders can be mathematically described by Equation 9.

$$X_{fines} = 1 - \frac{\rho_{coarse}}{\rho^*} = 1 - \frac{\rho_{coarse}}{\rho_{coarse} + (1 - \rho_{coarse}) \cdot \rho_{fines}} \quad \text{Equation 9}$$

Theoretically, assuming 60% for relative density of both the coarse powder, ρ_{coarse} , and the fine powder, ρ_{fines} , a maximum density, ρ^* , of 0.84 times the material density can be achieved using $X_{fines} = 30$ wt% fines.

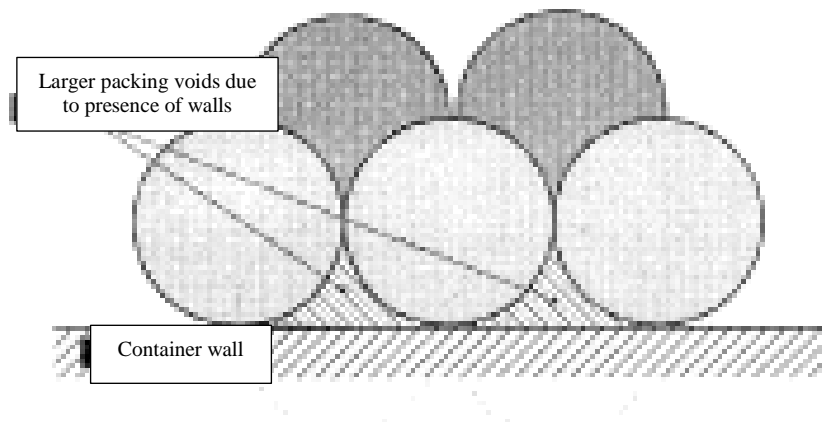


Figure 8. Effect of walls on void fraction in monodisperse packed particles [63]

McGeary's is true for powder bulks where the volume of the container is several orders of magnitude greater than the average particle size. It is noteworthy to mention that when the thickness is often less than ten times the particle diameter, the same size ratio and composition does not produce the same maximum packing density.

A greater dominance of wall effects is due to a higher concentration of voids in monodisperse particle packing (as shown in Figure 8), and therefore a higher concentration of fines is required to achieve maximum density. The void volume due to walls, V_{walls} ,

compared to the total void volume, V_{voids} , for an orthorhombic arrangement of particles of radius R , deposited in disk-shaped layer of diameter D and height h is given by Equation 10.

$$\frac{V_{walls}}{V_{voids}} = \frac{\frac{1}{3}\pi^2 R \cdot D \cdot \left(\frac{D}{4} + h\right)}{0.4 \cdot \pi \frac{D^2}{4} \cdot h + \frac{1}{3}\pi^2 R \cdot D \cdot \left(\frac{D}{4} + h\right)} \approx \frac{R \left(\frac{D}{4} + h\right)}{0.4 \frac{D}{4} \cdot h + R \left(\frac{D}{4} + h\right)} \quad \text{Equation 10}$$

Thus, the larger the cavity height for a given powder size, the smaller the total volume of voids along the wall. Total volume of voids between particles determines the relative density of the powder bed.

After testing ratios of various sizes and composition ratios of each size combination, Karapatis et al. (1999) determined that a size ratio of 1:10 between coarse and fine particles, using a 30% composition of fines, yields an increase of ~15% in density compared to monodisperse particles. For the purpose of this paper, however, relatively thick layers for SLS were used (around 500 μ m) and therefore, lower density yields are to be expected with yet thinner layers.

2.2.3. Powder Distribution onto Build Platform

The spread powder interacts differently with a smooth surface than it does in contact with a rough surface. From prior layers of built material. It is very important to understand the process of coating in a powder bed AM process to quantify the distribution of powder and heat source interaction in subsequent layers. A study by Mindt et al (2016)

recognizes the initial distribution of powder onto the processing table as an overseen first order input [24]. In this study, three separate powder layer values are used: processing table displacement (δ_t), fresh powder layer thickness (δ_p), and consolidated layer thickness (δ_c). The first parameter is set by the machine operator. The second parameter indicates the depth required for heat penetration. The third parameter represents the height addition to the final built part from a single spread of powder. The packing density, ρ_p (see Equation 4), relates the two measured values here by Equation 11:

$$\delta_c = \delta_p \rho_p \quad \text{Equation 11}$$

Thus, by adding the downward displacement of the table, the powder layer thickness of an upcoming layer ($n+1$) can be predicted by the density and thicknesses of the previous layer (n) according to Equation 12.

$$\delta_{p|n+1} = \delta_{t|n+1} + \delta_{p|n}(1 - \rho_{p|n}) \quad \text{Equation 12}$$

Figure 9 shows how the thickness of the powder increases with each table displacement for three assumed packing densities. According to the plot, powder layer thickness increases within the few initial layers until an equilibrium value is reached, after which the thickness of powder in each layer is approximately uniform. Higher packing density results in this stability being reached after fewer layers.

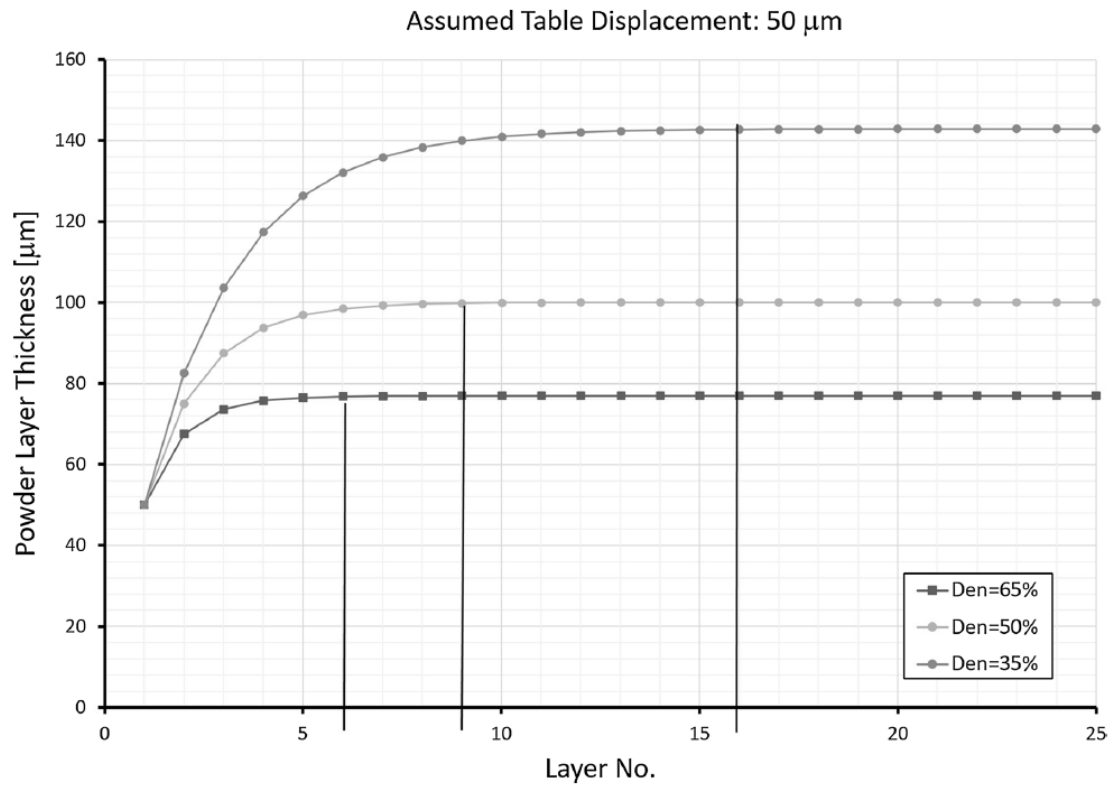


Figure 9. Powder layer thickness by layer number as a function of packing density [24]

2.3. Thermal Conductivity of Powder Beds

One of the more challenging powder properties to quantify is its thermal conductivity. While several measurement techniques have been designed to provide information about the behavior of heat from a laser source traveling through a powder bed, the values obtained through experimentation are highly varied as they represent relative conductivities rather than universal characteristics.

2.3.1. Transient Hot Strip Method

Bala et al (1989) utilized what is known as the transient hot strip method to measure thermal conductivity in copper powders [64]. In their experiments, a nickel strip is clamped between brass contacts and surrounded by a chamber of tapped copper powder which acts as an infinite medium. A schematic of the circuit used is illustrated in Figure 10. Constant current is passed through the strip, producing a mean temperature increment of about 1K. Resistance change from temperature results in a voltage drop across strip.

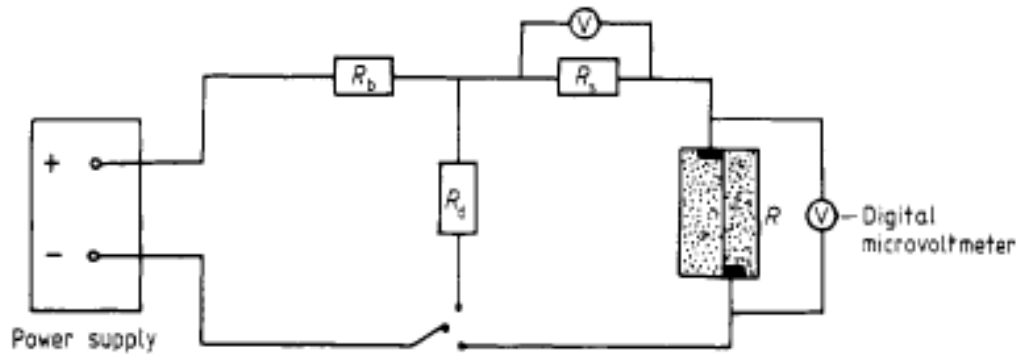


Figure 10. Circuit schematic for transient hot strip method [64]

Thus, the strip acts as both a heat source and as a sensor. By monitoring voltage drop over a period of time, the heat flow between the strip and the sample of loose powder can be relatively quantified.

Equation 13 shows the relationship under ideal conditions between instantaneous voltage (U) across the strip at time (t), the initial voltage across the strip (U_0), the

temperature coefficient of resistivity of the material of the strip (α) electrical current (I), and the thermal conductivity of the sample (λ).

$$U = U_0 + Cf(\tau) \quad \text{Equation 13}$$

$$C = \frac{\alpha IU_0^2}{4\sqrt{\pi\lambda h}}, \quad \tau = \frac{\sqrt{t}}{\theta}, \quad \theta = \frac{d^2}{k}$$

where $2h$ equals the length of the strip, d is equal to half the width of the strip, the characteristic time is denoted by θ , the function $f(\tau)$ is a complex error value function and k is the thermal diffusivity of the powder, respectively. The experimental calculation using this method was compared to a theoretical model for the effective thermal conductivity, λ_{eff} , of a porous medium in terms of a theoretically dense value of thermal conductivity, λ_{TD} , as shown in Equation 14, where ϕ is porosity of the powder sample.

$$\lambda_{\text{eff}} = \lambda_{\text{TD}}(1 - \phi)^{4/3} \quad \text{Equation 14}$$

The results of this study indicated that the effective thermal conductivity derived by experimentation was, on average, 96% of the thermal conductivity values determined by the theoretical methods. If the results of the experimental process are indicative of heat transfer properties of packed powder beds, then a model for conductivity can be approximated. In practice, however, measurement of porosity and contact between particles is more complicated for powders of different sizes, compositions and morphology.

Therefore, further study is necessary to determine the usefulness of either the theoretical model presented here or the transient hot strip method in predicting the interaction between a heat source and a powder bed in SLS.

2.4. Powder Bed Surface Roughness

A smoother surface of the powder bed after the spreading of each layer results in better bonding between layers and therefore better mechanical properties in a part printed by SLM. The surface quality of a printed part is also highly dependent on the loose powder roughness.

2.4.1. Optical Coherence Tomography

One method for determining powder surface roughness is using optical coherence tomography (OCT) [65]. In an OCT system, a super-luminescent diode delivers a light beam to the surface of the sample, as illustrated in Figure 11. A high-speed spectrometer detects the interference pattern of light reflected off the different heights along the surface. This pattern can be used to extract a series of sliced 2D images, which can be stacked to produce a 3D profile of the powder surface as shown in Figure 12.

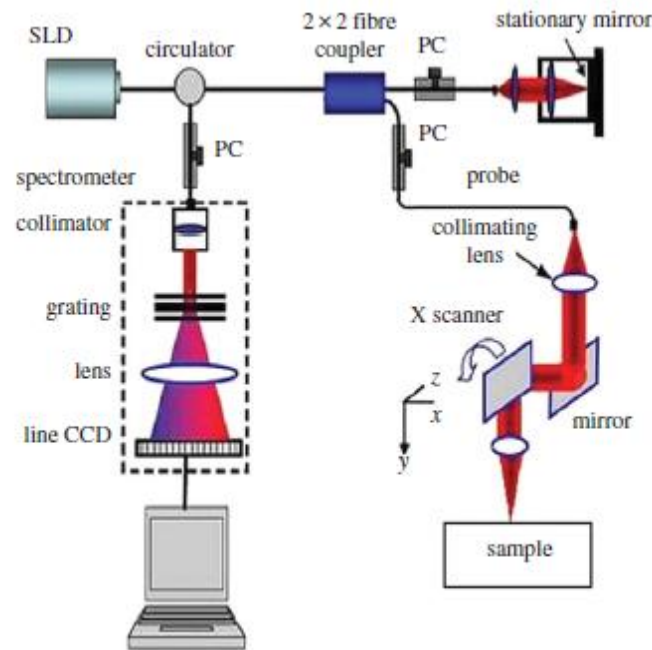


Figure 11. Typical optical coherence tomography setup [65]

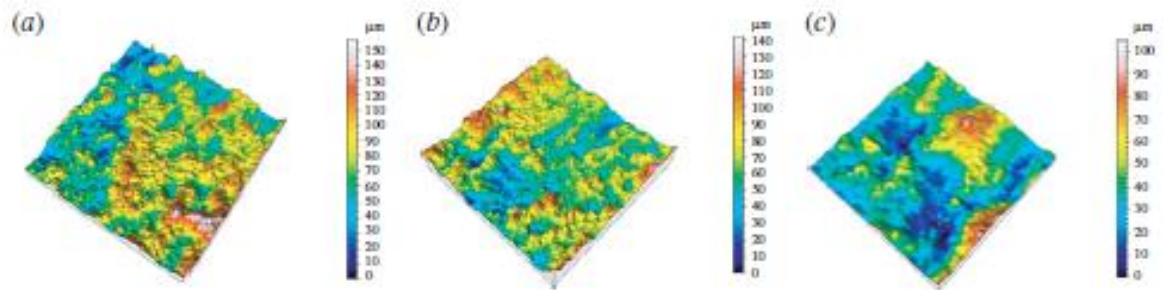


Figure 12. OCT-generated surface topography profiles of selective laser sintering samples [65]

2.4.2. Statistical Image Analysis

In a study by Sun et al (2015), the surface profile of spread Ti-6Al-4V powder was generated using Image Pro Plus software. Raised particles appear lighter in a grey-scale photograph due to light reflection as shown in Figure 13.2. The software assigns a pixel intensity value to each particle based on how the light appears. These pixel intensities were

then imported into MatLab to produce a 3D plot of the powder surface as shown in Figure 13.3.

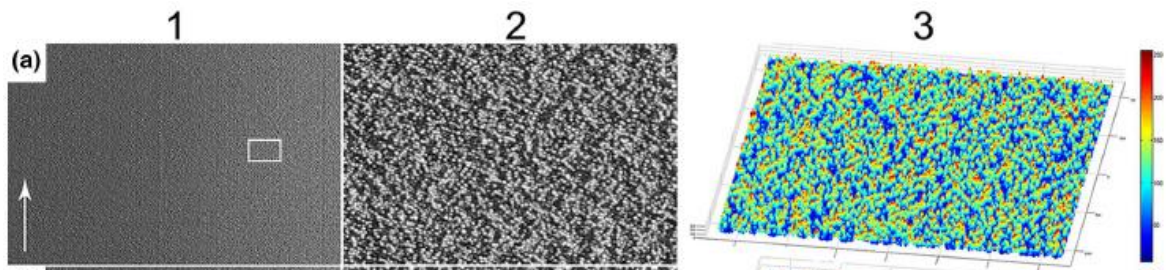


Figure 13. 45-106 μ m particles of Ti-6Al-4V (1) as spread, (2) zoomed in on surface of powder bed, and (3) imported into MatLab as 3D plot of pixel values [15]

2.5. Summary of Literature

In the preceding review, a range of particle characteristics and behaviors were explored. The established measurement techniques used to evaluate these properties could be useful in determining the quality of powder feedstock for SLM. Other methods of characterization not covered in this review include a number of simulation and modeling techniques. Therefore, a comparison of simulated results and experimentally determined characteristics could be useful in future work. This project, however, was more focused on hands-on experimentation. For the scope of this study, we determined the most important factor in spreadability to be the powder layer density. In the following section, the development and testing of a prototype measurement tool for powder density in spread powder layers is described.

3. Design and Experimentation

One of the goals of this study was to determine a simple, cheap and repeatable way to test the spreadability of a powder for the SLM process. The plan was to mimic the behavior of metal powder during spreading and measure the density of the metal after spreading, without rendering the test powder useless by melting it.

3.1. Early designs

Initially, a single layer spreading device was proposed, such as the drawdown shown in Figure 14. Drawdowns are used to measure the spreading properties of paint and other viscous films. It was suggested that a drawdown could be modified and set up to spread a monolayer of powder and in order to quantify its spreading behavior. This concept is similar to the previously discussed powder spreader developed by Van den Eynde et al [22]. However, drawdowns tend to be expensive and typically do not allow for layer thickness variation, or for the density of multiple layers of powder to be measured within a contained volume.



Figure 14. Drawdown paint analyzer by BYK-Gardner [66]

Next, a more complex apparatus was suggested in an effort to provide a deep enough test volume to understand the density of multiple layers of spread powder. A computer-generated model of this prototype is shown Figure 15. The design consisted of a spreading blade on a mechanical track (Figure 15a); an adjustable volume with height-adjustable wall (Figure 15b); a stationary base of the cube affixed to a scale beneath the apparatus to measure the mass of the sample (not shown); and an adjustable base to be raised with each spread layer (Figure 15c). This design was the first step in the direction of desktop density determination tools. However, the project was ultimately scaled back in complexity. Instead, a small test card that can be weighed on a regular scale for a quick analysis was proposed.

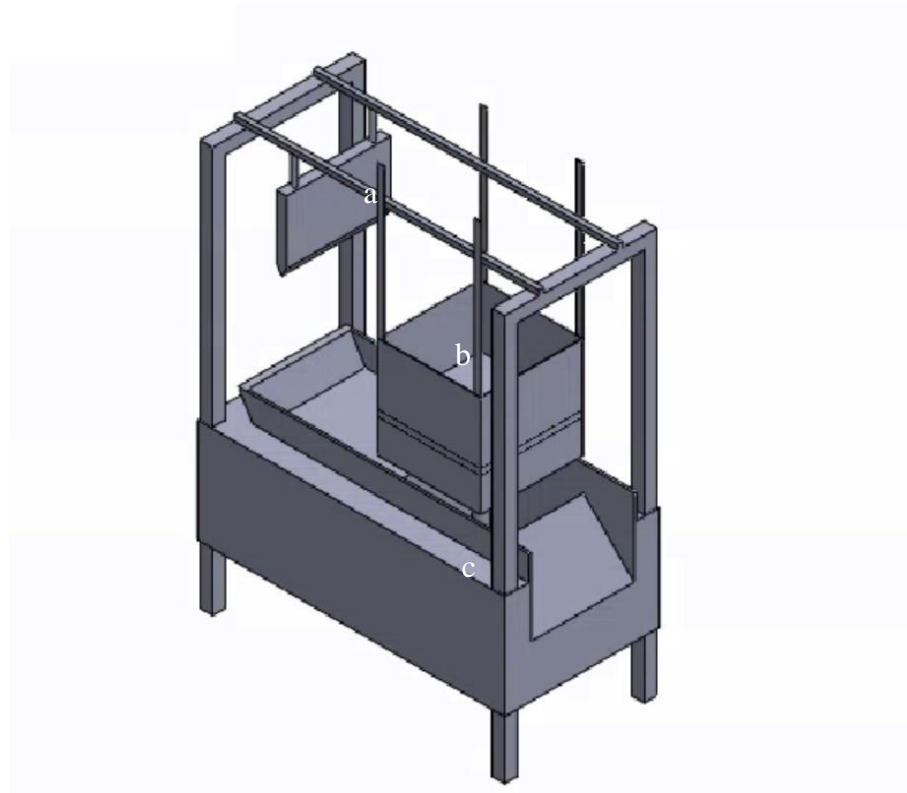


Figure 15. Automatic spreader design prototype

3.2. Final Notecard Design

The first prototype for the sample holder design consisted of multiple layers of 0.016-inch-thick aluminum. A solid rectangle with dimensions of 2 inches by 3 inches served as the base. The subsequent layers, with the same outside dimensions, have a 1.5-inch diameter circle laser cut from the center as shown in Figure 16. Once stacked, these pieces with a cut out make up the “walls” of the “sample volume” to contain the spread powder to be measured.

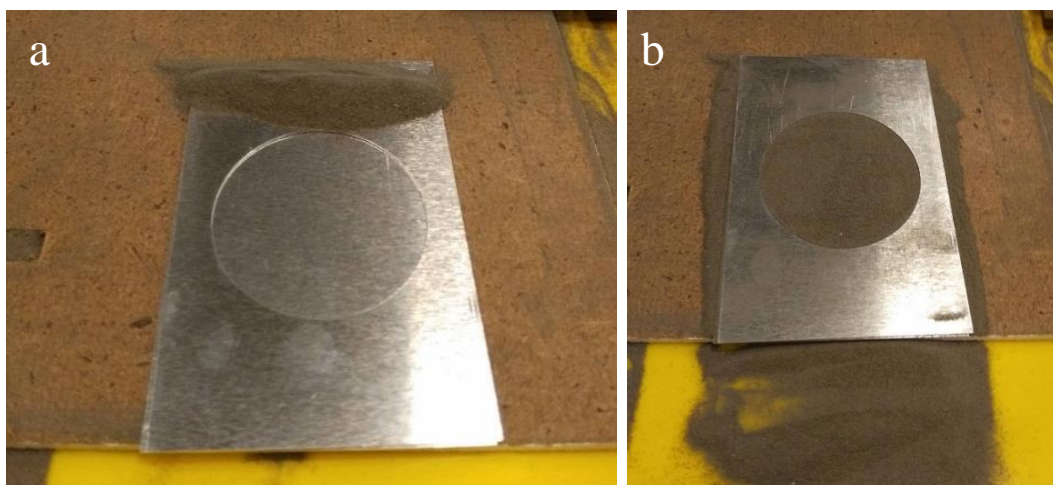


Figure 16. Single wall layer with base before spreading (a) and after spreading (b)

To test the spread density of a single layer, one wall sheet was stacked on top of the base sheet to create a short “cylindrical volume”. These two sheets were weighed together for the mass of the “container”. Next, a small amount of powder was spread along one edge of the circular area as shown in Figure 16a. Using the flat straight edge of a hard plastic sheet, the powder was then drawn across the circular area in one direction with a slow, steady motion to spread powder into the volume as shown in Figure 16b. Residual powder around the sample area was gently cleaned away using a fine brush so that powder only fills the area of the test volume as shown in Figure 17.

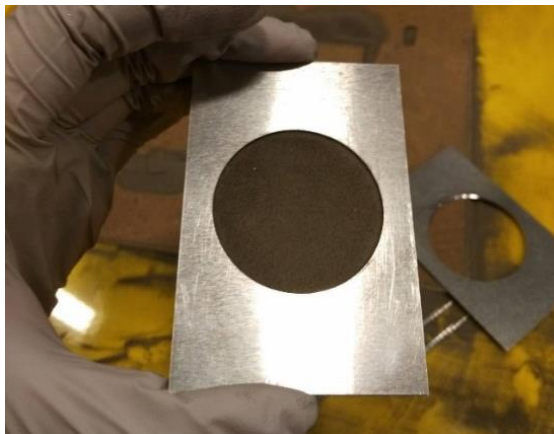


Figure 17. Sample holder after spreading a layer and cleaning surface of any excess powder

The mass of a single layer of thickness ~ 0.016 in was then determined by taking the mass of the sample and holder and subtract the holder mass. For multiple layers, a new sheet was placed over the surface after brushing. Then, pouring and spreading process was repeated. Mass of each new sheet was added to the mass of the initial mass of the sample holder, and the thickness of the new sheet was added to volume height (the total of a three-sheet volume shown Figure 18 below), respectively.



Figure 18. Three layers for a total container height of ~ 0.048 inches or ~ 1.2 mm

Powder stays relatively within bounds during process, as shown in Figure 19, indicating sufficient contact between base plate and sheets (some spreading-out likely would occur after wall layer is removed). It can also be expected that contact between layers is not 100%, due to small particles remaining on the sheet surface before the addition of another.



Figure 19. Powder volume after removing walls

For the preliminary test as shown in Figure 16 through 19, we used -100 mesh, water atomized 304 stainless steel (un-annealed), for which the tap density was $\sim 3.9 \text{ g/cm}^3$. The density results of four different spread methods using this material are shown in Table 1 below:

Table 1. Spread density of 150 μ m water-atomized 304 stainless steel with 0.41 mm sheets

	Density (g/cm ³)
Single sheet	2.42 \pm 0.045
Three sheets, single spread	2.91 \pm 0.209
2 sheets, spread after each sheet	3.28 \pm 0.251
3 layers, spread after each sheet	3.68 \pm 0.155
Apparent Density	3.10
Tap Density	3.87

Wall effects are clearly prevalent in a single layer sample, as evidenced by the increase in density per layer from one to three layers. These results are closer to the measured apparent density of ~ 3.1 g/cm³ than the tap density value. Three-layer samples appear to be denser when spread one layer at a time. However, excess powder trapped between layers may contribute to additional mass and thickness, distorting the results. In this case, a better spreading blade could provide a fully clear top surface of each layer and therefore could lead to more accurate results.

The layer thickness of actual SLM prints is closer to 50 or 60 μ m, so using a millimeter-thick layer is not necessarily indicative of the accuracy of this process. To scale down the thickness closer to that of SLM powder spreading, the process described was repeated using 18-8 stainless steel sheets with a thickness of 0.114 mm. For these thinner sheets, the diameter of the circular wall section is 1.25 inches. This sheet material is able to remain stiff at smaller thicknesses, making it a more promising option for simulating the SLM process. Three different size distributions of gas-atomized 316L stainless steel were tested for this layer thickness as shown in Table 2.

Table 2. Spread density of gas-atomized 316L stainless steel with 0.114 mm sheets

	Density (g/cm ³)		
<i>Particle Size (D₅₀):</i>	49μm	66μm	89μm
Single sheet	3.27±0.599	4.33 ± 0.353	4.54 ± 0.726
Three sheets, single spread	4.60±0.456	4.36 ± 0.074	4.30 ± 0.027
2 sheets, spread after each sheet	4.64±0.139	4.90 ±0.259	6.50 ± 0.245
3 layers, spread after each sheet	5.36 ± 0.387	5.83 ± 0.364	6.68 ± 0.421
Apparent Density	4.52	4.57	4.63
Tap Density	5.04	5.05	4.92

As shown in Table 2, the spread density taken from the test method is similar to the measured apparent density. Mean values for spread density were calculated to be higher than the tap density. Since this is not possible, the higher masses from these tests are likely due to powder spreading out between the layers. This excess mass is more for larger powder, where particles trapped between sheets have a greater effect on the height of the powder chamber.

3.3. Future Work

To be useful as a tool for powder property determination, the prototype developed in this project would require further additions and modifications. A standard method of seating, aligning and clamping the stacked pieces together should be developed to ensure higher consistency in the results. Other shapes for the test volume besides a round cylinder may contribute to more uniform spreading. Control over the spreading velocity and uniformity is also needed for better repeatability. Validation of the significance of density

measured using this method should be done by comparing the spread density to the density of printed parts. Comparison of spread sample density to density measured using the printed box method shown in Figure 4 may also be useful in determining whether the test method is a suitable simulation for spreading in the SLM process.

4. Conclusion

Following a review of literature on available methods for evaluating the powder flow, density, surface roughness and thermal conductivity; we designed a sampling process to measure the density of a powder bed comprised of thin spread layers. The prototype was tested for different thicknesses and powder types. The spreading tests showed that total density increases with an increasing number of layers. Furthermore, samples spread layer-wise showed higher average densities than the measured apparent densities for all powder types tested. This tool can be developed further to predict the density of a powder bed during SLM to select optimal powder for AM processes. While the scope of this project did not allow for experimentation of all the powder bed characteristics described in the review section of this report, the review of powder characterization methods provided a groundwork for how these measurement techniques could be implemented into a single device for identifying a powder spreadability indicator.

[Appendix references found in Chapter 6]

